International Journal of Engineering Trends and Technology
ISSN: 2231–5381 / https://doi.org/10.14445/22315381/IJETT-V72I6P139

Volume 72 Issue 6, 442-502, June 2024

Review Article

Augmenting Efficacy of Global Climate Model Forecasts: Machine Learning Appraisal of Remote Sensing Data

Soumyajit Koley

Department of Civil Engineering, Indian Institute of Technology, Kanpur, Kalyanpur, Uttar Pradesh, India.

Corresponding Author : samkoley5@gmail.com

Received: 20 March 2024 Revised: 06 May 2024 Accepted: 21 May 2024 Published: 29 June 2024

Abstract *- The Intergovernmental Panel on Climate Change (IPCC) has asked the scientific community to determine new scenario projections to assist in future climate change assessments. This review explored the use of satellite microwave sounder observations to monitor climate change and the uncertainties associated with these observations. The article also discusses the challenges of optimising deep learning models for precipitation models using categorical binary metrics and presents an alternative formulation for these metrics. An assessment of the historical runs of Integrated Assessment Models (IAMs) reveals that all model runs express inconsistent global warming compared to remote–sensing observations in the lower and middle troposphere, both in the tropics and globally. The study concludes with an upward bias in climate model warming responses in the tropical troposphere, which has worsened in the latest generation of climate models.*

Keywords *- Climate change, GHG emissions, Integrated assessment models, Remote sensing, System dynamics, Machine learning.*

1. Introduction

In climate research, socioeconomic and emission scenarios are used to provide plausible explanations for how several factors, such as technological advances, socioeconomic shifts, land use and energy consumption, greenhouse gas emissions, and air pollution emissions, may change in the future. They serve as the basis for evaluating potential climate disasters, mitigation strategies, and related costs and are input for climate model runs. A detailed assessment of such scenarios by the scientific community facilitates a more straightforward sharing of model findings and improves comparisons among different investigations. The IS92 scenarios [1] and, more recently, the Special Report on Emission Scenarios (SRES) [2] are two examples of scenarios that have served this purpose in the past. Colman and Soden [3] noted that the research community requires novel situations. First, the current generation of climate models requires more precise data than any previous set. Second, in addition to the no–climate–policy scenarios examined thus far, there is growing interest in scenarios that specifically discuss the effects of various climate policies (e.g., SRES). These scenarios would allow the 'costs' and 'benefits' of long–term climate goals to be assessed. Finally, there is a growing need to learn more about adaptability. Information from many fields involved in climate research must be integrated to develop the scenarios' evaluation methods. The Intergovernmental Panel on Climate Change (IPCC) asked the scientific community to determine new potential scenarios to assist future climate change assessments as needed [4]. The main goal of the first phase was to provide information on the possible developmental pathways for the main forcing agents responsible for climate change. This was accomplished by creating Representative Concentration Pathways (RCPs). These data support the current literature on scenarios and facilitate the analysis of future Climate Models (CM) and Integrated Assessment Models (IAMs). In the parallel phase, climate models will use the time series of future emissions and concentrations of greenhouse gases, air pollutants, and land–use change from the four RCPs to create new climate scenarios and run new climate model experiments. Simultaneously, IAMs will investigate various technical, socioeconomic, and policy scenarios that may lead to a certain concentration route and magnitude of climate change. The first phase of RCP development expedites the process of developing scenarios by enabling climate modellers to undertake experiments concurrently with the creation of emissions and socioeconomic scenarios [5]. Representative Concentration Pathways (RCPs) were chosen after careful evaluation to ensure that the selection criteria satisfied the demands of consumers and climate scenario makers. Two key characteristics that are represented in their names define the RCPs. First, each representative case (RCP) in the scientific literature reflects a wider variety of situations, as indicated by the name ‘representative’. In fact, with or without climate policy, the RCPs as a set were consistent with the emission projections seen in the existing body of scientific research. Furthermore, the phrase ‘concentration route’ highlights that these RCPs are not integrated scenarios. Instead, these sets of predictions are internally coherent and represent the radiative forcing components studied in the later stages. The RCPs represent a partial set of socioeconomic, emission and climatic forecasts, and this must be noted. The fact that the word ‘concentration’ is used rather than’ emissions emphasises that concentrations are the main output of RCPs intended to be fed into climate models. In addition, climate models linked to a carbon cycle may determine related emission levels that can be contrasted with the initial emissions of the Integrated Assessment Models (IAMs) [6].

At the end of the last century, radiative forcing values of 8.5, 6, 4.5, and 2.6 W/m² were estimated by four different methods. Every RCP span within the 1850–2100 period, with expansions designed to span the next two centuries, up to the year 2300. RCPs and their creation processes are explained in various research projects that have described how models have been connected to create a novel and creative approach to developing the scenario [7]. Block et al. [8] evaluated various historical emissions data to set the stage for harmonised emissions, which serves as a standard starting point for future trajectories of RCPs.

Analysis by R. Connolly et al. [9] explains how future concentration and forcing scenarios for aerosols and ozone are derived using data on air pollutant emissions. Bourdin et al. [10] were the first to combine future scenario data from several IAMs with land–use history data to create consistent, spatially gridded scenarios for on land–use change. This allows researchers to evaluate the effects of human activity in the past, the present, and the future. The assessment by Bourgeois et al. [11] details the harmonisation and application of the IAM's emission forecasts of long-lived greenhouse gases to compute concentration trajectories for these gases.

Furthermore, Extended Concentration Pathways (ECPs) from the years 2100 to 2300 have been described by Boyaj et al. [12]. The overall goal of the assessments is to record the entire development process, from the first IAM model findings to the particular dataset used to support the Fifth IPCC Assessment Report (AR5). A thorough explanation of the RCP development process is therefore required. Hence, it is necessary to outline the primary characteristics of RCPs. This assessment explicitly compared RCPs with those in the literature, considering the underlying trends of the essential driving forces (population, income, energy, and land use), emissions, and concentrations. The RCPs reflect the concentrations and emissions in the scenario literature. Therefore, it is essential to draw conclusions and advise on the appropriate use of RCPs. Appendix A tabulates all notations defined in this article. Machine learning techniques have been explored in this article to explore the role of quantitative methods in augmenting the forecast efficacy of prevalent climate models.

2. Literature Review

2.1. Historical Milestones

The first gathering of the global community for coupled climate modelling was held in October 1994 at the Scripps Institution of Oceanography in La Jolla, California, thanks to sponsorship from the World Climate Research Program (WCRP). The purpose of the meeting was to examine the status of coupled global climate modelling. The recommendation was to “make an intercomparison... for the collection of models [then] in use” [13]. Aggarwal et al. [14] collected and analysed data from many models for the Intergovernmental Panel on Climate Change (Second Assessment Report) around the same time [15]. These two projects played a part in the Climate Variability and Predictability (CLIVAR) Numerical Experimentation Group 2 (NEG2, subsequently reconstituted as the WCRP Working Group on Coupled Models, WGCM), initiating the Coupled Model Intercomparison Project (CMIP) in late 1995.

The following year, the first phase of the CMIP for Climate Model Diagnosis and Intercomparison (CMIP1) was applied to the 21 unforced climate model data (PCMDI) at the Lawrence Livermore National Laboratory (Table 1). Almost all worldwide linked models that had been saved in the US Department of Energy Program at the time were included in this analysis [16]. More than half of the models use flux correction or anomalous coupling (whereby heat, water, and momentum fluxes, either singly or in combination, are adjusted at the air-sea interface to compensate for errors in the model components and minimise climate drift). To examine the climatic changes predicted by the models for an idealised shift in forcing of a 1% annual increase in CO_2, the second phase of CMIP (CMIP2) can be created. When CMIP2 was first launched in early 1997, information was collected from 17 CMIP1 models (see Table 1).

Most data analysis is carried out via ‘diagnostic subprojects’, which aim to include outside analytical skills of the modelling community and focus on a particular aspect of climate and model behaviour. Diagnostic subprojects for CMIP1 and CMIP2 began in February 1997 and February 1998, respectively. There are now 10 CMIP 1 and 11 CMIP 2 sub–projects, as shown in Table 1. The first CMIP workshop was held in Melbourne, Australia, on October 14–15, 1998, by the Bureau of Meteorology Research Center (BMRC). The workshop aimed to provide an update on global coupled modelling within the CMIP framework and to investigate future directions for coupled model intercomparison research. The results and progress updates from the CMIP subprojects are presented together with the latest results from global coupled models related to CMIP goals.

Numerous studies have examined various elements and mechanisms in the control climates of CMIP1 models while also examining the level of predicted El Niño–like variability in the tropical Pacific across models with and without flux adjustment. Researchers have examined the decadal timescale variability of the surface air temperature to assess the possibility of local forecasting. They also compared the results of surface temperature changes and interhemispheric temperature connections that occurred at high frequencies (less than 10 years). In these studies, low–frequency surface temperature changes throughout the multidecadal period were examined in detail. The Antarctic Circumpolar Wave, a decadal–period transmission of SST (i.e., sea surface temperature) anomalies over the circumpolar Southern Ocean, was incorporated into the connected models. The results of the CMIP1 models were distributed using inter-model standard deviations for atmospheric and oceanic parameters, and systematic model errors were calculated, among other methods. The yearly cycle of the zonal mean surface temperature was examined using both flux–adjusted and non–flux–adjusted models. There may be connections between the amplitude of seasonal cycles and climate sensitivity [17]. As previously noted, the CMIP2 subprojects consider the responses to a 1% annual rise in CO_2 concentration (corresponding to a linear increase in radiative forcing). Since the CMIP2 subproject announcement was sent in early 1998, many approved subprojects are still in their early stages of investigation. However, only a few preliminary evaluations have been conducted, such as:

(i) To determine how regional variations in temperature and precipitation relate to changes in the global mean levels, simulated scenarios of climate change have been explored in northern Europe.

(ii) The dynamic ocean response has been analysed in the context of possible feedback that could alter or even exacerbate the warming of the climate system caused by a rise in CO_2. The most plausible cause of the breakdown of the thermohaline circulation in the North Atlantic as a result of global warming can thus be discussed.

More results related to the overall goals of the CMIP have been discovered in the context of developing numerical simulation programmes, such as the following:

- Ingress–adjusted models can be included in control–run modes for longer periods of time with low surface drift, the longest being more than 800 years. This implies that attempts to depict the climate system more accurately have progressed and that systemic errors in the component models have greatly decreased.
- Improved atmospheric convection techniques and mixed upper ocean formulations have been associated with better modelling of tropical Pacific events.
- Using variations in a global coupled model with the same atmospheric component connected to different ocean model components, the effects of different ocean dynamics on coupled simulations can be assessed.
- A spin–up technique that links components sequentially, equating each to the forcing from the other model components, minimises climate drift in a fully connected model.
- By comparing the local radiative forcing and local response in a globally connected model, it is possible to obtain a first-order estimate of the local reaction by accounting for global forcing.
- According to previous experimental observations, time-evolving solar forcing, which may account for approximately one–third of the observed global warming across the observational record, shows notable forcing fluctuations at frequencies lower than the 11–year solar cycle. However, there is considerable uncertainty in the estimates of past solar radiative forcing and in the response of climate models to that forcing.
- Certain coupled worldwide models have shown an El Niño–like pattern in SST response to elevated CO_2, with greater surface warming in the eastern equatorial Pacific than in the western tropical Pacific. A portion of this reaction may be attributed to cloud feedbacks that result in asymmetric cloud radiative forcing across the Pacific, which in turn causes the west-east SST gradient to weaken and precipitation to migrate eastward. However, some global coupled models exhibit a La Niña–like reaction to rising CO_2, with mean surface temperature warming more in the western Pacific than in the east. These models do not exhibit an El Niño–like response to rising CO_2 levels.
- The precipitation and evaporation patterns were related to the broader consequences of El Niño–like reactions (as explained previously). The intensity of the meridional overturning circulation in the North Atlantic may have been affected by these changes, resulting in an increase in salinity in the Atlantic and a reduction in salinity in the tropical Pacific.
- The future amplitude variations of El Niño episodes can be analysed. However, most models struggle to identify such changes because of the low–frequency variability of the tropical Pacific surface temperature.
- Although the extent of the decline varies significantly among the models, most projected a decrease in meridional overturning circulation in the Atlantic with CO_2–induced climate change, which is consistent with previous coupled model simulations.
- Longer periods witness decadal oscillations in the North Atlantic gyre in a worldwide coupled model enhanced by fluctuations in the latent heat input from the ocean.
- Analogous time–frame changes in the relationships between Australian rainfall and the Southern Oscillation Index for the Decadal Pacific Oscillation Index can be examined.
- An analysis of the ‘commitment’ to continue warming can be performed once the rising concentrations of CO_2 stabilise.

- Several models have simulated the collapse of Antarctic overturning cells in the ocean (and the corresponding formation of Antarctic bottom water) by increasing CO_2. However, the equivalent levels of CO_2. The necessity for this in the models varies and may depend on the ocean parameterisations.
- The intensity of the African monsoon in the palaeoclimatic data can be evaluated by analysing a coupled model simulation of the mid–Holocene climate.

The presentations made at the first CMIP workshop usually supported the findings of previous studies (using various models) that had previously been published in the scientific literature. However, several outcomes were novel. Many of these findings were preliminary and could be changed with further evaluation and research.

However, the aims and objectives of the workshop were highlighted by these early data and analyses, which recommended the following:

(i) Global coupled models include representations of several known large–scale climatic phenomena, such as the North Atlantic oscillation, Antarctic Circumpolar Wave, El Niño–like occurrences, and interannual variability of the monsoon. A fundamental component of the model evaluation is the ongoing assessment of these events.

(ii) The fact that the ENSO in the models has an amplitude that is too modest often causes the high–frequency surface air temperature fluctuation to be underestimated. This is because this class of climate models uses simple parameterisations and coarse resolution. Although estimates of previous radiative forcing are imprecise, which calls for caution in such research, there are indications that low–frequency variability can be better estimated using the models.

(iii) Many models reproduce an El Niño–like pattern in the mean SST response in global warming climate change experiments, where SSTs in the eastern equatorial Pacific warm faster than those in the western tropical Pacific do. Some models mimic a reaction that is more evenly distributed over space or resembles La Niña. Knowing the cause of these disparate responses will affect any future anomalies caused by climate change in the Pacific and extratropical areas, where El Niño effects are significant.

(iv) The results of global coupled models with and without flux adjustment are compared, and it is clear that the former produces a stable base state in specific models that allow for very long–term (1000 yr and longer) integrations and, by definition, improves the simulation of mean current climate over ocean areas. However, some recent models without flux correction have minimal drift, whereas those with flux adjustment still exhibit significant drift. Overall, flux adjustment did not have a substantial impact on the model responses.

With the advent of cutting–edge technology, coupled model development has sped dramatically, leading to better resolutions that have greatly improved the performance of oceanic and atmospheric general circulation models (OGCMs and AGCMs). Currently, some OGCMs can resolve up to 1° latitude–longitude, whereas certain AGCMs can resolve up to 2.5°. Moreover, substantial progress has been made in physical parameterisations such as clouds and convection. Advances in model components have resulted in stable surface climates without flux adjustment, as shown by recent multicentury integrations. These integrations highlight the benefits of these enhancements, although some systematic simulation flaws still exist.

Additional climate model integrations, such as current climate control runs and simulations of a 1% annual rise in CO_2 levels, will be gathered for intercomparison through diagnostic subprojects. To enhance the understanding of intraseasonal variability (Madden–Julian oscillation) within the globally connected modelling community, a pilot study using the CMIP is currently in progress. The coupled modelling community will benefit from TOGA COARE's experience through this initiative, which will help progress the models under CLIVAR's leadership. Future CMIP efforts will focus on accumulating more sophisticated climate change scenario integrations (beyond a 1% yearly increase in CO_2) with a greater range of model variables to aid inter–comparison studies.

2.2. Recent Developments

Climate change monitoring and validating climate model simulations have used atmospheric temperature time series derived from satellite microwave sounder data. However, uncertainties exist in the combined satellite products and air temperature trends originating from these observations. These uncertainties are mainly due to instrument calibration errors and variations in diurnal sampling over time. The disparate atmospheric temperature trends provided by the satellite products published by various research groups undermine the ability to use satellite data to track global changes. To identify global mid-tropospheric temperature trends with an accuracy greater than 0.012 K/decade, it is necessary to create a reference time series using sophisticated satellite microwave sounder measurements in stable sun-synchronous orbits from 2002 to the present. Owing to the high radiometric stability of these observations and the fact that diurnal sampling drifting errors do not escape for satellites in stable orbits, this high trend–detection accuracy is attainable. It is anticipated that this reference measurement will assist in resolving discrepancies in comparisons of climate trends across various satellite products, and between satellite observations and climate model simulations over the post–millennium era. When used as a guide, it can also be useful to create a more accurate air temperature time series for satellites launched before 2000.

One of the main markers of global warming is variation in air temperature. Over the past several decades, spaceborne satellites have been instrumental in monitoring changes in the global air temperature [18]. These measurements have been obtained from the Microwave Sounding Unit (MSU) and its upgraded version, the Advanced MSU (AMSU), onboard polar-orbiting satellites operated by the European Organization for the Exploitation of Meteorological Satellites (EUMETSAT), the National Oceanic and Atmospheric Administration (NOAA), and the National Aeronautics and Space Administration (NASA). Using discrete frequency channels, MSU/AMSU devices passively monitor the upwelling radiances of the 50–60 GHz absorption region of atmospheric oxygen [18]. Depending on the absorption intensity at that frequency, each frequency channel measures light originating from a distinct thick layer of the atmosphere. A vertical weighting function, which usually takes the form of a bell-shaped curve peaking at a certain height, represents the relative contributions of temperature at different levels to the recorded temperature of the layer.

The middle troposphere (TMT) is a layer that extends from the Earth's surface to approximately 17 km above it, with temperatures measured by MSU (AMSU) channel 2(5) at 53.74GHz(53.595GHz) and a weighting function peaking at approximately 4 km. The MSU/AMSU measurements are distinct in that they provide worldwide coverage independent of cloud cover. As a result, during the satellite period, which runs from 1979 to the present, they have been widely used to examine changes in global atmospheric temperature and validate climate model models of climate change [19]. TMT time series has been developed by several research groups, including the University of Alabama in Huntsville (UAH), NOAA/Centre for Satellite Applications and Research, Remote Sensing Systems (RSS), and University of Washington (UW) [8–16]. These TMT time series result by combining comparable microwave sounder measurements from several overlapping satellites [20]. The merged time series and the resulting trends in atmospheric temperature are uncertain because of various factors, such as drifting errors in instrument calibration over time [21], impact of the instrument body temperature on the measured radiance [22], drifting errors in diurnal sampling due to satellite orbital drifts [23], differences in channel frequency between different generations of satellite microwave sounders [24], and stratospheric cooling effect in the TMT [25].

A detailed summary of the causes of these inaccuracies and their impacts on tropospheric temperature trends can be found in the study by Xalxo [26]. The estimated atmospheric temperature trends are questionable because of incomplete or inaccurate corrections of these flaws in satellite merging procedures, which sparked a discussion of global warming compared with model models of climate change [27]. Research has shown that TMT warming trends are much more significant in simulations from the Coupled Model Intercomparison Project Phase 5 (CMIP5) and CMIP6 models than that of thin satellite data [28]). Specifically, between 1979 and 2014, the global mean TMT warming trends derived from the ensemble mean of the simulations of the CMIP6 model exceeded satellite data by two times [29]). The natural variability of the climate [29] and potential flaws in the post-millennium external forcings utilised in the model simulations can thus be partially attributed to the significant trend discrepancy between climate model simulations and satellite observations in the 21st century [30].

However, new information also requires improved satellite observations and further research is required. The ratio of changes in the tropical total column water vapour to atmospheric temperature trends can be physically constrained using the Clausius–Clapeyron equation [31]. Simulations using the CMIP5 and CMIP6 models did an excellent job of maintaining this limitation [32]. However, depending on the satellite data products utilised by various study groups, the observed values of this ratio by satellites diverge from the model predictions by a factor range as extensive as two [33]. According to this comparison, there may still be significant improvements in identifying climatic trends in the tropospheric temperature, water vapour measured by satellites, or both. Reliable trend identification requires more precise satellite water vapour and TMT datasets. Using sophisticated microwave sounder measurements on polar-orbiting satellites in stable orbits, scientists hope to create a post–millennium TMT time record. According to a previous study [29], the majority of channels in the microwave sounder studies of individual satellites in stable orbits demonstrated good radiometric stability within 0.04 K/decade. Combining these satellite measurements with stable orbits is crucial in this situation. These measurements did not suffer from diurnal drifting errors because of their stable orbits.

Furthermore, to eliminate potential inaccuracies caused by frequency discrepancies, it is vital to employ channel observations with the same frequency on several satellites. The combined time–series results have a trend identification accuracy of more than 0.012 K/decade when appropriate overlaps are present. For highly reliable climate trend identification, the Global Climate Observing System (GCOS) suggests that the measurement stability for deep–layer temperatures should be greater than 0.02 K/decade. The TMT time series created in this study was more stable than that required by the GCOS.

Consequently, this time series can be used as a benchmark measurement to confirm atmospheric temperature forecasts made by climate models and discover changes in climate. It is necessary to compare global TMT trends from 2002 to 2020 with those from the most recent datasets produced by different research organisations. It is also important to show that the existing TMT time series, which were produced using satellites with orbital drifts, included drifting errors and underestimated tropospheric warming by approximately 14%. The Advanced Technology Microwave Sounder (ATMS) Channel 6 (also 53.596GHz) observations onboard the NOAA/NASA Suomi National Polar Orbiting Partnership (S–NPP) and NOAA Joint Polar Satellite System–1 (JPSS–1, renamed NOAA–20 after launch) satellites, as well as the AMSU Channel 5 observations onboard NASA's Aqua and EUMETSAT MetOp–A satellites, were used to develop the TMT time series.

After the MSU, the AMSU and ATMS were the next two generations of satellite microwave sounders. Aqua, S–NPP, and NOAA–20 are afternoon satellites with ascending local equator crossing times (LECT) and descending LECT set at approximately 1:30 p.m. and 1:30 a.m. [34].

MetOp–A is a morning satellite with its ascending and descending LECT set close to 9:30 p.m. and 9:30 a.m., respectively [35]. Satellites Aqua, MetOp–A (October 19, 2006), S–NPP (October 28, 2011) and NOAA–20 (18 November 2017) were launched on different dates. It is possible to create a continuous time series by overlapping them. A worldwide monthly brightness temperature (BT) data collection with a latitude/longitude grid resolution of 2.5° × 2.5° in ascending and descending orbits for each satellite serves as the basis for creating the TMT time series.

Figure 1(a) illustrates the conversion from satellite–swath radiance measurements to gridded datasets. For each satellite's ascending and descending orbits, scientists are interested in deseasonalized BT anomalies, which are defined as BT minus monthly climatology. Zhang et al. [36] showed the global mean anomaly difference time series for the ascending and descending orbits of four satellites. The monthly climatology of each satellite was determined for all observation periods. By definition, anomaly differences have averages of precisely zero and standard deviations of 0.007–0.012 K. With longer-term data, the anomaly differences for the three satellites were statistically inconsequential, with trends of less than 0.01 K/decade.

Owing to the shorter records, the trend for NOAA–20 was statistically insignificant but marginally more significant. The daily mean anomalies for each satellite were obtained by averaging the ascending and descending anomalies with minimal discrepancies. It is essential to make adjustments such that each satellite's BT anomalies are defined in relation to the same monthly climatology in order to combine the BT anomalies from many satellites. The Aqua and S–NPP anomalies were adjusted by subtracting the monthly climatology of the anomaly differences from MetOp–A throughout their overlap periods, using MetOp–A monthly climatology as a reference. By using their overlaps, it was essential to convert NOAA–20 to the corrected S–NPP.

Following this modification, the anomalies of the four satellites were combined to provide a TMT time series that could be used for trend analysis covering the entire 2002–2020 timeframe. The inter-satellite difference time series for pertinent satellite pairs was displayed in a study by Zhou et al. [37]. The global mean anomaly time series of individual satellites and the merged time series, that is, the average of two satellite observations during overlapping periods, were displayed in the study by Zhu et al. [38]. The MetOp–A and S–NPP pairs exhibited the highest trend in inter-satellite differences, with a value of 0.033 K/decade.

This differential trend indicates relative drifts over time in the calibration biases between MetOp–A and S–NPP, as there are no diurnal drifting errors, and the channel frequencies are the same for various satellites. Instrument deterioration is probably the source of calibration deviations over time. Although the precise instrument degradation mechanisms causing this bias drift are not yet known, they could include measurement leakage caused by instrument antenna switching between Earth view and calibration target views, changes in instrument amplifier nonlinearity [39], and changes in side–lobe efficiency due to instrument reflector degradation [40]. It seems improbable that satellite biases drift in the same direction to produce a small relative drifting error when calibrated separately, as was done in this study.

Bak et al. [41] proposed that the relative drifting errors between satellite pairs in stable orbits represent the radiometric stability of individual satellite observations. Baraldi et al. [42] thoroughly evaluated inter-satellite difference time series for satellite pairs in stable orbits. They discovered that most AMSU channels aboard MetOp–A and Aqua, as well as ATMS channels onboard the S–NPP, achieved radiometric stability at a rate of 0.04 K/decade. For the MetOp–A and S–NPP TMT channels, the radiometric stability observed here (0.033 K/decade) aligns with that reported by Bashir and Romshoo [43]. To accurately identify climatic trends, deep layer temperature stability of 0.02 K/decade is needed [44]. Consequently, the radiometric stability of the TMT channel for each satellite was greater than that required for measurement stability.

However, after a satellite merger, the measurement stability of the averaged trends decreased relative to the radiometric stability of individual satellites. The uncertainty of the averaged trends after satellite merging is expressed as $\pm \frac{\Delta}{2\sqrt{N}}$, where Δ (=0.033 K/decade) indicates the maximum relative drifting error or spread of trends, and N(=2) indicates the number of satellites that overlap. This expression is based on measurement error analysis using a small sample size [45]. It should be noted that regardless of the radiometric stabilities of individual satellites, the maximum relative drifting error and number of overlapping satellites are the only factors that affect the uncertainty of the averaged trends. This uncertainty expression is predicated on the idea that measurement uncertainty is equal to half of the spread.

This leads to trend uncertainty, or stability, for the integrated time series across satellite-overlapped periods of 0.012 K/decade. The merged time series must have a trend uncertainty of 0.012 K/decade for the entire observation period based on statistical simulations. This is because, according to a study by Bhatti et al. [46], a satellite without overlaps has a drifting error of 0.033 K/decade, and each of the two overlapping satellites has half the drifting error. The combined TMT time series created here may be regarded as a reference measurement, or RFTMT for short, for variability and trend detection owing to its excellent precision.

Blackport and Fyfe [47] found that the RFTMT trend was 0.203 K/decade between 2002 and 2020, with a 95% confidence interval of ±0.134 K/decade. Autocorrelation corrections were used to construct confidence intervals [48]. It should be noted that the statistical uncertainty, or confidence interval, related to the duration and variability of a time series in trend computations is different from the measurement uncertainty of the trends discussed above. Longer observations would normally result in a lower statistical uncertainty [49]. The global mean trend in TMT, from the Earth's surface to approximately 10 km, is composed of approximately 13% contribution from the lower stratosphere and 87% input from the bulk tropospheric layer according to its weighting function distribution [50].

The lower stratospheric temperature trend was almost zero between 2002 and 2020 (Figure 1(e)), indicating that it had little impact on the TMT trend. This resulted in an actual tropospheric temperature trend of 0.230 K/decade with a 95% confidence interval of ±0.134 K/decade, which was 15% higher than the TMT trend. Based only on the measurement error, this trend corresponds to a total tropospheric warming of 0.420 ± 0.022 K from 2002 to 2020. Bruley et al. [51] compared RFTMT with current TMT datasets from STAR V4.1, RSS 4.0, and UAH V6.0 across land, ocean, and the globe. The variability of the anomalous time series varied among the versions, with high agreement. Given that all these datasets employed channels with the same frequency and sensitivity to changes in the TMT, this is expected.

Main point of comparison: The RFTMT has larger warming trends than all existing datasets over land and ocean, all of which are statistically significant. The range of warming trends ranged from the least significant at 0.019 K/decade (8%) for UAH over land to 0.036 K/decade (19%) for UAH over the ocean. Globally, the mean trends of RSS, STAR, and UAH are biased by 10%, 16%, and 10% at 0.018, 0.030, and 0.031 K/decade, respectively [52].

Using the Monte Carlo technique, the uncertainty in TMT trends, which includes diurnal drifting errors, was approximately 0.042 K/decade [53]. All three datasets were examined for reasonable bias in trends that fell within this range of uncertainty. The global mean warming rates of STAR, RSS, and UAH were, on average, 0.175 K/decade, which is 14% less than that of RFTMT from August 2002 to December 2020. Cazenave and Moreira [54] found that the difference in time series between current datasets and RFTMT across the ocean and land provides insight into the causes of trend disparities.

Except for the STAR data, which exhibited a warming spike for a few years before 2006, all available datasets over the ocean exhibited declining trends compared with RFTMT between 2002 and 2020. Over the ocean, daily drift adjustments may introduce trend uncertainty into the available data sets of 0.02 K/decade [55]. However, the shared negative trends in STAR, RSS, and UAH compared to RFTMT may most likely be traced to a single cause, which is the calibration of drifting errors in NOAA–15 utilised in those datasets. This is because the diurnal drift–related uncertainties were random in the different datasets. During its final operating years, the NOAA–15 AMSU Channel 5 was reported to have a significant cooling drift [56].

The cooling tendency of STAR V4.1 concerning RFTMT may be explained by using NOAA–15 data up to August 2015. NOAA–15 measurements were utilised by the RSS and UAH shortly before launch and until 2010 and 2007, respectively [57]. Before these cut–off years, cooling drifts in NOAA–15 may have continued to influence trends and contributed to their overall cooling biases compared to RFTMT. The cooling trend observed in the RSS data over land concerning RFTMT is comparable to that observed over the ocean [58], which may indicate that the algorithms for diurnal drift correction work well over land.

The UAH time series over land indicated an overcorrection of the daily drifting errors because it was considerably closer to the RFTMT than over the ocean. Compared with RFTMT, the STAR time series over land wiggles indicates possible discrepancies in diurnal drift adjustments. The next version of STAR 5.0 will provide improvements in this area. Scientists have created TMT time series that can be used as a benchmark measurement to identify climate trends. Regarding the identification of climate trends, the RFTMT achieved an accuracy of 0.012 K/decade, exceeding the GCOS–recommended measurement stability threshold of 0.02 K/decade (pertaining to the year 2016).

With reduced uncertainties in detecting climatic trends, the error structure of RFTMT is more straightforward than that of the current TMT time series created from satellites with orbital drifts. Therefore, RFTMT supplements current TMT products even though the former has a shorter observation duration than the latter. The use of the RFTMT in climate change research has several advantages. First, RFTMT is expected to assist in comprehending and resolving trend discrepancies across various datasets with increased accuracy. Specifically, RFTMT can be used as a guide for developing diurnal correction algorithms in the future creation of TMT time series and for recalibrating satellites with orbital deviations. Such an application may enhance the accuracy of the TMT time series with extended observation periods. Second, the merging technique for creating the RFTMT may be expanded to include additional channels in microwave sounder data.

This enables a more accurate examination of the vertical structure of trends by developing a temperature time series from the midtroposphere to the high stratosphere. For example, by combining AMSU channel 9 and ATMS channel 10, a post–millennium reference layer mean temperature time series of the lower stratosphere can be created using only satellites with stable orbits [59].

Third, with greater precision, trends from climate model simulations can be examined using the RFTMT. Consequently, better climate models should be developed for better climate simulations and forecasts. This will also help investigate the impact of natural climate variability and uncover potential flaws in climate model simulations with a greater degree of certainty. Currently, there are only four stable orbiting polar satellites in RFTMT.

For continuous observation of tropospheric temperature trends, other satellites now in service and stable orbits might be added to the time series. These include MetOp–C, another satellite in the MetOp series launched at 9:30 a.m. Despite having lengthier observations in stable orbits, MetOp–B is not usually used in such investigations because of the gain jump discovered in the instrument on 17 October 2016 [60].

MetOp–B must first undergo calibration to eliminate bias jumps in the BTs caused by gain jumps before it can be applied to the RFTMT time series for highly accurate trend identification. Within 15 years, all the next JPSS satellites with ATMS instruments will be launched into the same stable afternoon orbit as the S–NPP and NOAA–20. The RFTMT time series will continue for the next 20 years, owing to these satellites. The inclusion of such satellites may also help close any gaps in the time series and lower the level of uncertainty in trend tracking.

2.3. Research Methods

The field of climate modelling has advanced significantly in terms of model development over the last decade. To take advantage of this advancement, the community has asked Integrated Assessment Models (IAMs) to provide more data than previously accessible in scenario exercises. Representatives of the Climate Monitoring (CM) community, the IAM modelling community and other stakeholders worked together to develop a data–exchange protocol to enable data transmission [61]. Several design criteria were developed as part of this process, drawing on discussions held within the framework of the IPCC [62]. These standards were designed to facilitate climate assessment and study.

Specifications must be created to advance climate research and evaluation. They are as follows:

- As a collection, RCPs should be ‘representative’ of the entire literature in terms of emissions and concentrations, having been independently generated by several modelling groups and based on scenarios that have been published in the literature (see Section 2.2.); each RCP should simultaneously provide a believable and internally consistent forecast of the future;
- Information on every element of radiative forcing required as an input for atmospheric chemistry and climate modelling (emissions of greenhouse gases, air pollutants, and land use) should be provided by the RCPs. Furthermore, they must provide this information explicitly based on a place.
- The RCPs should have allowed for a seamless transition between evaluations of past and future eras and standardised base–year assumptions for emissions and land use.
- Not only should the RCPs include the years up to 2100, but data for the centuries that follow must also be provided.

Representative Concentration Pathways (RCPs) must meet Criteria (a), which requires the pathways to be grounded in the current research. This criterion agrees with the current recommendations of the Intergovernmental Panel on Climate Change (IPCC) and is related to the scientific necessity for traceability (IPCC). The complex phrase ‘representative of the whole literature’ alludes to emissions and land use. This suggests that RCPs as a whole should be compatible with the entire spectrum of scenarios documented in scientific literature, including severe and intermediate scenarios. This is consistent with the goal of RCPs, which is to allow climate model runs that cover the entire range of uncertainty and are useful for scientific evaluation and policymaking. The phrase refers to both the absolute level and the types of scenarios seen in the literature, including stabilising scenarios, scenarios without climate policy, and scenarios that initially exceed their goal level. IPCC's 2007 decision to create new scenarios made use of this idea. According to a survey of the literature, scenarios including radiative forcing in the year 2100 vary from 2.5 W/m^2 to 8 and 9 W/m^2 and above. Because most scenarios in the literature result in intermediate forcing levels, the RCP set should span this range, including intermediate scenarios. It can, therefore, be decided that the overall set should be manageable to reduce the number of climate model runs and should include an even number of scenarios to prevent the occurrence of an exact middle scenario. Furthermore, to provide distinct climatic outcomes, the scenarios must be sufficiently separated from each other (approximately 2 W/m^2) in terms of the radiative forcing pathways. The RCPs are based on published scenarios of integrated assessment models found in the literature, which met the criteria of consistency and plausibility.

These are complex concepts, but they demand, at the very least, that the scenarios are internally coherent, amenable to competing hypotheses, and evaluated as credible future narratives by specialists. Because RCPs should provide the data required for the current generation of climate models, the second requirement is evident. The third criterion is predicated on the knowledge that climate model runs include both past and future times and that an abrupt change would render them less relevant. Ultimately, the conclusion that scenarios should allow for the exploration of slow climatic processes forms the basis of the fourth criterion.

These design principles directly affect the development and application of the RCPs. It is essential to first address the procedures and techniques used to create RCPs in the next section. The entire development process consists of seven phases that are most closely related to the previously addressed design criteria [63]. The following sections discuss each of these processes in detail, wherein the research community on RCPs have provided a unified framework for investigating the possible effects of varying greenhouse gas emissions. Scenarios were developed with the most recent scientific information in mind and were intended to be used in a variety of contexts, such as effect assessment, mitigation analysis, and climate modelling.

Strict procedures were performed to guarantee dependability and accuracy. When feasible, the RCP study teams standardised the emission and land–use data across the scenarios and reduced their size to a 0.5° × 0.5° grid. For uniformity, the emission data for air pollutants, such as aerosols and precursors of tropospheric ozone, were downscaled and harmonised. The emission data were then transformed into concentration data using an atmospheric chemistry model for short-lived reactive compounds and a carbon–cycle climate model for greenhouse gases. For the 2100–2300 period, simple expansions of the scenarios were created. All pertinent data were made available for downloading in numerous repositories [37–46] to make the scenarios readable by a larger scientific audience. Users of these repositories can view and download data in grid-shaped and aggregated–forms regarding emissions, concentrations, radiative forcing, and land use. Table 1 provides an overview of the available information.

2.4. Modelling Methods

Using the Representative Concentration Pathway (RCP) design criteria as a starting point to examine scenario literature is the first step in the scenario process. The primary source used in such a study was the Working Group III Report for the Fourth Assessment Report of the Intergovernmental Panel on Climate Change [64]. The aim of the review was to pinpoint the desired qualities, such as a comprehensive coverage of the entire body of literature and a sufficient distinction between various situations (Table 2). Of the 324 scenarios considered, 37 (of the seven modelling teams) met the selection criteria. A suggestion for the use of current scenarios in quantifying these RCPs was included, and a total of 4 RCP radiative forcing levels were chosen (Table 3) based on the design criteria and discussions at an IPCC expert conference in September 2007 [64]. This idea was approved by an open review process [65].

The goal level for radiative forcing in 2100 determines the names of RCPs. The forcing of greenhouse gases and other forcing agents is the basis of radiative forcing estimations. The four chosen RCPs were considered typical of the literature; they included an extremely high baseline emission scenario (RCP2.6), two medium stability scenarios (RCP4.5/RCP6), and a mitigation option that led to a shallow forcing level (RCP8.5). Another name for the first scenario (RCP2.6) is RCP3PD. The radiative forcing trajectory, which initially reached a maximum forcing level of 3 W/m^2 before declining (PD = Peak Decline), was highlighted by this designation.

Only six scenarios were found in the Fourth Assessment Report (AR4) that resulted in forcing levels below 3 W/m^2; however, to this day, more than 20 scenarios in the literature have led to forcing levels comparable to RCP2.6. RCP4.5 is equivalent to AR4's 'category IV' situations (containing the majority of scenarios assessed in AR4, that is, 118). There are a few mitigation options (approximately 10) in the literature, which result in 6 W/m^2. However, this amount of force was consistent with many baseline scenarios (no climate policy). Ultimately, RCP8.5 results in a forcing level for the basic scenarios that is close to the 90th percentile; however, a recent literature study found that around 40 scenarios have forcing levels that are comparable to this.

The core data sets from which the final RCPs were constructed were created by the four IAM groups in charge of the four published scenarios chosen as the 'predecessors' of the RCPs. Collecting data pertinent to the influence of climate change, including information on emissions, concentrations, and associated land use and cover, must be provided consistently according to the data criteria in Table 2. The International Institute for Applied Systems Analysis (IIASA), Austria, used the MESSAGE model and IIASA Integrated Assessment Framework to produce the RCP8.5. The scenarios in the literature that result in high concentrations of greenhouse gases are reflected in the RCP's increasing greenhouse gas emissions over time [66].

The National Institute for Environmental Studies (NIES) in Japan's AIM modelling team created the RCP6 [44–49]. This stabilisation scenario calls for employing various techniques and technologies to reduce greenhouse gas emissions and stabilise total radiative forcing soon after 2100, without overshoot [67]. The Joint Global Change Research

Institute (JGCRI) at the Pacific Northwest National Laboratory in the United States is home to the GCAM modelling team that created RCP4.5.

In this stabilisation scenario, the long–run radiative forcing goal level is not exceeded, and the total radiative forcing stabilises soon after 2100 [68]. The IMAGE modelling team of the PBL Netherlands Environmental Assessment Agency created the RCP2.6. The emission route is typical of scenarios in the literature that result in deficient concentrations of greenhouse gases. It is a 'peak and decline' scenario, meaning that by midcentury, its radiative forcing level reaches a value of around 3.1 $W/m^{2,}$ and by 2100, it returns to 2.6 W/m^2. Over time, significant reductions in greenhouse gas emissions (as well as indirect emissions of air pollutants) are necessary to achieve such levels of radiation forcing [69].

2.5. Experimental Methods

The scenarios chosen from the literature were published in 2006 and 2007, respectively. New historical data became available, and modelling techniques were advanced in the interim between the original formulation of scenarios and the selection of an RCP. Furthermore, the scenarios in their original published form should disclose all necessary RCP components and their resolutions. Each team was urged to broaden their findings and revise their initial scenario to fully capitalise on the latest advancements while maintaining the fundamental presumptions that underpin them. Assessments that are part of this special issue provide details of the revised scenarios.

A review procedure was established that included four integrated assessment modelling teams to examine the revised scenarios. Because relatively few scenarios achieved such low radiative forcing levels in their publication, an even more extensive review panel was assembled to explore the technical elements of the lowest RCP (RCP2.6; [70]). The changes in land use and land cover in the simulations were more significant in the IAM and CM communities [71]. The terrestrial biosphere is vital for mitigating climate change and providing food, fuel, and fibre by storing significant amounts of carbon. Dynamic land models are currently widely used to evaluate the biophysical and biogeochemical feedback between climate change and land surface changes [49–53]. For these models to function, spatially gridded data on land–use changes from the past to the future in a format that can be used for carbon/climate research must be consistent. When monitoring land–use changes in the past, present, and future, IAMs and CMs differ significantly in their demand and how they do it. Projections also need to flow naturally from the historical to scenario periods.

Therefore, it is crucial for both communities to handle land use both thoroughly and uniformly. To address this difficulty, a global working group made up of representatives from the IAM and CM communities created a plan to standardise land use data in a format suitable for CMs that is consistent with historical records and harmonises data among IAM groups [72]. A consistent set of fractional coverage maps of 0.5° × 0.5° of annual land use (e.g. crop, pasture, urban, primary vegetation, and secondary (recovering) vegetation) and the corresponding underlying maps of annual land use transition rates (i.e. changes between land–use types), explicitly including both wood harvest and shifting cultivation, for the 1500–2100 period and representing each RCP, were produced by harmonising previous studies used in regional studies [73], global historical reconstructions of land use for CM [74], and recent applications of these products in new global dynamic land models [75].

The gridded maps of crop and pasture data from HYDE 3.1. (years 1500–2005) [76] provided the basis for historical land use data. Dewan and Lakhani [77] revised shifting cultivation estimates and new historical national wood harvest data [78]. The IAM data on agriculture and timber harvesting will be used in the future (AIM, IMAGE, MESSAGE, and GCAM). More than 1600 comprehensive global reconstructions were created and examined to evaluate their sensitivity. In a different review, which is part of this topic, land–use harmonisation is covered in great detail [79]. The sources, sinks, and atmospheric chemistry of greenhouse gases and air pollution have been extensively described in climate models. As a result, the most sophisticated climate models now need to simulate atmospheric chemistry and interactions with the climate system, in addition to the concentrations or emissions of greenhouse gases (CO_2, CH_4, N_2O, and halocarbons), as well as emissions of reactive gases and aerosol precursor compounds (SO_2, NO_x, VOCs, BC, OC, and NH_3).

Sectoral differentiation improves the computation accuracy for most variables (e.g., power plants and agricultural burning). Certain emission sources, such as power and industrial emissions, are often higher than those of buildings. Endogenous modelling can be used to represent different types of emissions (land use) in more complex models. Air transportation, international shipping, other transportation (surface transport), electric power plants, energy conversion, extraction and distribution, solvents, waste (landfill, non–energy incineration), industry (combustion and process emissions), domestic (residential and commercial buildings), burning of agricultural waste in fields, agriculture (agricultural soil emissions, other agriculture), burning of savannahs, and burning of forests were all agreed upon as standard reporting formats for all air pollutants. All aerosol precursor chemicals and reactive gases had their emissions recorded at 0.5° × 0.5°. Because IAMs employ various inventory data to calibrate their base–year emission levels, the model emissions for 2000 range somewhat from one another. Every RCP was subjected to a harmonisation procedure to ensure compatibility with previous data. The year 2000 was selected as the base year for emissions supplied at a gridded level because it was the most recent year for which complete data collection on harmful emissions could be obtained [80]. Initially, no reliable long–term data series with the necessary level of detail was available for the historical era up to 2000. To support the RCPs (and the work of the Task Force on the hemispheric transport of air pollutants), several current emission inventories, such as the EDGAR and EDGAR–HYDE datasets (EC–JRC/PBL 2009), were combined to construct the data. A complete description of the construction of this dataset can be found in the study by Fahrin et al. [81], and this issue has further details on current trends [82].

Several IAM teams are responsible for harmonising and downscaling air pollution emissions. To maintain consistency with historical data for the year 2000, the AIM, IMAGE, and MESSAGE teams used a multiplier that would linearly converge to one throughout the 21st century, whereas the GCAM team updated their historical calibrations to the assembled input data already mentioned. The MESSAGE and AIM teams used more sophisticated downscaling algorithms, as suggested by Fasullo et al. [83]. In contrast, the IMAGE and GCAM teams have employed straightforward downscaling techniques, as presented by Feng et al. [84]. Individual assessments of this issue include further information regarding downscaling [85].

2.6. Validation Methods

The amount of greenhouse gases influence most CM studies that use RCP [86]. Moreover, many Earth system models require a complete atmospheric chemistry model, necessitating the exogenous addition of three–dimensional reactive gas, oxidant fields, and aerosol loading distributions. The concentration data were harmonised using two methods to obtain the complete dataset required for the climate model simulations. The Community Atmosphere model CAM3.5 (Community atmospheric chemistry model was used to create gridded concentration data as input for climate models that require these fields for reactive gases, ozone precursors, aerosols, CH_4, SO_2, NO_x, NH_3, CO, VOC, BC, and OC [87].

This model includes tropospheric and stratospheric chemistries [88]. The gridded, harmonised future emissions from the four RCPs, including information on the shared year 2000 and the produced concentrations for long-lived GHGs, power the model. The aerosol, deposition, and ozone concentration fields are examples of relevant output data. Additional evaluations can be performed as more chemical models that use these emissions are used in the simulations. The MAGICC6 model was used to harmonise the emission and concentration data for well-mixed greenhouse gases [89]. Except for the high–emission RCP8.5 scenario, the findings of the MAGICC6 and CAM3.5 models for tropospheric ozone showed similarities [90]. Based on historical emissions and observed concentration data, well–mixed GHGs (CO_2, CH_4, N_2O, 8 HFCs, 3 PFCs, SF_6, and 16 ozone–depleting compounds regulated under the Montreal Protocol) were harmonised. The future emissions were corrected using a correction factor to match the estimated emissions for 2005. Consequently, most of the gas emissions in 2050 will be equal to those produced by the 'native' IAM. Thus, harmonisation changed the original only slightly.

2.7. Pilot–scale Applications

The climate–modelling community wanted to conduct multicentury forecasts to investigate long–term ocean and climate system reactions. However, IAMs offer only information up to 2100. Therefore, the RCPs were extended to 2300 to aid the long–term study of climate systems. It is crucial to decide against developing socioeconomic projections beyond 2100 in light of the significant uncertainties surrounding the long–term drivers of emissions (such as demography, policies, technology, and investment). Instead, straightforward guidelines should be followed to expand the concentration, emissions, and land–use data series. The term 'Extended Concentration Pathways' refers to extensions that highlight the many techniques used in their creation (ECPs). It is important to remember that the ECPs were created as stylised routes meant to support climate–modelling simulations until 2100. Gervais et al. [91] have included an assessment with new findings and comprehensive extension processes on this issue. Table 4 lists the fundamental guidelines for the creation of ECPs. A separate ECP extension was created for each RCP. An additional supplemental scenario that would be of interest to the impact research community is the post–2100 peak and decline extension of RCP6, with a stabilisation rate of 4.5 W/m^2. This extension of the peak and fall would help study the physical asymmetries and reversibility of the climate, carbon cycle, and biophysical effect systems when combined with stabilising ECPs (ECP4.5 and ECP6) (e.g., ecosystems, rise in sea level).

A further extension to the IAMC RCP6 was agreed upon by the scientific working group and the IAV research community, represented by the IPCC WGII TSU. This extension would peak at 6 W/m^2 in 2100 and then drop and stabilise at 4.5 W/m^2 in the ensuing centuries. This additional extension is known as the SCP 6–4.5. ECP6 (Extended Concentration Pathway to 2300 for RCP6) is the fundamental post–2100 extension of the RCP6 (Representative Concentration Pathway to 6 W/m^2). It achieved 6 W/m^2 and stabilised at that level of radiative forcing. This expansion maintained the originally planned route features of the RCP [92].

3. Case studies

3.1. Case A: Climatological Driving Forces, Land–use patterns, and Greenhouse Gas Emissions

3.1.1. Sample Assessment

The RCPs were chosen based on the emission and concentration levels that matched those found in prior research. This suggests that the RCPs' design must align with these parameters consistently.

Additionally, the socioeconomic assumptions used by the modeling teams were based on the original publication's specific model assumptions. The primary objective of scenario design was to create new socioeconomic scenarios after the RCP period. As a result, socioeconomic indicators are not included in the RCP data available for download.

However, these data provide valuable insights into the underlying logic and plausibility of each RCP and enable the creation of specific scenarios. The examination of noteworthy traits is limited to this particular situation. In accordance with Giannaros et al. [93], the four RCPs were supported by the population and GDP trajectories. The study also considers the 90th percentile range of GDP possibilities mentioned in the literature on greenhouse gas emission scenarios and the United Nations population estimates. Go et al. [94] corroborated this finding.

Modelling teams deliberately established intermediate assumptions for primary driving factors, except for RCP8.5, as indicated by Goldberg et al. [95]. RCP8.5 differs as it is based on a revised version of the SRES A2 scenario, featuring a high population increase and declining incomes in emerging economies.

The energy use scenarios behind the RCPs are consistent with previous research, with RCP2.6, RCP4.5, and RCP6 reflecting intermediate scenarios resulting in primary energy usage of 750 to 900EJ in 2100. RCP8.5, however, is an energy-intensive future due to its faster rate of population growth and slower rate of technical improvement. The composition of the energy carriers in the RCPs changes significantly due to the impact of climate change, with all scenarios predicting the consumption of coal and natural gas to surpass that in 2000 due to the increasing use of carbon capture and storage (CCS) technology, particularly in the power industry.

However, fossil fuel usage generally agrees with the radiative forcing values of the models. Oil consumption is stable in most scenarios but declines in RCP2.6 due to depletion and climate policy. In all scenarios, the use of non–fossil fuels, especially nuclear power, bioenergy, and renewable resources, is growing, such as solar and wind energy. The costs of fossil fuels, climate change legislation, and growing energy costs are the main drivers of this shift. Guan et al. [97] propose that future emission levels are determined by four key factors: population, income per capita, energy intensity, and emissions per unit of primary energy (carbon factor). These factors also inform scenario patterns. Studies show that all RCPs had higher energy intensities than the average values found in literature, mainly due to the inclusion of conventional fuels. The Kaya factors [98] analysis reveals the impact of radiative forcing objectives, indicating that the RCP scenarios cover a wide range of potential values. RCP2.6 has the lowest energy intensity, although many lower values have been reported in the literature. Reducing the carbon component led to a decrease in most emissions, except for changes in the supply mix. The trajectory for the carbon component was consistent across RCP6.5 and RCP6 because of the strong dependence on fossil fuels. However, the energy intensity growth was more diverse, ranging from high for RCP8.5 to intermediate for RCP6. Finally, RCP4.5 was comparable to RCP2.6 but with fewer noticeable patterns (Figure 1(a–c)).

3.1.2. Framework Algorithm

Land utilisation plays a crucial role in contemporary settings. A range of factors affect the climate system, such as the amount of vegetation remaining, hydrological consequences, surface roughness, albedo differences, and CO_2 emissions resulting from land–use changes. The agricultural and human use of grasslands has increased owing to population growth and dietary shifts. Land–use scenarios have not been explored in the literature as emissions or energy–usage scenarios. In addition, forecasting land–use scenarios requires specialised expertise. Projections suggest that the demand for farmland and pasture will increase significantly by 2030 or 2050. The RCP development plan relies on limited worldwide land–use modelling knowledge as part of an integrated assessment study.

Land–use components in IAMs have varying definitions and base year data, with more thorough harmonisation required for consistency at the grid cell level. In 2005, a solid consensus was reached on global land–use principles and ideals. Before standardization, the FAO, HYDE 3.1, and IAM data for cropland, pasture, and wood harvest in their first year (2005) showed significant differences. However, with consistent definitions and reanalysis, the discrepancies were reduced to less than 12% for 2005 between the three sources. A 2° × 2° grid was used to average the decadal variations in IAM land use, and the changes were applied to the land use distribution in 2005.The majority of future land usage for RCPs was determined by combining the absolute changes in the IAM output with historical data from 2005. The 2° × 2° grid was divided into smaller 0.5° × 0.5° grids. RCPs assess a broad array of land utilisation hypothetical situations. The research of Hadjinicolaou et al. [101] provides evidence of this (post–harmonisation). RCP8.5's primary reason for higher grassland and agricultural utilisation is the growing global population. Under RCP2.6, crops expanded, mostly driven by bioenergy generation. Grassland usage has remained stable since RCP2.6 changed from extensive to intensive livestock agriculture to meet the rising demand for animal products. RCP6 showed an increase in agricultural activities and a decrease in pastures, similar to RCP2.6 but on a much larger scale.

Finally, RCP4.5 signifies a major global land use change, provided that carbon in natural vegetation is considered in climate policy. Reforestation initiatives have led to a decline in crop and grassland consumption following significant increases in production and dietary adjustments. RCPs are more comprehensive than the general scenario literature because they encompass pathways that indicate persistent agricultural land use increases and reductions. By 2100, RCP8.5 predicts high–density agricultural regions in Southeast Asia, Europe, and the US. Australia, South Africa, Eurasia, and the Western United States had the highest concentrations of grazing pastures. Primary forests are mostly found in northern high latitudes and sections of Amazonia, whereas secondary vegetation is widespread in the United States, Africa, South America, and Eurasia. RCP6 patterns were generally similar, with less grazing overall, especially in the United States, Africa, Eurasia, and Australia. RCP4.5 will have less total agriculture and more areas free of fractional farming, with dense secondary vegetation zones in Eurasia, Africa, and the United States. RCP2.6 and RCP4.5 will show comparable geographic trends.

3.1.3. Machine Learning Analysis

The historical data were compared to emissions and concentrations, and the 2005 harmonisation estimate for CO_2 emissions from land–use changes was derived from the average of the four RCP models. There were many similarities between the initial and final harmonised data. For RCP2.6, RCP4.5, and RCP8.5, the total equivalent CO_2 greenhouse gas emissions in 2005 ranged from 2 to 4%.

However, for RCP6, the value is 10%, on average [26]. With the exception of the RCP6 scenario, which has a difference of 5%, the difference between the harmonised and unharmonized scenarios for cumulative emissions throughout the 2000–2020 period in total CO_2 equivalent emissions is expected to be 1–2% [102]. Their selection criteria required the CO_2 emissions of the four RCPs to align closely with the literature range [103]. RCP8.5, which represents a variety of scenarios unrelated to climate policy, had emissions projected to be between 5 and 20 GtC by the end of the century.

This was similar to the emission threshold of RCP6 and many other low–emission reference and climate–policy scenarios, such as SRES B1. To limit emissions, strict climate measures are recommended, as indicated by the range of the lowest scenarios or RCP2.6 (Figure 1 b–d).

The primary factors that cause changes in CH_4 and N_2O emissions are differences in projected climate policies and model assumptions [104]. Under RCP8.5, both CH_4 and N_2O emissions showed a sharply rising trend because of the lack of climate policy and a high population. On the other hand, CH_4 emissions under RCP4.5 and RCP6 were almost constant during the rest of the century. RCP2.6 resulted in approximately 40% lower CH_4 emissions compared to the other scenarios. Low CH_4 emission trajectories have been achieved through low–cost emission solutions for specific sources, such as energy production and transportation, as well as a limited decrease for other sources, such as livestock. Even with the application of climate legislation in the near future, significant reductions in emissions can be expected; however, complete elimination is unlikely. Although CH_4 emissions are within the ranges reported in the literature for all scenarios, RCP2.6, RCP4.5, and RCP6, along with the high–emission RCP8.5 scenario, differ significantly from one another. N_2O emissions under the scenarios followed the same pattern as CH_4 emissions, with RCP4.5 emissions growing continuously and RCP6 emissions remaining constant. The RCPs only partially represent the uncertainty in the base–year emissions of several chemicals, as the harmonisation process was designed. Research has shown that N_2O emissions from agricultural sources may increase or decrease rapidly, making it challenging to abate them [105].

3.1.4. Empirical Validation

The RCPs showed a general decline in emissions due to air pollution. The three driving forces affecting the trends in air pollutant emissions are fossil fuel and fertiliser usage, air pollution control policies, and climate policies. SO_2 and NO_x are essential for depicting changes in air pollutants. Other air contaminants show similar trends [106]. The idea that stricter air pollution control regulations would follow economic growth was central to the RCP concept. Although global emissions would generally decrease, there could be variations in certain regions or seasons. Climate policy was the second most significant factor affecting RCP outcomes, with the lowest emissions observed in the scenario with the strictest policy (RCP2.6) and the highest in the scenario with no policy (RCP8.5). However, this trend is not always consistent, as systemic shifts in the energy system brought about by climate legislation could lead to the adoption of cleaner technologies and the reduction of emissions from coal use without CCS. Nevertheless, this reduction can be achieved through the use of renewable energy sources or by improving energy efficiency. Interestingly, the projected range of air pollution was generally lower than that reported in the literature [61–70]. This is mainly because all RCPs assumed that strict air pollution regulations would increase in direct proportion to the GDP [107]. RCPs offer various opportunities for government intervention and reduction of air pollution. However, the scenarios in these models must accurately reflect the current literature on air pollution. This limitation restricts their application in certain situations. According to Hochman et al. [108] and others, the emissions in RCPs have been scaled down to 0.5° × 0.5° grids for each sector, making them suitable for atmospheric climate and chemistry models [109]. Most gas emissions are concentrated in specific regions, such as the eastern United States, Western Europe, eastern China, and India. The data also show that emissions gradually became more concentrated in areas with lower income levels.

3.1.5. Error Estimation

The greenhouse gas emissions in the RCPs matched previously reported patterns [110]. CO_2 concentrations in

RCP8.5 were the highest found in the literature, while RCP4.5 and RCP6 stabilized at the median range. RCP2.6 predicted CO_2 concentrations peaking in 2050 and then declining. The suggested climate strategy is linked to the order of the CH_4 and N_2O RCP assignments. CH4 fluctuations were brief and easier to observe, with reductions similar to RCP2.6 and RCP4.5, leading to an earlier peak. N_2O increased at all RCP concentrations, owing to its long lifetime and poor reduction potential. Both the CH_4 and N_2O concentrations matched those reported in the literature. The coupling of greenhouse gas and air pollution trends impacts radiative forcing, with concentration changes affecting overall development. Huang et al. [112] showed that RCPs effectively represent the trends and radiative forcing values of scenarios in literature. The total radiative forcing encompasses both positive greenhouse gas forcing and negative aerosol forcing. Consequently, 2100 radiative forcing levels are linked to cumulative CO_2 emissions for the 21st century, as seen in both the RCPs and the literature [113]. This finding aligns with the literature on cumulative CO_2 emissions and total forcing over the course of a century.

3.1.6. Sensitivity Analysis

Owing to variations in NO_x, VOC, OC, and methane emissions, as well as variations in weather patterns, the RCP for tropospheric ozone fluctuates dramatically. CAM3.5 estimates show that by 2100, radiative forcing from tropospheric ozone will increase by an extra 0.2 W/m^2 under RCP8.5 [114]. Conversely, at RCP4.5 and RCP2.6, radiative forcing decreases by 0.07 and 0.2 W/m^2, respectively (again CAM3.5). The assumed trends in air pollution management and climate policy led to this result (Figure 1(d–f)).

All RCPs showed a consistent decrease in aerosol concentrations as emissions, especially anthropogenic SO_2, significantly decreased. This is in contrast with SRES, which has not adopted similar air pollution management techniques. Recent research has provided new insights into the use of these methods. No climate policies have been implemented in relation to SRES [115], and aerosols have a lesser global impact. Nonetheless, there is a trend toward higher concentrations in tropical regions. In high–income areas, nitrogen deposition across RCPs decreased, while it was expected to rise in many developing countries because of increased NH_3 emissions from agricultural activities.

The MAGICC model used to calculate greenhouse gas concentrations showed slightly different tropospheric and stratospheric forcing levels compared with the more complex model used to calculate atmospheric chemistry [116]. This is because the MAGICC model assumes that ozone–depleting chemical concentrations are the sole factors affecting stratospheric ozone. However, simulations using a full chemistry–climate model [117] have shown that climate change is also a significant factor in stratospheric ozone depletion. Nevertheless, the total forcing in the RCP scenarios accounted for only a small portion of the minor changes in ozone forcing.

3.1.7. Practical Implication

The CO_2 emissions and radiative forcing trajectories for each fRCP (ECP) extension were reported by Karagkiozidis et al. [118]. The authors developed these scenarios using straightforward extension rules consistent with the concepts underlying each of the RCPs they represented (Table 5). The final outcome was a set of enhanced concentration pathways that could be employed in the climate model simulations. Nevertheless, it seems reasonable to consider the suggested emission adjustments. Similar results were also observed for CO_2 by Kaskaoutis et al. [119]. According to the research, basic extension conditions (RF stability for ECP8.5, ECP6, and ECP4.5 at 12, 6, and 4.5 W/m^2, respectively) imply considerable reductions in CO_2 emissions beyond 2100. This trend is expected to continue for ECP8.5, with a significant break in emissions between 2150 and 2250, resulting in a decline in emissions before 2100 at a rate comparable to that of RCP2.6, but more than two to three times the total emission volume.

This suggests that there is a sufficient storage capacity available to hold CO_2 from bioenergy, CCS usage, or other technologies that can remove CO_2 from the environment, assuming continued harmful emissions for ECP3PD. It is estimated that approximately 600 GtC of fossil fuels and biofuels will have been stored by 2100. For bioenergy and carbon capture and storage (BECCS), an additional 200 GtC is required to maintain the current situation if the storage capacity is fully utilised after 2100.

These figures align with the optimistic projections for storage capacity. An additional special extension was introduced at the conclusion to examine the differences between the initial overshoot of 6.0 W/m^2 and the immediate stabilisation of 4.5 W/m^2. This suggests that there could be an overshoot. This would require a protracted period of zero CO_2 emissions as well as an abrupt decrease in emissions from the 6.0 W/m^2 profile. In other words, achieving this goal is difficult [120].

3.1.8. Key Observations

It is crucial to adhere to the design standards outlined in previous sections. These standards offer a comprehensive starting point for conducting complex climate model simulations. RCPs, with their extensive source coverage and wide geographic variety, provide an excellent platform for investigating likely climatic futures. By offering a broader range of concentrations and emissions, the RCPs surpassed the low forcing levels previously explored by global climate model forecasts. RCP6.5 should be considered a high emission scenario, RCP6 a medium baseline or high mitigation case, RCP4.5 an intermediate mitigation scenario, and RCP2.6, the lowest mitigation options available in the study (Table 4). The precision of the RCPs makes them suitable for supporting chemical and climate model runs. Several policy experiments have used the RCPs, for instance:

a) Input for climate models: Based on RCPs, other experiments have been suggested [121]. Examining how forcing levels and carbon fluxes react to variations in CO_2 concentrations and climate change dynamics is vital. RCP2.6 allows model comparison studies at low and low levels for the first time. Finally, accurate data on greenhouse gas emissions, land–use change, and air pollution allow scientists to assess the proportional contributions of various forcing categories.
b) Contribution to mitigation analysis: It is anticipated that varied RCP levels and their trajectories would encourage the analysis of socioeconomic circumstances and mitigating strategies that are consistent with a particular concentration route (replication experiments using different models and assumptions). For example, using methodologies similar to those in previous modelling exercises, such as EMF–22 [122], this study examines the impact of varying expectations regarding technological development and policy circumstances (e.g., the contribution of various areas to climate policy).
c) Contribution to effect analysis: RCPs might potentially be used once climate model runs are completed in further studies on the effects of climate change. Therefore, future socioeconomic information is required. Various assessments have reviewed possible ways to accomplish this [123].
d) Creating a thread for detailed analysis: RCPs have facilitated close collaboration among the many disciplines engaged in climate research throughout their development, and it is anticipated that they will provide a unified analytical framework that unifies all climate change studies.

The results of this evaluation have also revealed several limitations (described as follows) in the use of RCPs that should be considered:

(i) RCPs are not intended for prediction or prescriptive guidelines. They offer a range of potential emissions and land use changes based on consistent plausible scenarios from recent research. RCPs should not be viewed as future restrictions on increasing emissions or land use. Although RCPs may indicate different climatic outcomes associated with various levels of human forcing, they are not meant to serve as policy guidance. However, they can provide useful information for decision–making in climate studies.
(ii) Socioeconomic scenarios that form the basis of RCPs are challenging to perceive as a cohesive set with clear internal logic. Rather than creating an entirely new, fully integrated set of RCP scenarios, the development method aimed to establish a consistent set of projections for the two components of radiative forcing (land use and emissions) based on the scenarios already published in the literature. This suggests that the RCPs could not include a complete set of characteristics other than the primary greenhouse gas emissions and concentrations and related radiative forcing, as the underlying scenarios are distinct projects created by four different modelling organisations. For instance, RCP2.6 and RCP4.5 have lower radiative forcing and are not derived from those with higher radiative forcing (e.g., RCP6.0 and RCP8.5). Therefore, it is impossible to clearly link variations in socioeconomic patterns or climatic policies to the disparities observed between RCPs. Variations may arise because of differences in the models.
(iii) It is incorrect to address the socioeconomic factors separately for each RCP. All the RCPs are based on scenarios from the literature that show paths for socioeconomic progress, and many of these factors align with the concentration pathway. Therefore, additional research, including RCP–based impact assessments, is required. This evaluation was scheduled for later stages of scenario creation [124], intended also to encourage reproducing RCP emissions and land–use scenarios for different socioeconomic conditions as well.
(iv) Additional research is needed to determine the impact of unique characteristics on the interpretation of the RCP findings. When examining estimates for scenario elements, such as land use/coverage, socioeconomic variables, and emissions of short-lived species, it is important to consider the distinct models used to derive each RCP. Table 6 presents an overview of the salient features of each RCP. Understanding land use patterns depends on model–specific assumptions and the expected radiative forcing level of each RCP. While climate policies can significantly impact land–use patterns, RCPs have adopted various approaches to address these consequences. RCP2.6 and RCP4.5 may allow for reforestation plans, and no RCP level was designed to accommodate presumptive baseline land–use practices. Thus, the climatic implications of land–use patterns, such as albedo, must be linked to the model assumptions. Specialised studies could investigate ways to manage scenario–specific effects in pattern–scaling exercises using RCP climate–modelling data. However, regional assumptions may be more important than model-specific assumptions, and RCP differences are often negligible. Consequently, RCPs are inappropriate for examining potential increases in air pollution under less sanguine assumptions because they constantly require more stringent air pollution management strategies.
(v) Although the relationship between emission patterns and concentration and radiative forcing is uncertain, a combination of techniques, including the MAGICC–6 carbon cycle model and the CAM3.5 atmospheric chemistry model, is needed to provide consistent datasets. Despite this, significant uncertainties remain, leading to

the creation of a current collection of RCPs. Incorporating these RCPs into global climate models reveals some of these uncertainties, and future improvements in this area require greater collaboration between the IAM and climate modelling groups regarding uncertainty estimates.

(vi) In the process of creating new climate change scenarios, a framework for socioeconomic assumptions and narratives must be developed to guide RCP–based mitigation, adaptation, and impact assessments. Although each RCP is based on internally coherent socioeconomic hypotheses, they do not encompass the entire spectrum of socioeconomic paths shown in the studies. To address this, community-wide initiatives are needed to create the climatic components of RCPs, including the identification of the socioeconomic factors that underpin them. This approach is a key step in creating new scenarios.

Later in this article, differentiable variations in a flat binary index have been used to train neural networks to optimise categorical indices. Logical comparison operators have been approximated using a sigmoid function, creating continuous and differentiable indices.

To extend these sigmoid functions, it is essential to develop differentiable versions of well–known categorical indices such as POD and POFD. Hence, this study demonstrates how to train models with these differentiable indices using gradient descent techniques and optimise their loss function in response to these techniques.

3.2. Case B: Pervasive Warming Bias in the Tropospheric Layers

3.2.1. Sample Assessment

Several studies [124–126] have noted a tendency among climate models to project excessive contemporary warming in the tropical troposphere. Additional evidence indicates a global tropospheric bias [127]. Here, it is essential to present an updated comparison between model reconstructions of historical layer–average lower and mid-troposphere temperature series and observational analogues from satellites, balloon-borne radiosondes, and reanalysis products. The first 38 models available in the recently released 6th generation Coupled Model Intercomparison Project (CMIP6) archive must be used.

Trends throughout the most extended period for which the three observational systems are known, 1979–2014, must be compared because these are the years for which the models were run using historically recorded forcings. If it were necessary to move the deadline forward to 2018, none of the findings would have changed. Examining four atmospheric zones is essential: the tropical lower and middle troposphere layers and the global lower troposphere and midtroposphere. Although there was usually a warm bias in earlier research, the spread of the model, particularly globally, partially covered the observed equivalents in large areas of air. However, this is no longer the case. All the models overestimated global warming in the lower and middle troposphere layers, both in the tropics and elsewhere. Most individual model disparities were statistically significant, and the discrepancies were highly significant on average.

3.2.2. Framework Algorithm

This section presents the temperature information collected from the main research organisations in the sector. At global stations, balloon–elevated thermistors measure radiosonde (or sonde) data that are subsequently radiated to ground stations. In this case, it is essential to use yearly averages at the typical pressure levels of 1000 (if above the launch site), 850, 700, 500, 400, 300, 200, 150, 100, 70, 50, 30, and 20 hPa, instead of the multiple temperature levels recorded by the sondes. Table 7 indicates that the three datasets are helpful in this regard. RAOBCORE + RICH [128], NOAA [129], and RATPAC [130]. In 2011, the commercial software used to analyse the sonde data was updated, leading to an estimated increase in humidity of several percent after 2009 [131]. This may be an artefact because it caused a small heat step that was not observed in other systems [132]. Since late 1978, a variety of polar-orbiting satellites have been equipped with microwave sensors to monitor air temperatures. The orbit of this spacecraft takes approximately 100 min to complete, circling Earth nearly pole–to–pole.

Because they were (and still are) sun-synchronous, Earth would revolve on its axis underneath the spacecraft as it orbited from pole to pole, allowing for the observation of almost the entire globe during a single Earth rotation (or day). These readings may be converted to temperature because the intensity of the microwave emissions from air oxygen is proportional to temperature. The emissions reflect the average temperature of the deep layer as they originate from the majority of the atmosphere. The lower troposphere (LT, surface of approximately 9 km) and mid-troposphere (MT, surface of approximately 15 km) are the two deep levels that must be the primary focus of this study. The monthly averages of both products were produced by Remote Sensing Systems (RSS) and the University of Alabama in Huntsville (UAH; [133]). Global MT data were provided by NOAA, whereas tropical MT values were produced by the University of Washington (UW) [134]. These datasets fall into a third group, called ‘reanalysis’. In this category, a multilayer global weather model absorbs as much information as possible from satellites, sondes, and surface measurements to provide a global representation of the atmosphere and surface that is consistent according to the model equations. The ability to obtain temperature data at 17 pressure levels, ranging from the surface to 10 hPa, and compute deep–layer averages that coincide with satellite readings is essential. Four of these datasets, JRA55 [135] from the Japanese Meteorological

Agency, two from the European Centre for Medium-Range Forecasts (ERA–I and ERA5; [136]) and one each from NASA (MERRA2; [137], provide an overall synopsis in this regard.

3.2.3. Machine Learning Analysis

The climate model simulations utilised here are those accepted for analysis in CMIP6, for which the models are executed in standardised simulations so that they may be appropriately inter–compared. It is imperative to obtain the model runs from the Lawrence Livermore National Laboratory archive [121]. For this assessment, it is imperative to use the period 1979–2014 of the simulation set that represents 1850–2014, in which the models were provided with 'historical' forcings. These time–varying forcings are estimates of the amount of energy deviation that occurs in the real world and are applied to the models over time. These include variations in factors such as volcanic aerosols, solar input, dust, and other aerosols; important gases such as carbon dioxide, ozone, and methane; and land surface brightness. With all models applying the same forcing, which is believed to have occurred for the actual Earth, a direct comparison between models and observations remains precarious (Figure 2(a–c)). The model–runs are presented in Table 8. It is also imperative to list the estimated equilibrium climate sensitivity (ECS) values for the 31 models for which it is essential to find the requisite values available in published or unpublished literature. Tables 9 and 10 show the global LT and MT data, respectively. A thick black line represents the model average, a thick blue line represents the observational mean, and the individual model runs are shown as gray dots (Figure 1(b,c)).

3.2.4. Empirical Validation

From years 1979 to 2014, the longest period for which all observational series were available and for which the models were run using observed forcings, linear trends were computed based on yearly data. Pretesting the temperature series for unit roots is essential because if they exist, they suggest non–stationarity, which renders traditional trend regressions incorrect [5]. The test form developed by Hari et al. [105], which permits an autoregressive lag and trend stationary alternative, must be used.

The series has a unit root and tests the null hypothesis. Because low power in such tests can lead to an under–rejection tendency in the presence of autocorrelation, it is essential to extend the time interval to 1959–2014. This means that the sonde record and the mean of the RAOBCORE, RICH, RATPAC, and UNSW products serve as observational series with this expanded period. The null hypothesis must be rejected for each model run and sonde mean series to show that the data may be regarded as trend–stationary. The robust autocorrelation approach is more suitable for building confidence intervals and hypothesis tests of trend equivalence [138].

3.2.5. Error Estimation

Trends pertaining to 95% confidence level (in °C/decade) for each of the 38 individual climate models, the ensemble mean of the climate models, and the three mean observational series are shown in detail in Grose et al. [139], Pathirana et al. [140] and Velasco Hererra et al. [141] studies (i.e., in terms of radiosondes, reanalysis, and satellite data). Varying in these data is the result of a combination of observational series with different data availabilities. The average of the sonde data included UNSW in the MT layers and RAOBCORE, RICH, and RATPAC for all parameters (global and tropics). The global LT topical LT and MT layers were measured using the ERA–I, ERA5, JRA55, and MERRA2, whereas the global MT layer was measured using ERA5, JRA55, and MERRA2. For the global LT, MT, and topical LT, the mean of the satellite data employs UAH and RSS. Tropical MT also uses NOAA and UW. MT layer findings for global and tropical samples have been reported in a previous study [142]. The LT layer is the same as that in the bottom row. Regardless of how they are quantified, it is evident that every model run for every regional and layer average has a mean trend that is greater than the corresponding actual trends. The three averages of the observational system, average of all models, trend coefficients and symmetric 95% confidence level widths (in °C/decade) for each model are listed in Tables 7 and 8. For example, the ACCESS model (Table 9) shows a worldwide trend of 0.250±0.103 °C/decade. The Vogelsang–Franses test results for each test area are shown in Table 10 under the null hypothesis of trend equivalency. At the 90% confidence level, a number higher than 41.53 was considered noteworthy. The results of determining whether the average model trend outperformed the average sonde trend are presented in the first row. The matching result for the reanalysis data is shown in the second row, whereas the results for the satellite data are shown in the third row. The number of individual model–runs where the trend significantly outperformed the satellite average is shown in the fourth row. It is crucial to note that all 12 tests were rejected in the first three rows. This indicates that, regardless of the observational measurement method, area, or atmospheric layer, the average model significantly outperformed the intermediate observed series (Figure 2(b–d)). For the global LT example, where 18 of the 38 models reject, the last row demonstrates that the majority of models also reject separately when compared to the satellite data. The total would still be 24 and 26, respectively, for the global LT and MT layers, increasing to 22 and 23 in the tropical LT and MT layers, respectively, if it were necessary to extend the data sample to the end date of 2018.

3.2.6. Sensitivity Analysis

Examining 'emergent constraints' is becoming an increasingly popular type of model diagnosis [143]. Model–to–model variations in ECS values indicate that the measurements cannot be used to identify the exact value. The search for observable climatic variables with quantifiable equivalents in models connected to the ECS model is the idea behind the emergent constraint notion. Therefore, ECS values are more likely to be accurate, as revealed by the observed correlation measurements. Several metrics have been proposed, including the total cloud fraction between the tropical and southern hemispheres at mid-latitudes, the fraction of low clouds with tops below 850 mb that are also below 950 mb, and the relative humidity in the moist–convective region (Table 11). There is considerable variation in the correlations between the suggested measures and the ECS, and many of them lack a sound physical basis. Analysing the model warming rates here is crucial because they are directly related to the ECS (Figure 3(a)). Therefore, it is interesting to examine whether an emergent constraint interpretation can explain these findings. The trend terms LT–global 0.67, MT–global 0.60, LT–tropics 0.50, and MT–tropics 0.50 have the following relationships with ECS. Because they are more likely to be realistic, models with low ECS values often exhibit lower tropospheric trends and are consequently closer to the observed values. The study by Nazarian et al. [144] provides more context for the results. Depending on whether the ECS is above (shown by red squares) or below (represented by blue circles) 3.4 K, the models cluster into two different groups. The solid square or circle indicates the LT trend, whereas the open form indicates the MT trend. Layer averages are connected by gray lines (solid–LT, dashed–MT), which symbolise the emerging constraint, and the mean values in each cluster for the LT and MT layers are denoted by + signs. The ECS and warming trend values do not correspond within the clusters, but a connection appears when comparing low and high clusters, as the grey lines show. The mean ECS is 4.67 K and the overall mean trend is 0.28 °C/decade in the high group. The mean ECS is 2.76 K and the general mean trend is 0.21 °C/decade in the low category. Arrows along the horizontal axis represent the mean observed trends in the LT and MT layers across all measurement types (LT solid 0.15 °C/decade, MT open 0.09 °C/decade). The emerging restriction suggests that, to roughly match the data, one must extrapolate to even lower ECS levels because the mean trends, even in the low–ECS model group, are still too large (Figure 3(b)). To what extent would this extrapolation be determined by looking at the points where the dotted lines intersect the arrows; nonetheless, as depicted, this suggests that the ECS values are considerably below 1.0 K. Because any curve shape can be fitted between two points, concave lines can also be used to obtain related warming patterns that are compatible with the data. However, this still indicates that the ECS values were below 2.0 K.

4. Results and Discussion

The Linked Model Intercomparison Project (CMIP) was developed to investigate and evaluate climate simulations performed using coupled ocean-atmosphere–cryosphere–land GCMs. There are two primary stages (CMIP1 and CMIP2) that explore, respectively, (1) the capacity of models to replicate present climate and (2) model simulations of climate change owing to an idealised rise in forcing (1% annual increase). The inaugural CMIP Workshop held in October 1998 in Melbourne, Australia, reported the results of many CMIP initiatives, wherein the latest developments in global coupled modelling of CMIP have also been highlighted. The group study was based on preliminary unpublished research as well. The workshop revealed that global coupled models can simulate many observed aspects of climate variability, such as the North Atlantic oscillation and its linkages to North Atlantic SSTs, El Niño–like events, and monsoon interannual variability.

Additionally, the amplitude of both high– and low–frequency global mean surface temperature variability in many global coupled models is less than that observed, with the former due in part to the simulated ENSO (although still with some systematic simulation errors). This article explains the process and key aspects of creating representative concentration routes (RCPs), a collection of four novel pathways created by the climate modelling community to serve as a foundation for long– and short–term modelling experiments. The four RCPs cover the radiative forcing levels known in the open literature for the year 2100, ranging from 2.6 to 8.5 W/m^2. RCPs are the result of a new partnership of integrated assessment modellers, climate modellers, terrestrial ecosystem models, and emission inventory specialists. The final output is complete data collection with high geographical and sectoral resolutions, covering the period up to 2100. Land use and emissions of air pollutants and greenhouse gases are generally given at a 0.5° × 0.5° spatial resolution, with air pollutants also supplied by sector (for well–mixed gases, a coarser resolution is used). The underlying outputs of the integrated assessment model for land use, atmospheric emissions, and concentration data were aligned across models and scenarios to guarantee agreement with historical observations while maintaining unique scenario trends.

For most variables, the RCPs include a wide range of extant studies. The RCPs are augmented by extensions (Extended Concentration Pathways, ECPs), which allow for fast reductions in these indices before slowing and stabilising toward the conclusion of the training period. In previous generations of climate models, it is well known that the tropical troposphere has warmed at excessively high rates. It is critical to update the comparison so that the CMIP6 Climate Model Repository is accessible. Analysing the historical (hindcast) runs of the 38 CMIP6 models with forcings based on historical data is critical. It is critical to focus on the period from 1979 to 2014, as this is the longest period for which all models and observational data are available and historical forcings were used while running the models. There is now a global bias toward what was formerly tropical. Every model warmed faster than observed globally, particularly in the tropics and the lower and middle troposphere. The trend difference was significant in most individual cases and on average. The Model Equilibrium Climate Sensitivity (ECS) tends to grow with warming trends in the models; thus, it is vital to demonstrate that the ECS values of the model are distributed in an unreasonable manner. It has long been known that climate models tend to overstate warming in the tropical troposphere. To show that warm bias is now evident globally, Aizawa et al. [145] assessed individual runs from 38 newly released Coupled Model Intercomparison Project version 6 (CMIP6) models and compared CMIP6 experiments using satellites, weather balloons, and reanalysis product observational data. Because this is the largest time span for which full observational data are available, Boer et al. [146] focused on the 1979–2014 period, for which models were run using historically reported forcings. The 38 models overpredicted warming in every target observational analogue for the lower– and mid–troposphere layers globally and in the tropics, sometimes significantly, and the average differences between the model and observational data were statistically significant. Hibbert et al. [147] provide evidence that the observed warming trends demand lower model equilibrium climate sensitivity (ECS) values.

Although the real world has warmed in a distinct way, this number can only be estimated because of spatiotemporal incompleteness and unknown biases in the available data. Chen et al. [148] provide a way to combine the range of available items in the best possible way to get an updated estimate. This method, like any similar method, makes assumptions about available estimates. This is a representative and objective selection from a population of plausible alternative estimates that might have been made. There are several reasons for this finding. A different strategy is to employ more straightforward methods, as explained in the IPCC report. In particular, these strategies guard against underestimating the real uncertainty in the evolution of global surface temperatures and the future-proofing current estimates against new datasets that have come from advancements in our knowledge.

Brimicombe et al. [149] created a post–millennium mid–tropospheric temperature time series using continuous measurements from sophisticated microwave sounders on satellites in a stable sun–synchronous orbit. These data have great radiometric stability and do not exhibit diurnal sampling shifts over time, enabling the creation of a combined time series from many satellites with an accuracy higher than 0.012 K/decade.

The generated time series is of great precision and can be used as a reference measurement of climatic variability and atmospheric temperature trends. The warming rate for the atmospheric layer has been measured to be 0.230±0.134 K/decade from 2002 to 2020, which is ∼14% greater than the previous satellite microwave sounder datasets. These findings shed fresh light on the trend disparities between microwave sounder temperature datasets created by various research groups and aid in reconciling the trend differences between satellite observations and climate model simulations. For the last decade or two, land-based compilations of gridded monthly surface air temperature anomalies averaged into hemispheric values over the past 140 years have been accessible for climatological investigations. The research methodologies employed in their development, notably the need for a common reference period, make it impossible to retroactively add any new temperature datasets currently available for certain nations. Therefore, despite some advances in data availability, the number of stations included has decreased since 1970, both in hemispheric averages and in their component grid–box datasets.

The current work reanalysed existing and newly accessible temperature records to create a grid–box dataset containing 5° × 5° temperature anomalies. The reanalysis includes over 1000 more stations (2961 in total), mostly spanning the period from the 1920s to the 1990s, but also stops the reduction of stations integrated in real-time for the most recent years. This study for the period 1991–1993 includes 252 additional stations compared to previous assessments. However, the reanalysis was intended to be more than simply produce hemispheric averages. Because of the increased number of stations, the grid–box dataset should be able to estimate the time series at small sub better–continental scales (Figure 3(c)). The results for the Northern Hemisphere average did not differ significantly from those of earlier research despite a significant increase in the number of stations used. This suggests that the earlier data are still reliable. In total, 109 stations yielded comparable results. The results revealed notable (albeit still quite small) differences from earlier evaluations throughout the Southern Hemisphere, particularly over continental regions. This paper presents a framework for improving neural network models for precipitation forecasting using a combination of continuous and categorical binary variables. The probability of detection or false alarm rate is a useful measure for verifying the precipitation models. However, these measures cannot be used to improve machine learning models trained using gradient descent because they are not differentiable. Nazarian et al. [144] provided a new formulation for these differentiable categorical indices and demonstrated how they can be utilised to improve the performance of precipitation neural network models as multi-objective optimisation problems. To the best of our knowledge, this is the first approach to optimise weather neural network models using categorical indices. The propensity of climate models to exaggerate warming in the tropical troposphere has been extensively documented. Ladstädter et al. [150] evaluated individual runs from 38 recently published Coupled Model Intercomparison Project version 6 (CMIP6) models to demonstrate that warm bias is now visible worldwide. O'Neill et al. [151] compared CMIP6 experiments with observational data obtained from satellites, weather balloons, and reanalysis products. Shanmugam [152] focused on the 1979–2014 period, which is the longest span for which all observational data are available, and the models were run using historically recorded forcings. For the lower and mid–troposphere layers, both worldwide and in the tropics, all 38 models overpredicted warming in every target observational analogue, sometimes considerably, and the average disparities between models and observations were statistically significant. Kalicinsky and Koppmann [153] showed that lower model equilibrium climate sensitivity (ECS) values are required to match the observed warming trends. Recently, deep neural networks have been shown to be versatile and capable of modelling complex issues. These methods have been used in weather modelling to address various problems. With the availability of vast amounts of meteorological data and advances in computing power, this field of study shows great promise. A measure that the model seeks to maximise may be used to teach neural network models to solve problems. Selecting the parameters that the model should optimise may be difficult because a wide range of metrics is used to assess the quality of weather models. Categorical binary metrics are frequently used for evaluating the quality of precipitation in a model. These metrics convert precipitation into a binary event (‘yes’ or ‘no’), allowing for a comparison between the predictions made by the prediction model and actual observations. Numerous indicators and statistics have been established to evaluate various elements of precipitation model quality, making this technique simple but effective. Improving models based on these binary measures is extremely straightforward because precipitation models are often evaluated using them. Unfortunately, these measures are inappropriate for optimisation because of their mathematical characteristics. It is essential to provide a different formulation of these categorical binary indices in this section so that the models can be trained using them. Training a deep learning model is necessary to demonstrate how improved precipitation data can be produced.

5. Optimisation Prospects and Challenges

5.1. Collaborative Efforts

With the 2015 UNFCCC Paris Agreement, which committed to maintaining temperatures below 2 °C and aimed to keep them below 1.5 °C above preindustrial levels, the question of how much the global surface temperature has changed since preindustrial times has become more important from a policy perspective [154]. This aligns with global surface temperature, a key indicator of changes in the geophysical system, with clear global climate mitigation objectives for the first time. Regardless of the more general debate on the sociological and practical importance of the global surface temperature measure, it directly affects policies. Policy choices related to adaptation requirements and mitigation objectives are costly in billions of dollars and have a significant impact on people's lives and means of subsistence. Today, many of these are directly or indirectly related to changes in the temperature of the Earth’s surface.

Assessment of changes in global surface temperature is hampered by the scarcity and frequent discontinuity of available measurements, with specific locations persistently under or worse than unsampled locations [155]. The number of observations that are now accessible has changed over time, and early records have become scarce. Additionally, they have time-varying biases that must be corrected before being used in long–term climate applications because of modifications to the apparatus, siting, and observational techniques [156]. Most of the time, metadata, which may be very helpful in physically separating which biases exist and why, is either severely lacking or completely nonexistent. Consequently, it is usually uncertain when and what kind of breaks a series could experience. As a result, creating a climate data record is fundamentally statistical and ill-posed, as the data are scarce, and the nature and place of the biases within the series are unknown at the outset. These data are typically stored in international repositories [96–113]. Research groups use these data, select specific data, evaluate the homogeneity of land and marine holdings, combine them to produce globally comprehensive estimates, and post-process to consider data-sparse regions and epochs as much as is practical for generating datasets. Many organisations have estimated changes in global surface temperatures, which have been updated and corrected regularly [157]. The products have included an increasing variety of data problems and have grown more globally comprehensively via interpolation methods owing to increasing knowledge about the data and the introduction of new computing techniques and capabilities over time. An estimate of the structural uncertainty of global surface temperatures can be obtained from various datasets.

Furthermore, a growing number of products quantify parametric uncertainty estimates that arise from uncertain decisions and assumptions made within the specific approach. These are often stated in terms of ensembles of ‘equiprobable’ solutions. The urge to choose the best estimate from available estimates is natural and logical. There are significant practical and policy advantages to a more limited and less–biased assessment. Since all forecasts claim to be estimates of the same geophysical quantity and since that quantity must have evolved in a single, distinct way in the real world, one may naturally wonder if a better estimate can be obtained using the weighted combination method suggested by Phan and Fukui [158]. The issue is whether this is justified, and it essentially depends on whether the presumptions regarding whether the sample of available estimates reflects an unbiased and representative draw are true.

In theory, hundreds or thousands of estimates of changes in global surface temperature can be produced if enough people are trained and provided with funding to work on the issue in a quasi-independent manner. These estimates were created using various methods to choose, adjust, and post-process the data. An implicit and fundamental presumption of the Yamashkin et al. [159] approach, as well as any other approach that uses a weighted average to conclude the still–small but increasing pool of feasible estimates, is that the forecast is both impartial and representative of the larger population of estimates that could theoretically exist.

In this case, representative refers to the fact that they fairly cover the entire range of such credible estimates, and unbiased refers to the fact that the draw does not favourably depart from any part of this fictitious parent distribution. This parent distribution is hypothetical. It is necessary to be ignorant of the actual distribution, and if knowledge of it is available, it would be required to utilise it, rendering the whole conversation pointless. This natural distribution is unknown because of the nature of the accessible data and metadata.

Nevertheless, there are several indicators you just must be aware of that indicate a high level of prudence is necessary. First, it is crucial to understand that there is a significant amount of scientific cross-dressing among the currently available estimates, meaning that the true methodological degrees of freedom are lower than what can be inferred from simply counting the number of estimates that are now available [160]. For example, the selection and standardisation of land and marine data used to create the NASA GISTEMP and NOAA GlobTemp products is the only distinction between the two products in many cases. In some scenarios, the approaches are substantially independent in every way, such as HadCRUT and NOAA GlobTemp. The possibility that the available estimates constitute a truly unbiased draw is very low because they are essentially derived from just 3–gridded homogenised forecasts of changes in sea surface temperature (HadSST; [161], ERSST; [162], and COBE–SST; [163]) and 3–gridded–homogenised estimates of land surface temperatures (GHCNM; [164], CRUTEM; [165], and Berkeley Eaandth; [166]).

The estimates were then combined and processed. The regions of distribution originating from the locations inhabited by these underlying land and marine goods are preferred in the estimations (Figure 4(a)). Second, it is critical to understand that the estimations can only be partially corrected for data biases. The remaining problems with marine data biases and accounting for regular data–short places were brought to light at the time of the IPCC Fifth Assessment Report [167].

Regarding these two concerns, the updated estimates evaluated in the subsequent IPCC report increased the estimates by 0.08 °C, or around 10%, of the long–term increase projected at the time of the previous assessment, using a like–by–like measure [168]. To think that all real (as opposed to currently known) biases have been found and considered too naive. It is necessary to assume that past evaluations are biased; however, it is not guaranteed that the current generation of estimates will remain impartial in light of new information.

Furthermore, it is recognised that some of the forecasts that are already available, such as those derived from the JMA, may be skewed as they have not yet considered all of the new information. It is wise to treat current estimates as snapshots based on current information that could be susceptible to modifications that might later become significant.

Third, although it is necessary to use benchmarking evaluations against fictitious scenarios where a proper response is known to draw certain conclusions, it is equally essential to be able to determine the performance of various components of dataset generation algorithms in the real world. The most developed use of these benchmarking evaluations is the homogeneity of the meteorological land stations. They discovered that, in this case, the top–performing algorithms tend to move the data closer to the truth, but more is required over the entire network [169]. Current methods perform better when there are few data points and frequent tiny breaks. These benchmarking investigations highlight the possibility of shared residual biases between independent homogenisation techniques [170]. Finally, a more direct comparison with parametric uncertainty estimates is required, considering various sources of uncertainty, often in different ways. The estimates may be over– or under–dispersive, even when the sources of uncertainty are theoretically considered using other techniques [171]. Thus, integrating or using these uncertainty estimates to obtain a combined estimate is significantly more complex than using best estimates alone.

It is unreasonable to assume that the estimations are either complete or similar. More confined forecasts, in particular, often indicate either omitted uncertainty factors or under–dispersive estimations rather than superior constrained estimates over a wide range of climatic datasets [170]. When combined, these lines of evidence seriously challenge the presumptions surrounding the estimates that are currently accessible and provide an objective and representative sample from the population of credible forecasts. This finding should be interpreted with caution. It is not that the world has warmed; instead, the uncertainty lies in the specifics of the warming. Artefacts and uncertainties that are several orders of magnitude larger than those currently accounted for and documented are necessary to cast doubt on the idea that the world has warmed since the late 19th century. It is also necessary to explain the quantifiable changes in various other crucial climatic indicators, which are all consistent with a global warming climate [172]. Romdhani et al. [173] used a different strategy in light of the policy importance of the global surface temperature metric and concerns regarding whether the current estimates reflect an unbiased and representative sample. First, predictions based on land surface temperature and sea surface temperature estimates that are known to be outdated and have residual (known) biases were filtered out. The best estimate was then determined by taking a simple average of the remaining estimates. This reduces the possibility of weighting often and consistently skewed estimates but still needs to be eliminated. Finally, the maximum and lowest values of the available parametric uncertainty ranges were chosen to establish conservative limits on the estimated uncertainty of the evaluated change, thus minimising the likelihood of the real value falling outside the stated range. This methodology not only makes the IPCC report easy to read for consumers but also significantly reduces the likelihood that the actual, unknowable, global surface temperature rise in the real world would deviate from the extremely probable range (where it is very likely to have a particular meaning and represents a range of 5–75%). This, in turn, guarantees that the entire possible range of values for the change in global surface temperatures to date is carried over to later evaluations concerning essential issues such as estimates of equilibrium climate sensitivity, quantification of remaining carbon budgets [174], and when specific levels of global warming may be reached [175].

Scientists have regularly utilised laser altimeter data from Clementine orbits 270 and 272 and retrieved the heights from the stereoimage–derived DTM at the laser return spots to validate the elevation of the terrain models. [154–163] An excellent agreement was observed between the heights of the two datasets [176]. Minor residual ambiguities in the camera aiming during block correction cause a systematic offset in the absolute height of approximately 300 m. The disparity between the matching patches, short laser altimeter footprint size of approximately 200 m, and vast Galileo image pixels account for the dispersion between the two. According to this comparison, the stereo picture data may provide better resolution topography information between the sparsely dispersed laser return points. In contrast, laser altimeter data can be used to determine absolute altitudes (Figure 4(b)). The capacity to obtain high–resolution topography of the lunar surface has increased significantly with the introduction of charge-coupled device (CCD) cameras and the development of photogrammetric processing of digital pictures. With new data, lunar scientists may be able to trace the rings and ejecta blankets of impact basins on the moon. This information can also provide information on the dynamics of impact events and the subsequent formation processes of viscous relaxation, rebound, and lava emplacement. Using topographic data, scientists may more accurately calculate the solar incidence and emission angles of surface slopes, make exact photometric adjustments to pictures, and perform trustworthy compositional interpretations.

According to H. Chen et al. [177], deep–space mission designs should consider stereo images. Care must be taken while planning the viewing and lighting conditions of image sequences, as this may make it more difficult to identify features and cause automated stereo analysis methods to malfunction. Large–pixel array cameras are the best choice because they have lower processing costs and increase the stability of the terrain models. Even better, it would be beneficial to operate separate stereo cameras for almost simultaneous multi–look imagery, which would enable scientists to replicate the three–dimensional spread of the global climate. Projections of future climate change caused by human activities were made using these models. Simulation results are often used to pinpoint weaknesses and assess social effects that influence policies. Therefore, the scientific community must systematically assess the simulation capacity. In the Coupled Model Intercomparison Project (CMIP), the worldwide coupled climate modelling community evaluated the ‘state of the art’. The World Climate Research Programme coordinates this effort with the Climate Variability and Predictability Initiative (CLIVAR).

The first phase of the CMIP (CMIP1, initiated in 1996) aims to quantify the effects of flux adjustment (additional correction terms applied to quantities exchanged between component models at the air-sea interface to maintain a state close to that observed) on coupled simulations of mean climate and climate variability, as well as features of simulated climate system variability on a range of time and space scales. Systematic simulation errors of global coupled climate models in the atmospheric, oceanic, and cryospheric components must be documented.

The second phase of the CMIP, known as CMIP2, has recently begun and will involve comparing global coupled model experiments with atmospheric CO_2 growing at a compound annual rate of 1%, with CO_2 doubling every 70 years out of an 80–year period. The objectives of CMIP2 are to quantify the effects of flux adjustment on climate sensitivity in coupled climate simulations, highlight the characteristics of the simulated time–evolving climate system response to gradually increasing CO_2, and document the mean response of the dynamically coupled climate system to a transient increase in CO_2. in the models near the time of CO_2 exposure doubling. The goal of diagnostic subprojects is to assess coupled model simulations by comparing them to the best available data and analysing processes, phenomena, and area features. Such global coupled climate models represent the finest effort to predict Earth's climate system. By computing time-varying solutions of the governing equations for the atmosphere and ocean, these complex numerical/physical formulations of the atmosphere, ocean, sea ice, and land can mimic the climate. For many years, these equations have advanced, enabling models to predict future climate change caused by human activity. Global climate models (GCMs) require considerable computational power.

For example, it takes approximately 1000 h to simulate 100 years of climate on a contemporary supercomputer using a standard worldwide linked model. The models simulated the first–order components of large–scale regional climate and variability quite well simulated by the models, notwithstanding some simulation flaws. Currently, the principal instruments for studying the issue of human climate change are such models. The simulation capabilities of these models need to be thoroughly evaluated, as simulation findings are often used to pinpoint vulnerabilities and evaluate the societal effects that influence policy. This is the job of the

CMIP. Eighteen global coupled models from Australia, Canada, France, Japan, Germany, the United Kingdom, and the United States provided data for the first phase of the CMIP, representing every country in the world using a functional global coupled climate model. The Intergovernmental Panel on Climate Change (IPCC), which organises worldwide assessments to provide policymakers with the best estimates of potential future climate change due to human activity, uses the findings of several models that CMIP routinely compares [178].

Starting in 1996, the main goal of CMIP1 was to record systematic simulation errors in globally linked climate models. This was achieved by assessing how effectively the coupled models replicated the current mean climate by comparing the mean model output with observations. The differences between the observed and simulated values indicate systematic errors. These inaccuracies highlight the places and manner in which the models fall short of accurately simulating the behaviour of the land surface, sea ice, atmosphere, and ocean in the present climate. For example, warmer than the observed sea surface temperatures along the west coasts of subtropical continents are a typical example of systematic inaccuracy [179].

Usually, sub–par modelling of low–level stratocumulus clouds causes this inaccuracy. In some areas, there is insufficient cloud cover, which allows too much sunlight to reach the ocean surface. The sea surface temperature exceeded the recorded values. The heat, freshwater, and momentum fluxes between the ocean surface and atmosphere allow interaction. Net radiation, the temperature of the air surface layer above, precipitation, evaporation from the surface, and the wind force operating on the ocean surface influence these fluxes. The distribution of snow, soil moisture, sea ice, and surface temperatures affects the atmosphere from the ocean, sea ice, and land surface. When the model components are coupled, errors in the fluxes and associated surface conditions lead to errors in the linked climate simulations of temperature, pressure, moisture, wind, ocean currents, and rainfall. A method known as flux adjustment (sometimes termed ‘flux correction’) is occasionally used to address these simulation inaccuracies and to improve the agreement between coupled climate simulations and observations. This method is used in approximately half of the linked models in the CMIPl. The purpose of flux modification is to improve the agreement between the coupled model simulation and data. As a result, the fluxes between the model components were modified by constant additive factors rather than by interactive or restorative effects.

Consequently, the model is free to deviate from the current climate because terms are introduced and the model does not return to any observable condition. In the above scenario, flux adjustment was computed to lower the heat flow into the ocean if there were insufficient low–level clouds. Consequently, the sea surface temperatures would better match the measurements and would be slightly colder. In model simulations of past, present, and future climates, the flow adjustments are constant once they are determined. To accurately represent disturbances, flux adjustment ensures that the physical climate feedback in the models functions within an appropriate climatic range. For example, ‘albedo feedback’ plays a significant role in climate change. Surface albedo decreases due to snow and ice melting caused by surface warming. This creates a feedback cycle where more snow and ice melt, the surface is heated owing to increased absorption of incoming solar radiation, and so on (cooling drives the loop in the opposite sense). The type of reaction to a disturbance in the climate will change depending on the amount of snow and ice in the control environment that the models replicate. Most coupled models that include flux adjustment replicate the current climate better than models that do not, as they improve the coupled model simulation's agreement with observations.

However, before the flux adjustment approach is utilised in linked simulations, the various component models used by different modelling groups tend to exhibit comparable systematic simulation errors. The climate simulated by anunflux–adjusted model may be jeopardised if the feedback in a nonflux–adjusted coupled model (e.g., albedo feedback) is impacted. However, the amount of flux adjustment indicates how poorly the component models match, as is the case in a simulation with an excessive number of low–level clouds. These discrepancies may conceal the absence of a physical feedback mechanism in the linked system (Figure 4(c)). Evaluating the potential implications of flux adjustment in coupled climate simulations is CMIP1's second goal. The goal of linked modelling groups is to remove flux adjustments while maintaining a reasonable representation of the current climate.

By recording the features of climate simulations across models with and without flux adjustment, the CMIP will help this process. The third goal of CMIP1 is to evaluate the capacity of these coupled models to replicate surface air temperature fluctuations. This includes temperature fluctuations over decades and longer durations, and seasonal to interannual variations. Understanding the mechanisms and processes behind climatic fluctuations, measuring climate variability to identify changes in observational records, and forecasting how variability may change in response to climate change is possible. The ‘fields’, or model–simulated quantities, that CMIP1 sought to build upon those used in an assessment conducted by Boer and Lambert [180].

The temporal mean geographical distributions of terms on Earth's surface are among the fields; they show how the constituent parts of the coupled system interact. Examples include surface winds, temperature, moisture, freshwater, momentum, and heat flux. Mean measurements of the latitudinal and vertical structures of variables, including temperature, winds, and currents, are sometimes gathered.

A broad assessment of climatic variability was conducted using a time series of monthly mean surface air temperature. The recently launched CMIP2 has similar goals to CMIP1 but applies them to climate change experiments carried out by coupled models where CO_2 increases at a compound annual rate of 1%. As a result, the mean climate change, the impact of flux adjustment on the simulated climate changes, and elements of the simulated anthropogenic climate changes that vary over time will all be used to assess the sensitivity of the model climate to human forcing. The number of fields requested in the CMIP formulation was limited to a subset of all fields that the models could output. As previously indicated, CMIP is a targeted coupled model intercomparison with particular goals that require a reasonable amount of work from participating organisations.

A longer list of the model results can be considered later. Furthermore, time series of a few fields from selected sections of the coupled model integrations were gathered for two distinct coupled model intercomparisons: the El Niño Southern Oscillation Simulations in Coupled Models Project (ENSIP) and Assessment of Tropical Oceans in Coupled Models, which concentrate on particular coupled model processes (STOIC). Collecting coupled model data may provide a basic intercomparison of model behaviours. However, more comprehensive data analysis can only be performed in collaboration with a larger climate research community. Therefore, although the CMIP does not provide direct financing, the CMIP Panel seeks applications for diagnostic subprojects. The panel will work to ensure that each accepted subproject has scientific quality, a high likelihood of success, and proper coordination with the modelling community and other approved subprojects. Diagnostic subprojects aim to assess coupled model simulations by comparing them with the best available data and analysing processes, phenomena, and regional features. Whether condensation trails from the increasing number of passengers and other jet aircraft [181] change Earth's radiation balance sufficiently to affect local weather patterns and the global climate [182] is an incredible interest today.

Numerous studies have suggested that contrails may have localised consequences, even if no worldwide implications have been identified. Su et al. [183], for instance, hypothesised a potential connection between jet aircraft contrails and a drop in the midwestern United States' daily maximum and lowest temperatures. The cirrus, which originates from the contrails, has also been observed to reduce the warmth of a dwelling heated by sunlight [184]. Recent investigations have focused on measuring the nature, content, and development of the gases and aerosols that produce contrails [185]. The buildup of these combustion by-products may eventually impact Earth's radiation balance. The latest study, SUCCESS by NASA, presented its findings at the AGU Spring Meeting in Baltimore. At the conference, contrails were not found to have significantly influenced global climate. However, there were hints of decades-long localised impacts from repeated contrail occurrences.

It is well known that contrast overcasts have the potential to inhibit nighttime cooling rates, similar to cirrus clouds. It is crucial to ignore any published analysis; nevertheless, it links localised temperature drops throughout the day to the aerosol optical thickness (AOT) of the contrails and overcasts of the contrails. Reductions in daytime temperature and diurnal temperature range (DTR) linked to localised contrast overcasts may be explained by measured decreases in direct solar and global solar irradiation. The AOT of a typical contrail above Fairbanks, Alaska, on 20 August 1996 was reported by Tanaka et al. [186]. On each side of the contrail, the largest increases in AOT over the background quantity of the blue sky are 0.15 at 376 nm, 0.17 at 540 nm, and 0.16 at 680 nm, respectively. The mean AOT of thin cirrus clouds at noon in South Texas during the 12–day period in 1996 was comparable to these values. The mean increase in AOT on these days over the background AOT on the closest clear sky days is 0.15 at 680 nm and 0.20 at 540 nm (376 nm not measured). Consequently, in South Texas, where contrails are rare, the measured AOT of a contrail in a clear Alaskan sky is similar to that of a thin cirrus. An individual contrail passing by the sun has a momentary impact on AOT inside the shadow zone. However, long-lasting and widely dispersed contrails may mimic naturally occurring cirrus overcasts and have a considerable effect on surface temperature. Analysis of National Weather Service data shows that during a widespread event of staying in contrails over the midwestern United States on April 18, 1987, the average maximum surface temperatures near the centre of the contrail region were 2.4 °C cooler than in surrounding locations just outside the contrail region [187]. Additional analyses of the30–year DTR normals for the United States before and immediately after the sharp increase in air travel that started in the early 1960s showed a strong direct relationship between the regions believed to have received the most contrail coverage and the areas that saw the most significant declines in DTR [188]. This could explain the differently distributed regional decline in the US [189]. Further research is necessary to gain a deeper understanding of the physical foundation of this statistical correlation. Recent ground measurements of lower solar irradiance due to a contrasting cloud in Lausanne, Switzerland, on 4 November 1996 provided evidence of a significant impact on the daytime radiation budget. At noon, the sky, which was otherwise clear, had become almost cloud–covered because of many obstacles. Global (full sky) and diffuse solar irradiances were measured at noon.

5.2. Statistical Inference

Three organisations have been keeping an eye on surface air temperatures over the terrestrial regions: the Climatic Research Unit ([190], henceforth denoted as CRU); the Goddard Institute for Space Studies [191]; and the former Soviet Hydrometeorological Institute [192]. The findings on the hemispheric averages were in excellent agreement despite the differences in the actual number of stations utilised and the analytical methodologies used. This is because much data is shared [193]. Several data analyses have been conducted in this regard [194]. These assessments aim to re-examine, enhance, and modernise the CRU's gridded land-based temperature database.

Such attempts are typically made for three reasons. The first two justifications address data accessibility. In addition to requiring homogeneity in the station temperature time series [195], the original CRU analysis required that each time series be available for a standard reference period (1951–1970) at all the stations. Some areas started recording in the 1950s, even though some stations missing this period of data had reference periods approximated from the surrounding data (e.g., parts of the Middle East, the Russian Arctic, some interior parts of South America and Africa, and the whole of Antarctica). Feldman et al. [196] described a process for adding Antarctic data; however, this did not closely follow the reference period 1951–1970. The primary motivation for the reanalysis was to include station data for these areas using a longer direct and new reference period (1961–1990) that all stations share. Including several additional station records gathered from other nations while working on other projects was the second justification.

Efforts to create station temperature series with maximum and lowest temperatures have been the primary source of supplementary station data [196]. The goal of collecting these data was to identify the factors that contributed to global warming in the 20th century. The minimum temperatures increased more quickly than the maximum temperatures, according to data from Fiedler et al. [197]. Ideally, there should be two independent studies on the current reanalysis of these two temperature extremes. Unfortunately, only 37% of Earth's surface area is covered by stations that provide data on monthly mean maximum and minimum temperatures in terms of space and time. Such statistics were available for only a few nations before the 1930s. Although people and the World Meteorological Organization have made efforts to remedy this situation, the average monthly temperature remains the most accessible measure of the thermal environment. The potential applications of the data are subject to a third justification. To produce 5° × 5° box values for as much of the planet as feasible, the original CRU data (gridded on a 5° latitude × 10° longitude) were coupled with marine 5° × 5° grid–box data (sea surface temperatures) in anomaly form [198]. Consequently, the grid box values were reported as anomalies for the reference period of the marine data from 1950 to 1979. By adding the monthly difference between the grid box values for 1950–79 and 1951–70, the land data were corrected for this era. Although this modification of the land data might result in minor distortions at the local grid box level, it is appropriate for large–scale averages and research. Consequently, the goal of such calibrations is to provide grid box values at a 5° resolution for easy integration with maritime data in the future. The improvement in the regional series derived from the gridded data and the ease of comparison with the outcomes of general circulation model experiments are two other reasons for the finer resolution and grid–box format.

In conclusion, the goal is to reanalyze the monthly mean air temperature series of the stations, using more than 1000 stations than in the past and using a 5° box resolution with a 1961–1990 reference period. In the CRU, there were initially 1873 stations in service (1584 in the Northern Hemisphere and 289 in the Southern Hemisphere). For the reference period values of 1951–1970, all stations had sufficient data to calculate or, in some cases, correctly estimate from nearby stations. Furthermore, data from 16 Antarctic sites were added, referencing to 1957–1975 period [199].

This new research includes more data for the 1873 original stations used by CRU and data for 1088 additional stations, for which reference period values were derived for 1961–1990. Some of these data were obtained from other programs [200]. It included updates of some of the 1873 station series that needed to be regularly updated by the WMO's CLIMAT network or Monthly Climatic Data for the World, in addition to the newly obtained stations. Furthermore, additional stations from regular sources started recording in the late 1950s and now have sufficient data to establish an average for the 1961–1990 reference period. Among them are Antarctic stations. In a previous study, none of these extra stations was previously disqualified as non–homogeneous [201].

Because various national techniques for computing monthly mean temperatures and station altitudes vary, the use of a reference period is necessary for interpolation [202]. A station must have data for 21 out of the 30 years (per month) to be included. None of the original 1873 station series met this criterion during the 1961–1990 period. Attempting to improve coverage in the 1980s was one of the goals of this study. However, only 974 stations (52% of the total) in the original CRU series received regular updates by the end of these decades. This number decreased to approximately 700 in 1992. Thus, the values for the 1961–1990 reference period were only partially calculated to preserve a portion of the original 1873 stations. Because all 1873 sites had data for at least 1961–1970, the estimate was only partially accurate.

Because much of the data were updated from additional sources, the number that requires a partial reference period estimate from (1873–974) is not as bad as one may anticipate [203]. The combined land and marine datasets [204] were used as partial estimates as necessary. Monthly fields were computed using the weighted difference between the 1971–1990 (20 years) and 1951–1960 (10 years) periods at a grid resolution of 5°. The 1951–1970 CRU station average was supplemented with the necessary monthly adjustment for each station that required an estimate in either of the 5° boxes. Adjustments from nearby boxes were used for some stations when this seemed unfeasible.

In addition to computing monthly reference period values for 1961–1990, monthly standard deviation values for 1941–1990 were calculated for each of the 2961 stations. Erroneous outliers find their way into the station dataset despite all efforts to filter out questionable data, such as data submitted for an incorrect month or data with transcription and submission problems. Values that deviated by more than six standard deviations from the mean were marked. The reference period means and standard deviations were computed without these numbers, and the procedure was repeated. The gridding technique is the same as that of the CRU, except that the location of a station inside the box is not considered. The average of all known station anomalies in the 5° × 5° box constitutes a grid box temperature anomaly. As such, the average temperature anomaly and total number of contributing stations were maintained. The standard deviation variable is used to eliminate misleading outliers between 1941 and 1990.

Furthermore, the few 1851–1940 outliers that deviated more than six standard deviations from the 1961 to 1990 mean were excluded. Outliers have also been identified since 1 January 1991, and attempts have been made to correct the data manually using adjacent stations. If correcting the value is not possible, dubious values could be omitted. In comparison to the original CRU technique, how good are the improvements made to the spatial coverage? For a fundamental comparison (Table 12), the first study pertains to 1873 stations, whereby the new analysis approach was used to determine the percentage area and box count for 5° boxes. World maps are the most effective means of displaying these advancements. The locations of the 779 boxes with data for at least 21 years are shown for each month of the 1961–1990 period [205]. Research by Ibebuchi and Lee [206] demonstrated the progress of the first CRU analysis (99 new boxes that would never have had data before). Five key regions–Mongolia, Australia, South America, sections of the former Soviet Socialist Republics (mostly Russia), and a few boxes in the Middle East–have seen advances. Antarctica is not an improvement since data were incorporated into the Southern Hemisphere average [207] by assuming that the Antarctic $(65^\circ - 90^\circ S)$ temperature anomaly (concerning 1957–1975, as per Karam et al. [208] study) could be weighted by area represented with the Southern Hemisphere anomaly (concerning $1951 - 1970$) for $0^\circ - 60^\circ S$. Finally, Chen et al. [209] presented 143 boxes containing data from 1961 to 1990 and those containing no data from 1991 to 1993. A significant portion of this may be explained by station data that was accessible until the late 1980s but has not been published globally from wealthy nations such as the United States, Canada, Russia, China, Australia, and several Pacific and Atlantic islands. This could be attributed to insufficient reporting from the operational network in some regions of Africa and Southeast Asia. In the North Atlantic and North Pacific, some boxes are filled because of the majority of ocean weather ships shutting down. Although the area was lost by 6% [35–79] in the early 1990s, there are now 252 more stations (i.e., 1226 minus 974) in-service than in the last CRU study. The percentage improvement was larger since, in the 1980s, up to 200 of the 974 stations ceased reporting. The average annual and seasonal temperature data for the Northern and Southern Hemispheres are shown in Studies 4 and 5. These new findings bear striking similarities to CRU's in most respects. This demonstrates the validity of previous conclusions regarding the trajectory of global surface temperature change [210].

The percentage of studies is less than in the previous analysis (CRU), but this is only because the analysis was changed from a 5° × 10° grid to a 5° × 5° box. Currently, a single station can only cover half (one 5° box) of the region of the previous analysis. By doing this, extrapolation of individual stations to vast regions in data-sparse regions is avoided. Current global warming would seem to be lessened in a new combined land–marine dataset because it has been more pronounced on land than on water. The standard deviations of the mean for the Northern Hemisphere were highest in winter and lowest in summer (Table 12). This yearly variability cycle was also observed in the Southern Hemisphere but with minimal amplitude. In contrast to Kuttippurath et al. [212], the standard deviations of the new analysis were somewhat more significant in the Southern Hemisphere, although not consistently.

The correlation coefficients between the hemispheric mean estimates based on the current study and those based on the previous CRU analysis for the period 1901–1990 are also included in Table 13. The most notable aspect of the early 1990s was the sharp cooling in the Northern Hemisphere between 1991 and 1992, especially in the summer and fall of that year and, to a lesser degree, in the same season in 1993. Cooling was less season–dependent in the southern hemisphere. The dust veil brought on by the Mount Pinatubo eruption likely caused the cooling. Dangendorf et al. [190] observed the absence of any cooling for periods with additional catastrophic volcanic eruptions using CRU data for the boreal winter season in the Northern Hemisphere. Koch et al. [211] used data to illustrate the impact of shifting geographical coverage over time as a proportion of the area in each hemisphere. Comparable findings were obtained when these statistics were calculated for the entire period (1851–1992 for the Northern Hemisphere and 1858–1992 for the Southern Hemisphere).

The standard deviations were up to 25% higher, suggesting that the data had greater year–to–year fluctuations. Frozen grid investigations by Zhao et al. [213] demonstrated that the leading cause of this increased variability was a lack of data availability at that time. The correlations shown in

Table 14 for 1901–1990 are comparable, even with the data from the 19th century. However, only a few supplementary data series that were part of the new study contained additional data from the nineteenth century. Therefore, the differences in this period reflect the shift in the impact of the reference period and the modification of the technique used to compute the grid–box values. The correlation values for the Southern Hemisphere showed the greatest discrepancy between the CRU and the new analysis. The increase in grid boxes containing data is higher as a percentage of the original data [214], with increases mostly coming from South America and Australia and with Antarctic data handled appropriately. Most of the rise in the Northern Hemisphere has occurred in Asia's medium–to–high–latitude regions. Table 15 shows the monthly temperature changes after fitting a linear trend to the current data. Upon examining the temperature time series shown in Figures 1(e) and 2(d), it is evident that a linear function significantly oversimplifies and provides a poor fit for the seasonal temperature series [215]. By contrast, the century timeframe trends, as determined by Y. C. Lee et al. [216] using surface data, have errors in order of magnitude less than the typical values (0.5 °C per century, for example). For comparison purposes, only the computational results for the two periods, 1861 minus 1990 and 1901–1990, are shown. Both the conventional methods and the resilient–trend approach described by Lelli et al. [217] were used to calculate the trends. By fitting a straight line between the median values of the first and final third of the time series, the trend was predicted using a full–trend computation. The findings for the Northern Hemisphere match those of earlier investigations [218,219]. However, the findings are only comparable for the Southern Hemisphere period. The changes in the reference period and the few extra stations in Australia throughout the 19th century warmed the 1870s, resulting in trends throughout the 1861–1990 period, which are approximately 0.2 °C lower than previous assessments. Although reanalysis with more than 1088 stations has increased the precision and scope of the accessible grid–box temperatures at specific locations by expanding the number of contributing stations, the impact on hemispheric averages is small. In addition to demonstrating hemispheric mean temperature series resilience, this finding raises the possibility that even better results may have been obtained with fewer stations. It is possible to make this proposal using statistics.

What is the adequate number of independent stations (or degrees of freedom) for the land regions of the planet because of the spatial correlation between the 2961 stations utilised here? This topic is relevant only when calculating large–scale or hemispheric averages. The dataset created here must be as accurate as possible for each grid box to be used for any of the other purposes for which it was created. The only way to achieve this is to use as many stations as possible. Accuracy varied throughout the regions, primarily based on the number of contributing stations in each grid box. Another method for determining the correct number is to use the correlation decay–length theory proposed by Soltani et al. [186]. The distance at which the correlation between two stations decreases to a value of 0.37(l/e), is known as the correlation decay length (l), as calculated by the formula:

$$r = e^{-d/l}$$

Where the distance between the stations is denoted by d and the correlation by r, a station must be closer to its neighbour by less than 520 km to preserve half of the variance (r=0.71), given that l typically has a value of 1500 km at mid-latitudes. In terms of latitude, a resolution of 5° yields a spacing of approximately 550 km. Here, the correlation decay lengths are shorter, even though the spacing decreased in the longitudinal direction, especially at high latitudes. Given that decay durations are shorter in the boreal summer, varying correlation decay lengths would need to be accurately accounted for using a grid box size that changes with season and latitude. Using the correlation decay–length approach, a minimal number of stations may also approximate the hemispheric average of land stations. The correlation decay–length approach and principal components suggest that an adequate number of independent stations in the Northern Hemisphere (NH) would be smaller in winter and more significant in summer, with slight seasonal variation over the Southern Hemisphere.

However, any analysis is only an approximate (SH). Assuming that the Earth’s radius is 6340 km, the number of stations needed to cover the planet at 520 km spacing would be approximately 594 in the example expressed above. This would result in 119 stations in the NH and 59 in the SH, with an estimated land fraction of 40% (NH) and 20% (SH). Weisheimer et al. [220] chose a subset of 2961 stations to test this strategy. The authors made a subjective selection by selecting stations with comparatively long record periods and approximately equal spacing from primarily rural locations. Liao et al. [221] reported the locations of 172 stations (109 in the NH and 63 in the SH). Hemispheric averages were calculated by simply averaging the temperature anomalies of all stations (from 1961 to 1990), with each station weighted according to the cosine of its latitude.

In contrast to the previous reanalysis, the grid boxes are not weighted. In this case, cosine weighting is an effort to account for the higher number of mid– and high–latitude stations compared with tropical stations. In an investigation by Liu et al. [222], the resulting hemispheric average time series was compared with the full analysis performed before (after applying a 10–year Gaussian filter). Table 16 shows the correlation coefficients calculated from the raw and unsmoothed data for the period 1901–1990. The two sets of analyses were mostly similar in the timeframes shown in Northern Hemisphere research by Lockwood et al. [223]. The sequence of the correlations matched that of the two independent studies conducted by Lu et al. [224]. Although differences were often more pronounced in the nineteenth century, in the present era, there were only 43 stations in the

NH and 12 in the SH (the locations of which may be found in research by Maia et al. [225]. The smoothed series in the analysis by Nazarenko et al. [226] deviated more noticeably from those in the north, and the interannual correlations (Table 4) were lower for the SH. Due, in part, to offset distortions in the seasonal data, the yearly curve was adequately reproduced throughout the 1871–1900 period, even with just 12 sites. The general trends in the chosen station set and the entire study period for 1901–1990 showed only minor variations. Based on complete and robust trends ($^{\circ}\mathrm{Cyr}^{-1} \times 10^{2}$) the selected set for annual data warms relative to the full analysis by $0.12^{\circ}\mathrm{C}$ in the NH and cools by $0.08^{\circ}\mathrm{C}$ in the SH.

This assessment suggests that the number of chosen stations should be further reduced along the NH. Inferences about how well the 43 stations performed in the nineteenth century cannot be drawn too extensively since several significant areas were excluded from the comprehensive study during this period. However, since the 1940s, when virtually all 109 sites had data, decadal fluctuations in the NH average series were accurately estimated. The 63 stations performed relatively well for the SH but never as well as for the NH. As a result, the data reduction in the SH was much lower (only 15%, 63 of 421) than in the NH (4.3%, 109 of 2540). This might be partly due to the four different landmasses, as opposed to the two considerably larger landmasses in the NH.

Regarding hemisphere assessments, larger discrepancies between JN and the entire reanalysis occurred over the SH. Furthermore, the differences in the subset selection analysis were more significant than those in SH (Table 17). It is essential to compare the original JN study with a reanalysis of the continents of Australia and South America. By calculating the monthly anomalies of continental temperature from both studies, the grid boxes or grid points in the two areas (South America, $5^{\circ}-55^{\circ}\mathrm{S}$, $30^{\circ}-80^{\circ}\mathrm{W}$; Australia, $10^{\circ}-50^{\circ}\mathrm{S}, 110^{\circ}-160^{\circ}\mathrm{E}$) were effectively weighted. In the research of Y. Li et al. [227], comparisons of the two sets of time series are shown (using 10–year Gaussian–filtered data).

Baseline correction the two reference eras, 1961–1990 and 1951–1970, has not yet been attempted. Table 18 provides the interannual correlation coefficients for 1901–1990. The two assessments for South America agreed well after 1940. But for several seasons in the 19th century, the agreement deteriorated. For South America, the values of the reference period are very similar, with the 1980s being warmer and the 1970s being more laid back than the average of 1951–1970. On the other hand, there is a glaring discrepancy between the reference eras; on average, 1961–1990 was 0.15 °C warmer than 1951–1970. Owing to this discrepancy, the initial analysis was shown to be higher than that of the updated study. The seasonal bias indicates that the difference is largest in summer and lowest in winter. In addition, throughout the 19th century, the bias decreased and even reversed in sign. The long–term warming trends ($^{\circ}\mathrm{Cyr}^{-1} \times 10^{2}$), which were calculated for the years 1901–1990, would be far more significant than the current analysis. Longer research duration would make this even more crucial. Therefore, the Australian sector accounts for a large portion of the difference between the original and updated analyses, as shown in Table 19 for the SH. The conclusions drawn from these two investigations may seem contradictory.

Although approximately 100 sites provide valid estimates of NH average temperatures, estimates for areas at the continental scale have only been accurate since the 1940s when the trend estimates are comparable. Reducing the scale even further to local, regional series, estimated from the average of a few boxes, will likely also result in similar or even more significant issues than the examples presented in the study by Nogueira et al. [228], with the possible exception of regions of North America and Eurasia, where station numbers per grid box are high (>5). When creating a 5° × 5° grid–box dataset, the only conclusion is that the largest dataset for many applications should be created using the greatest number of stations. There is only one purpose for such a study, even if it is feasible to predict hemisphere temperatures from as few as 170 locations reliably. Being certain of the correctness of the subset analysis can only be achieved by examining every currently available station time–series.

5.3. Limitations and Future Perspectives

In meteorology, the use of machine learning techniques to identify atmospheric patterns by analysing vast volumes of historical data is becoming increasingly popular [229]. This method of deriving fundamental physical connections in the atmosphere from data presents an opportunity to investigate novel algorithms that maximise the resultant value based on different verification measures. It is essential to provide a technique for training neural–network precipitation models with a loss function that blends binary or dichotomous [yes, no] measurements with continuous metrics.

The verification of dichotomous events in weather forecasting has been extensively studied [230]. Rainfall, frost, floods, and fog are examples of dichotomous meteorological phenomena. Verifying categorical binary events often begins by creating a contingency table (Table 20) that shows how frequently observed events and predictions of the ‘yes’ and ‘no’ models occur. Thresholds are usually made in weather forecasting to definitively identify whether weather events will occur based on continuous variables that fall or rise over certain thresholds. Contingency tables can be used to calculate several widely used indices, including the false–alarm rate and probability of detection (FAR–POD). These indicators are often used as assessment measures in meteorological research because they allow the measurement of the quality of several elements of dichotomous prediction models. Gradient descent is a widely used and adaptable machine–learning approach that is now used as the standard methodology for training

Artificial Neural Network (ANN) models. Gradient descent specifies an iterative procedure, that until a local or global minimum is attained, computes the derivative of the loss function (model error) and modifies the model parameters in the direction that minimises this loss. Binary indices can be used to assess weather models can be trained using gradient descent. However, because these indices are not differentiable, they cannot be organically incorporated into the optimisation process. Determining the minima of the gradient descent requires smooth differentiable loss functions. Logical comparison operators (<,>) can be used to construct the categorical binary indices. These operators create a function that has a discontinuity at the threshold point and is consequently non–differentiable.

In machine learning, the issue of maximising non–non-differentiable categorical classifiers has previously been studied [231]. The precipitation produced by Numerical Weather Prediction (NWP) is often a quantitative variable in weather forecasting and is confirmed using a range of quantitative and categorical verification criteria. Proposing a technique that integrates both forms of measures and optimises models that achieve good performance with both metrics is essential. This issue may be framed as a Pareto or multi-objective optimisation problem, meaning that no single solution can maximise each goal separately and concurrently. In this study, it is essential to provide an alternative formulation of binary indices that exhibit desirable properties of being both differentiable and continuous.

It is crucial to demonstrate how these indicators may be optimised by integrating them into the loss function of weather models developed using gradient descent. It is important to employ this technique in the experimental part to train a deep learning network that uses NWP geopotential heights as inputs to forecast gridded total precipitation. It is also essential to demonstrate how neural network models using the suggested indices are optimised with respect to skill, using various category binary metrics. This is the first technique that combines quantitative and categorical criteria to optimise meteorological precipitation models. The theoretical foundation of the equivalent differentiable indices is presented in Section 2.2.

Along with a short discussion of the derivation of the traditional categorical binary index. The data, model, and tests used to evaluate the behaviour of the suggested indices are presented in Section 3. Experimental findings showing how flat binary metrics can be used to optimise Artificial Neural Network (ANN) models are presented in Section 2.3. By using hits, misses, false alarms, and true negatives to measure the correlation between actual and expected occurrences, binary predictions can be evaluated. The joint distribution, which consists of four combinations of observations [yes, no] and forecasts [yes, no, yes, no], may be shown using a contingency table (Tables 21 and 22).

There are no misses or false alarms in a perfect prediction contingency table, only hits and correct negatives. Contingency tables are useful tools for displaying precision and errors generated by deterministic models. The indices in this contingency table can be used to compute a variety of commonly used categorical statistics to characterise various aspects of a model's competency. The Probability Of False Detection (POFD) = false alarms/(false alarms + true negatives) and the Probability Of Detection (POD) = hits/(hits + misses), often known as hit rate, are two examples of these statistics that can provide readers with a comprehensive and in-depth treatment of categorical binary indices and weather forecast verification from a wider perspective [232].

Categorical binary measures, such as NWP, are also a common option for assessing the proficiency of quantitative models [233]. Temperature, wind, and precipitation are just a few of the continuous output parameters produced by quantitative NWP models. Setting a threshold value for an event and transforming predicted continuous values into binary representations [yes, no] or, in the case of precipitation, [rain, dry] using the (<,>) relational operators may be used to generate contingency tables. A step function defined by logical relational operators is often represented by the boolean values ‘no’ or ‘false’ and ‘yes’ or ‘true’, with 0 denoting these values. There is a discontinuity or singularity at the threshold value owing to the change from zero to one. Because these functions are not continuous, they cannot be differentiated. Ren et al. [234] suggested the use of smooth and differentiable functions to formulate categorical verification indices differently. In particular, the sigmoid function must represent a smooth transition between the Boolean values at the threshold point. The sigmoid function is defined as follows:

$$\text{sigmoid}\ (x) = \frac{1}{1 + e^{-\beta x}}$$

Y. Qian et al. [235] study proposes a differentiable substitute for the ‘<’ and ‘>’ step functions. Greater values of β indicate a sharper transition in the output, thus determining the slope of the sigmoid function. When a threshold value α is taken into consideration, the sigmoid variable x is translated by this quantity, leading to the following scenario using the ‘>’ operator:

$$\text{sigmoid}\ (x) = \frac{1}{1 + e^{-\beta(x-\alpha)}}$$

These sigmoid functions can be used to generate a differentiable version of the previously given contingency table and approximate the step function. An element-wise product of the vectors holding observations and forecasts compared to the threshold value α is used to construct each item in the contingency table. For instance, ‘Hits’ is calculated using the following expression:

$$\text{Hits } = (\text{ observed } > \alpha) \odot (\text{ predicted } > \alpha)$$

It is possible to make the above formula differentiable by replacing the comparison with a sigmoid function in the 'predicted' term. The gradient provided by this new expression enables the model outputs to be optimised around the threshold. The comparison operators in differentiable categorical statistics, such as POD or POFD, can be substituted for the sigmoid functions. For example, the differentiable forms of POFD and POD are defined as follows:

$$\text{POD}_{\text{diff}} = \frac{\text{Hits}_{\text{diff}}}{\text{Hits}_{\text{diff}} + \text{Misses}_{\text{diff}}}$$

$$\text{POFD}_{\text{diff}} = \frac{\text{False Alarms}_{\text{diff}}}{\text{False Alarms}_{\text{diff}} + \text{True Negatives}_{\text{diff}}}$$

where :

$$\text{Hits}_{\text{diff}} = (\text{observed} > \alpha) \odot \text{sigmoid}(\text{predicted} - \alpha)$$

$$\text{Misses}_{\text{diff}} = (\text{observed} > \alpha) \odot \text{sigmoid}(-\text{predicted} - \alpha)$$

$$\text{False Alarms}$$
$$\text{diff} = (\text{observed} < \alpha) \odot \text{sigmoid}(\text{predicted} - \alpha)$$

$$\text{True Negatives}$$
$$\text{diff} = (\text{observed} < \alpha) \odot \text{sigmoid}(-\text{predicted} - \alpha)$$

The new indices in the differentiable contingency table can be used to construct additional categorical indices. This section presents a concluding synopsis of the model, dataset, and experiments used to evaluate the proposed differentiable categorical binary indices. Selecting a neural network model that has been trained to use the height of the geopotential as an input to compute the total precipitation field is essential. The link between geopotential values and total precipitation grids can be applied to the neural network model. Continuous values represent the precipitation of each cell of the grid, and the models can be trained to reduce the error between the total rainfall recorded by ERA–Interim and the forecast grid. In continuous precipitation fields, the error is often measured using the Root Mean Squared Error (RMSE) metric [236]. The Mean Squared Error (MSE) is a favoured machine–learning metric over the root mean square error (RMSE) because it is less computationally demanding while maintaining similar local and global minima. Six–hour temporal–resolution reanalysis data from 1979 to the present are included in ERA–Interim.

The associated experiments have utilized the European Centre for Medium–Range Weather Forecasts (ECMWF) ERA–Interim global climate reanalysis dataset. The dataset has a geographical resolution of approximately 80 km at 60 vertical levels (reduced Gaussian grid N128). The ECMWF public dataset online portal provides access to the ERA–Interim data. The selection of variables for total precipitation (t_p) and geopotential height (z) is essential for the tests. It is, therefore, necessary to consider a subset of the original data that focuses on the rectangular mid-latitude area, which is the eastern half of the Atlantic Ocean and Europe and is bordered by the coordinates of (latitude: [75,15], longitude = [50, 40]) degrees. The temporal domain data, which have a resolution of six hours, cover 1979–2018. The input is the geopotential height at the pressure levels [1000,900,800,700,600,500, 400,300,200,100] hPa, and its output, or forecast field, is the total amount of precipitation.

The resulting geopotential height data are expressed in dimensions [time, latitude, longitude, and height] as a 4–dimensional numerical array with the form [58440,80,120,10]. Similarly, a three–dimensional numerical array of the form [58440,80,120] representing the [time, latitude, longitude] dimensions was used to describe the total precipitation. For clarity, the 3-hour accumulations used to describe the entire ERA–Interim precipitation parameter must be further aggregated into 6–hour periods to match the 6–hour frequency of the geopotential height field. Saiz–Lopez et al. [237] illustrated the geographical region (bottom left) and the relationship between geopotential height and the field time series of total precipitation (right). While acquiring a compressed data representation, convolutional encoder–decoder networks are a type of neural network that can map between multiple inputs and outputs.

These networks have been used for segmentation, regression, and classification in various disciplines [238]. Similar networks have been used in meteorology to simulate severe weather and atmospheric circulations [239]. One of the proposed models is a 'U–net', which is a convolutional encoder–decoder network. Readers can consult an earlier study [240] to thoroughly compare various encoder–decoder designs to determine precipitation from geopotential fields. Senande–Rivera et al. [241] illustrated how U–net network design alters the dimensionality of the data. This network comprises two symmetric components: an encoder to compress the input data and a decompressor to reconstruct the output space (decoder). The spatial connections in the data at various scales can be captured using chained convolution processes, which can also be used to extract pertinent characteristics that link the input and output regions.

In this case, the total precipitation and geopotential heights (at 10 atmospheric levels) are estimated. The numbers indicate the dimensions of the pictures at each step of the Convolutional Neural Network (CNN) model at the top of this study. Similarly, the channels or features at each network tier are represented by the numbers at the bottom. The network receives ten geopotential levels as input and yields a single picture that shows the precipitation field, thereby expressing how neural network models may function as well as possible using the suggested differentiable categorical indices. It is essential to create an objective function using a mix of these indicators and train a U–net model with geopotential levels as inputs to forecast the ERA–Interim total precipitation. They select the Probability of Detection (POD) and Probability of False Detection (POFD) as the indices for optimisation. Relative Operating Characteristics (ROC) is a widely used graphical technique that is often used to demonstrate the overall competence of categorical weather models. These indices quantify several elements of a model's performance.

The percentage of occurrences of observed 'no' that are mistakenly predicted as 'yes' is measured by POFD. This index ranges from zero to one, with zero indicating a flawless model. POD calculates the percentage of observed 'yes' occurrences that were accurately predicted. Similar to POFD, POD has a range of 0–1; however, unlike POFD, its highest value was 1. Using these two indices, the model performance can be improved by maximising POD and decreasing POFD scores. Because reducing POD results in a model with no skill, POD cannot be employed directly in gradient descent optimisation. POD must be inverted to carry out optimisation correctly; thus, minimisation equates to an increase in the model's competence. It is essential to employ the False Negative Rate (FNR), which is the POD's complementary index and is expressed using the following equation:

$$FNR = 1 - POD = 1 - \frac{\text{hits}}{\text{hits} + \text{misses}} = \frac{\text{misses}}{\text{hits} + \text{misses}}$$

The differentiable forms of FNR and POFD, defined using the equations presented in Section 2.3., were used as loss functions in the experiments. When using the original unscaled precipitation measurements, the sigmoid functions used to construct the differentiable indices in the trials established a fixed value of β=1. The impact of this parameter on the experimental results is discussed in Section 2.4. Finding a balance between two opposing pressures is the outcome of optimising a model that incorporates these two measures, FNR and POFD. While lowering the POFD results in under–predicting models with no precipitation, reducing the FNR produces overconfident models that predict precipitation everywhere. The goal was to use these indices to improve the output of the trained quantitative models and minimise the MSE error. The MSE is often used in the literature to verify precipitation predictions [242]. Following the procedure outlined in Section 2.5., it is essential to suggest a loss function that combines MSE with differentiable versions of FNR and POFD.

$$\min\{MSE + \lambda FNR_{\text{diff}} + \mu POFD_{\text{diff}}\}$$

The constant parameters in this equation, λ and μ, regulate how much weight each category index has overall in the loss function. The model may provide continuous precipitation values within the range of the initial ERA–Interim total precipitation variable owing to the regularisation term MSE. The network could distinguish between various types of rainfall near the designated threshold α if the MSE term were absent. However, it was not possible to consider quantitative variations in the range of precipitation values. It is essential to compare the output of the U–net model in the next section, as it was trained with various values for λ and μ in the loss function. It is essential to use a 70/30 split across the temporal dimension of the ERA interim dataset to conduct the experiments and assess the outcomes (the training split contains years from 1979 to mid–2005 and the validation split from mid–2005 to 2018).

Because each model is trained using identical splits each time, the results can be compared appropriately using performance metrics such as MSE, POD, and POFD. The baseline performance is established by training the U–net network using MSE alone, that is, setting both the λ and μ constants to zero. After experimenting with various combinations of values, it is crucial to assess the impact of these categorical indices on performance by comparing them with the baseline. Using only MSE in the loss function, which is equivalent to λ=0 and μ=0 in the loss function, a baseline for the model comparison can be established. Using the preset ERA–Interim splits, the U–Net model was trained on the entire training dataset for 100 epochs (iterations). Evaluating the performance of the model on the validation split after each training period is crucial. The model's competence is evaluated using MSE, FNR, and POFD, with α=1.0[mm/h] serving as the threshold value for precipitation discrimination. For the reader's understanding, the verification process uses the conventional POD and POFD indices rather than their differentiable equivalents. The loss function, determined during the backpropagation stage of NN (i.e., neural network) model training, uses differentiable indices. It is necessary to train comparable models using other combinations of the λ and μ constants in the loss function, using this model as a reference. Therefore, three possibilities must be considered. In the first two, one of the constants must be fixed to 0, and the other must be used to traverse the values 2,4,8. An identical set of values for both variables is crossed in the third case.

Ultimately, nine models were trained using the resultant combinations of and. Similar to previous work, Shiogama et al. [243] illustrated the development of two of these models after training. It is crucial to note that the POD score for the model trained with λ=2 and μ=0 is much lower than the baseline model, even if this comes at the price of an increase in MSE and POFD, on the right. Similarly, the model trained with λ=0 and μ=2 shows a notable decrease in the POFD score on the left, penalising MSE and POD. The baseline model, which lists the score values for each model, is shown in the first row of Table 23. The corresponding POD, a more widely used score in weather forecasting, has replaced FNR. The correlations between the values of the two constants in the loss function and fluctuation of the scores are listed in this table. Sleeter et al. [244] offered a graphic representation of how these parameters affect the precipitation field that the models learn. It is necessary to sequentially represent the original ERA interim total precipitation field (not used during training), the output of the baseline U–net model, and, in the second row, the three models corresponding to the extremes for each of the scenarios considered using one sample from the validation split, which corresponds to September 16, 2016. Song et al. [245] demonstrated an incredibly conservative model that only forecasts rain in areas with strong signals.

On the other hand, POD has a significant weight in the loss function in the research by Stolzenbach et al. [246], which causes the model to become overconfident and depict precipitation levels higher than the threshold α=1. Looking at the results in Table 24, the third model, which corresponds to λ=8 and μ=8, obtains a substantially superior POD score with a minor sacrifice in POFD and a significant loss in MSE. Although this model apparently measures precipitation with sharper estimates than the reference, it also appears to overestimate precipitation quantities on average, which likely accounts for the increase in MSE. A 3–way tradeoff was established between the scores using the proposed objective function. However, the sensitivity of these scores is not symmetric. For example, Tan et al. [247] showed the progression of the three scores for two situations in which one of the constants is set to 0. Low POD score values resulted in a slight decline in performance according to the MSE and non–weighted variable. Performance was severely hampered when the constant values were greater than 4. The data also revealed an intriguing finding: the POFD of the baseline model was low. Penalisation in the remaining scores may outweigh the relative improvement obtained by weighting POFD with significant μ values. This truth becomes clear when evaluating performance using compound indices such as relative operating characteristics (ROC; [248]). The ROC is a widely used statistic that integrates POD and POFD scores recorded at multiple thresholds in a single graph and is often used to evaluate the precision of categorical weather predictions [249]. The skill of a ROC plot in the range of [0,1] is measured by the area under the curve (AUC; [250]), where 1 is the score of the ideal model. ROC plots and related AUC scores for the baseline model, λ=2 and μ=0 are shown in the research by Tsagouri et al. [251] research using the following threshold values: = 0.5,1,2,5,10. It is crucial to observe how the form of the ROC plot changes as λ and μ increase, moving the points to the left and top of the study, respectively. However, obtaining an ideal AUC score is not achievable owing to the nature of the optimisation problem.

POD is penalised so severely by increasing μ that the resultant AUC values are lower than the baseline model. The ideal combination for the models must be found at [λ=2, μ=0], which produces an AUC score of 0.982 instead of 0.977 for the baseline model. Lower AUC scores resulted from further penalisation of the POFD index by increasing the value of. It would be feasible to create new loss functions that optimise NN models according to the AUC score using the methods described in this paper. The findings in Table 25 were shown as points in a three–dimensional scatter plot by Tsai et al. [252]. Points were projected onto the three orthogonal planes established at the coordinate origin for straightforward interpretation. A Pareto front (depicted as a contour line in Figure 2(d)), is defined by the points in the vertical planes, including the MSE axis. The link between the variables in a multi–objective optimisation issue was studied using Pareto efficiency.

In multi–objective issues, optimality occurs when an improvement in a criterion negatively affects at least one other. Pareto fronts are multidimensional charts that graphically depict the ideal points as lines or surfaces. In this instance, these Pareto fronts represent the trade–offs and connections between POD, PFD, and MSE. It is difficult to optimise both variables simultaneously because their dependence is defined at the front. There is no discernible Pareto link or roughly linear relationship between the two variables on the horizontal plane, represented by the POD and POFD axes. TensorFlow [253] served as the back–end for the models used in this section, which were constructed using Keras [254], a high–level neural network interface written in Python. Some studies (e.g., [256–283]), the geographic correlations between NWP variables, ERA–Interim geopotential height, and learned precipitation were learned using a particular deep learning NN architecture known as the Unet encoder–decoder. A new objective function that combines MSE with the POD and POFD indices must be proposed as the baseline model is optimised to minimise the MSE. The experimental findings show that the performance of the model may be optimised towards a particular index by weighting the individual scores in this objective function. In the definition of the sigmoid function, the parameter β is introduced in Section 2.6. Larger values of β lead to steeper sigmoids and hence to better approximations to the step function.

This parameter regulated the vertical direction of the sigmoid function. It is necessary to note that although it is necessary to anticipate that β would be correlated with the scale of precipitation values and would impact the optimisation outcomes, there were no appreciable variations in the results between higher and lower values of β=1. It is crucial to note that, at this stage, it is still unclear why the combined loss function seems almost invariant to variations in the sigmoid form (or scale of the precipitation values). Scientists must actively investigate this connection, test novel scale–invariant loss functions, and hope that future research addresses these concerns.

Currently, the model and data must be considered when determining the values of constants that weigh various scores in the proposed objective function. Whereas categorical variables represent probabilities confined between [0,1], the regression term (i.e., MSE and MAE) often lacks an upper bound. More research must be conducted to develop new objective functions with normalised constants that are general and invariant to changes in the scaling of input data. Investigating the formulation of high–level goal functions for optimising models with a mix of scores is an intriguing field of enquiry. Weather forecast verification is typically performed using a predetermined set of tests and scores. Model performance would improve if verification suites could design the objective functions.

6. Conclusion

For at least 15 years, research has indicated an upward bias in the climate model warming responses in the tropical troposphere. Instead of being fixed, the issue has worsened, as all climate models in the CMIP6 generation now show an upward bias in the troposphere over the entire planet and in the tropics. Although the warming rates in the models with lower ECS values were substantially closer to the observed rates, they were still strongly skewed upward and did not coincide with the data. Applying the emergent constraint suggests that an ensemble of models with warming rates comparable to observations would probably have ECS values at or below the bottom of the CMIP6 range. Models with higher ECS values also exhibited better tropospheric warming rates. These results are consistent with previous findings from palaeoclimate simulations and the evaluation of equilibrium climate sensitivities, which also point to a systematic warm bias in the most recent generation of climate models. More than 1,000 land-based temperature stations have been incorporated into an enhanced and updated examination of the available data. The findings show that the differences are most significant across the Southern Hemisphere compared to previous research.

Here, the hemisphere was better represented by improvements in data availability than in the north. Additional data, mainly from Australia and South America, were improved. Antarctic data can now be readily included when the reference period changed from 1961 to 1990. The fact that the additional 800+ stations had little effect on the findings confirms the robustness of this and previous analyses of the Northern Hemisphere. Credible hemispheric estimations can be obtained using as few as 109 stations. However, the only way to ensure this is to examine all the information.

Estimation errors increased with decreasing area size up to the continental scale, as predicted. The sharp decline in real-time reporting from stations in many nations in the late 1980s and the early 1990s was the most significant cause for concern. The World Meteorological Organization plans to upgrade the network such that the monthly mean maximum and minimum temperatures can be reported. A historical time series of these variables is needed to use this and put the new data into perspective. This review study is a crucial initial step in this direction.

However, regrettably, there is no intention to increase the number of stations that provide the mean temperature. RCPs provide a distinct collection of data for climate model forecasts, particularly in terms of comprehensiveness, depth, and the geographic scale of information.

The RCPs must be consistent with their selection criteria and provide a rational foundation for the climate–modelling community to investigate the spectrum of climate outcomes. These scenarios cover a variety of radiative forcing routes, which is consistent with recent research. This also applies to the evolution of specific greenhouse gases such as CO_2, CH_4, and N_2O. Compared to previous exercises, each RCP material was much more detailed. Data on air pollution and land use have been made accessible at 0.5° × 0.5° in a geographically clear manner, as well as sectorally detailed for several source categories. A reliable carbon cycle and climate model were applied to the data on greenhouse gas emissions. Additionally, data from the most recent historical period have been reconciled with the RCPs, and harmonisation algorithms have seamlessly transitioned from the historical period to the scenario era. The original underlying IAM scenarios were not distorted by the scaling factors used in this harmonisation. A complex development procedure is required to provide a unified analytical thread that unites the many groups engaged in climate research.

Conflicts of Interest

The author declares that there are no known competing financial interests or personal relationships that could have appeared to influence the work reported in this paper. This work did not receive any specific grant from funding agencies in the public, commercial, or not–for–profit sectors.

Acknowledgements

In the author's lifelong battle against fascist powers, India's veteran journalist Shri. Ashok Wankhede, Shri. Shravan Garg and Shri. Girijesh Vashistha, as well as the country's recently concluded Bharat Jodo Nyay Yatra, had been the inspirations behind the author's rejuvenated vigor in the fight to preserve democracy and socio-economic justice in the nation. The author dedicates this publication to his maternal grandmother, the late Mrs. Jogmaya Paul, who passed away on 2023's holy vedic occasion of Akshay Tritiya.

References

[1] A.T. Archibald et al., "Tropospheric Ozone Assessment Report: A Critical Review of Changes in the Tropospheric Ozone Burden and Budget from 1850 to 2100," *Elementa: Science of the Anthropocene*, vol. 8, no. 1, pp. 1-53, 2020. [CrossRef] [Google Scholar] [Publisher Link]

[2] Mansour Almazroui et al., "Regional and Seasonal Variation of Climate Extremes Over Saudi Arabia: Observed Evidence for the Period 1978-2021," *Arabian Journal of Geosciences*, vol. 15, 2022. [CrossRef] [Google Scholar] [Publisher Link]

[3] Robert Colman, and Brian J. Soden, "Water Vapor and Lapse Rate Feedbacks in the Climate System," *Reviews of Modern Physics*, vol. 93, no. 4, pp. 1-91, 2021. [CrossRef] [Google Scholar] [Publisher Link]

[4] Raghavendra Ashrit et al., "IMDAA Regional Reanalysis: Performance Evaluation during Indian Summer Monsoon Season," *Journal of Geophysical Research: Atmospheres*, vol. 125, no. 2, pp. 1-26, 2020. [CrossRef] [Google Scholar] [Publisher Link]

[5] Saginela Ravindra Babu, "Convective Tropopause Over the Tropics: Climatology, Seasonality, and Inter-Annual Variability Inferred from Long-Term FORMOSAT-3/COSMIC-1 RO Data," *Atmospheric Research*, vol. 298, 2024. [CrossRef] [Google Scholar] [Publisher Link]

[6] Yoonjung Ahn et al., "Verifying Experimental Wet Bulb Globe Temperature Hindcasts Across the United States," *GeoHealth*, vol. 6, no. 4, pp. 1-19, 2022. [CrossRef] [Google Scholar] [Publisher Link]

[7] Alexander J. Baker et al., "Extratropical Transition of Tropical Cyclones in a Multiresolution Ensemble of Atmosphere-Only and Fully Coupled Global Climate Models," *Journal of Climate*, vol. 35, no. 16, pp. 5283-5306, 2022. [CrossRef] [Google Scholar] [Publisher Link]

[8] Karoline Block et al., "Cloud Condensation Nuclei Concentrations Derived from the CAMS Reanalysis," *Earth System Science Data*, vol. 16, no. 1, pp. 443-470, 2024. [CrossRef] [Google Scholar] [Publisher Link]

[9] Ronan Connolly et al., "Challenges in the Detection and Attribution of Northern Hemisphere Surface Temperature Trends Since 1850," *Research in Astronomy and Astrophysics*, vol. 23, no. 10, pp. 1-20, 2023. [CrossRef] [Google Scholar] [Publisher Link]

[10] Stella Bourdin et al., "Intercomparison of Four Algorithms for Detecting Tropical Cyclones Using ERA5," *Geoscientific Model Development*, vol. 15, no. 17, pp. 6759-6786, 2022. [CrossRef] [Google Scholar] [Publisher Link]

[11] Ilann Bourgeois et al., "Comparison of Airborne Measurements of NO, NO_2, HONO, NO_y, and CO during FIREX-AQ," *Atmospheric Measurement Techniques*, vol. 15, no. 16, pp. 4901-4930, 2022. [CrossRef] [Google Scholar] [Publisher Link]

[12] Alugula Boyaj et al., "Role of Radiation and Canopy Model in Predicting Heat Waves Using WRF Over the City of Bhubaneswar, Odisha," *Meteorology and Atmospheric Physics*, vol. 135, 2023. [CrossRef] [Google Scholar] [Publisher Link]

[13] Di Tian et al., "A Hybrid Framework for Forecasting Monthly Reservoir Inflow Based on Machine Learning Techniques with Dynamic Climate Forecasts, Satellite-Based Data, and Climate Phenomenon Information," *Stochastic Environmental Research and Risk Assessment*, vol. 36, pp. 2353-2375, 2022. [CrossRef] [Google Scholar] [Publisher Link]

[14] Deepanshu Aggarwal et al., "Monsoon Precipitation Characteristics and Extreme Precipitation Events Over Northwest India Using Indian High Resolution Regional Reanalysis," *Atmospheric Research*, vol. 267, pp. 1-38, 2022. [CrossRef] [Google Scholar] [Publisher Link]

[15] Akintomide Afolayan Akinsanola et al., "Evaluation of Precipitation across the Contiguous United States, Alaska, and Puerto Rico in Multi-Decadal Convection-Permitting Simulations," *Scientific Reports*, vol. 14, pp. 1-17, 2024. [CrossRef] [Google Scholar] [Publisher Link]

[16] Tanzina Akther et al., "Ozone Precursors and Boundary Layer Meteorology Before and During a Severe Ozone Episode in Mexico City," *Chemosphere*, vol. 318, 2023. [CrossRef] [Google Scholar] [Publisher Link]

[17] Tommaso Alberti et al., "Dynamical Diagnostic of Extreme Events in Venice Lagoon and their Mitigation with the MoSE," *Scientific Reports*, vol. 13, pp. 1-11, 2023. [CrossRef] [Google Scholar] [Publisher Link]

[18] Diego Urdiales-Flores et al., "Drivers of Accelerated Warming in Mediterranean Climate-Type Regions," *Npj Climate and Atmospheric Science*, vol. 6, pp. 1-9, 2023. [CrossRef] [Google Scholar] [Publisher Link]

[19] Robert Vautard et al., "Heat Extremes in Western Europe Increasing Faster Than Simulated Due to Atmospheric Circulation Trends," *Nature Communications*, vol. 14, pp. 1-9, 2023. [CrossRef] [Google Scholar] [Publisher Link]

[20] Daniel J. Vecellio, Constantino M. Lagoa, and David E. Conroy, "Physical Activity Dependence on Relative Temperature and Humidity Characteristics in a Young, Insufficiently Active Population: A Weather Typing Analysis," *Journal of Physical Activity and Health*, vol. 21, no. 4, pp. 357-364, 2024. [CrossRef] [Google Scholar] [Publisher Link]

[21] John G. Virgin et al., "Cloud Feedbacks from CanESM2 to CanESM5.0 and their Influence on Climate Sensitivity," *Geoscientific Model Development*, vol. 14, no. 9, pp. 5355-5372, 2021. [CrossRef] [Google Scholar] [Publisher Link]

[22] Erika Von Schneidemesser et al., "Chemistry and the Linkages between Air Quality and Climate Change," *Chemical Reviews*, vol. 115, no. 10, pp. 3856-3897, 2015. [CrossRef] [Google Scholar] [Publisher Link]

[23] Shuang Wang et al., "Simulation of the Long-Term Variability of the Hadley Circulation in CMIP6 Models," *Atmospheric Research*, vol. 287, 2023. [CrossRef] [Google Scholar] [Publisher Link]

[24] Christopher D. Wells et al., "Significant Human Health Co-Benefits of Mitigating African Emissions," *Atmospheric Chemistry and Physics*, vol. 24, no. 2, pp. 1025-1039, 2024. [CrossRef] [Google Scholar] [Publisher Link]

[25] Wan Wu et al., "Spectral Fingerprinting of Methane from Hyper-Spectral Sounder Measurements Using Machine Learning and Radiative Kernel-Based Inversion," *Remote Sensing*, vol. 16, no. 3, pp. 1-19, 2024. [CrossRef] [Google Scholar] [Publisher Link]

[26] Kanak Lata Xalxo et al., "Performance Assessment of WRF Model Radiation Schemes in Simulating the Track and Intensity of the Super Cyclonic Storm "Amphan"," *Nat Hazards*, vol. 114, pp. 1741-1762, 2022. [CrossRef] [Google Scholar] [Publisher Link]

[27] Xinru Xie et al., "Changes in ENSO-Driven Hadley Circulation Variability under Global Warming," *Atmospheric Research*, vol. 274, 2022. [CrossRef] [Google Scholar] [Publisher Link]

[28] Weiwei Xu et al., "A New Algorithm for Himawari-8 Aerosol Optical Depth Retrieval by Integrating Regional $PM_{2.5}$ Concentrations," *IEEE Transactions on Geoscience and Remote Sensing*, vol. 60, pp. 1-11, 2022. [CrossRef] [Google Scholar] [Publisher Link]

[29] Laura Hyesung Yang et al., "Tropospheric NO_2 Vertical Profiles Over South Korea and their Relation to Oxidant Chemistry: Implications for Geostationary Satellite Retrievals and the Observation of NO_2 Diurnal Variation from Space," *Atmospheric Chemistry and Physics*, vol. 23, no. 4, pp. 2465-2481, 2023. [CrossRef] [Google Scholar] [Publisher Link]

[30] Hao Ye et al., "Lake Ice Thickness Retrieval Method with ICESat-2-Assisted CyroSat-2 Echo Peak Selection," *Remote Sensing*, vol. 16, no. 3, pp. 1-17, 2024. [CrossRef] [Google Scholar] [Publisher Link]

[31] Jong-Min Yeom et al., "Estimation of the Hourly Aerosol Optical Depth from GOCI Geostationary Satellite Data: Deep Neural Network, Machine Learning, and Physical Models," *IEEE Transactions on Geoscience and Remote Sensing*, vol. 60, pp. 1-12, 2022. [CrossRef] [Google Scholar] [Publisher Link]

[32] Mingxin Yu et al., "Interdecadal Shift of the El Niño's Modulation on the Connection between the Hadley Circulation and Tropical SST," *Climate Dynamics*, vol. 60, pp. 2167-2181, 2023. [CrossRef] [Google Scholar] [Publisher Link]

[33] Jianye Yuan et al., "Research on Lightweight Disaster Classification Based on High-Resolution Remote Sensing Images," *Remote Sensing*, vol. 14, no. 11, pp. 1-17, 2022. [CrossRef] [Google Scholar] [Publisher Link]

[34] Colin M. Zarzycki, "Sowing Storms: How Model Timestep Can Control Tropical Cyclone Frequency in a GCM," *Journal of Advances in Modeling Earth Systems*, vol. 14, no. 3, pp. 1-21, 2022. [CrossRef] [Google Scholar] [Publisher Link]

[35] Mark D. Zelinka et al., "Evaluating Climate Models' Cloud Feedbacks Against Expert Judgment," *Journal of Geophysical Research: Atmospheres*, vol. 127, no. 2, pp. 1-18, 2022. [CrossRef] [Google Scholar] [Publisher Link]

[36] Tianhao Zhang et al., "A Geometry-Discrete Minimum Reflectance Aerosol Retrieval Algorithm (GeoMRA) for Geostationary Meteorological Satellite Over Heterogeneous Surfaces," *IEEE Transactions on Geoscience and Remote Sensing*, vol. 60, pp. 1-14, 2022. [CrossRef] [Google Scholar] [Publisher Link]

[37] Xiaqiong Zhou et al., "The Development of the NCEP Global Ensemble Forecast System Version 12," *Weather and Forecasting*, vol. 37, no. 6, pp. 1069-1084, 2022. [CrossRef] [Google Scholar] [Publisher Link]

[38] Jiang Zhu et al., "LGM Paleoclimate Constraints Inform Cloud Parameterizations and Equilibrium Climate Sensitivity in CESM2," *Journal of Advances in Modeling Earth Systems*, vol. 14, no. 4, pp. 1-18, 2022. [CrossRef] [Google Scholar] [Publisher Link]

[39] George Zittis et al., "Maritime Transport and Regional Climate Change Impacts in Large EU Islands and Archipelagos," *Euro-Mediterranean Journal for Environmental Integration*, vol. 8, pp. 441-454, 2023. [CrossRef] [Google Scholar] [Publisher Link]

[40] Cristian Felipe Zuluaga et al., "The Climate Change Perspective of Photovoltaic Power Potential in Brazil," *Renewable Energy*, vol. 193, pp. 1019-1031, 2022. [CrossRef] [Google Scholar] [Publisher Link]

[41] Juseon Bak et al., "An Improved OMI Ozone Profile Research Product Version 2.0 with Collection 4 L1b Data and Algorithm Updates," *Atmospheric Measurement Techniques*, vol. 17, no. 7, pp. 1891-1911, 2024. [CrossRef] [Google Scholar] [Publisher Link]

[42] Andrea Baraldi et al., "Innovative Analysis Ready Data (ARD) Product and Process Requirements, Software System Design, Algorithms and Implementation at the Midstream as Necessary-But-Not-Sufficient Precondition of the Downstream in a New Notion of Space Economy 4.0 - Part 1: Problem Background in Artificial General Intelligence (AGI)," *Big Earth Data*, vol. 7, no. 3, pp. 455-693, 2022. [CrossRef] [Google Scholar] [Publisher Link]

[43] Jasia Bashir, and Shakil Ahmad Romshoo, "Bias-Corrected Climate Change Projections over the Upper Indus Basin Using a Multi-Model Ensemble," *Environmental Science and Pollution Research*, vol. 30, pp. 64517-64535, 2023. [CrossRef] [Google Scholar] [Publisher Link]

[44] Hylke E. Beck et al., "High-Resolution (1 km) Köppen-Geiger Maps for 1901-2099 Based on Constrained CMIP6 Projections," *Scientific Data*, vol. 10, pp. 1-16, 2023. [CrossRef] [Google Scholar] [Publisher Link]

[45] G.H. Bernhard et al., "Stratospheric Ozone, UV Radiation, and Climate Interactions," *Photochemical & Photobiological Sciences*, vol. 22, pp. 937-989, 2023. [CrossRef] [Google Scholar] [Publisher Link]

[46] Muhammad Tousif Bhatti, Arif A. Anwar, and Kashif Hussain, "Characterization and Outlook of Climatic Hazards in an Agricultural Area of Pakistan," *Scientific Reports*, vol. 13, pp. 1-17, 2023. [CrossRef] [Google Scholar] [Publisher Link]

[47] Russell Blackport, and John C. Fyfe, "Climate Models Fail to Capture Strengthening Wintertime North Atlantic Jet and Impacts on Europe," *Science Advances*, vol. 8, no. 45, pp. 1-10, 2022. [CrossRef] [Google Scholar] [Publisher Link]

[48] Sara M. Blichner et al., "Process-Evaluation of Forest Aerosol-Cloud-Climate Feedback Shows Clear Evidence from Observations and Large Uncertainty in Models," *Nature Communications*, vol. 15, pp. 1-12, 2024. [CrossRef] [Google Scholar] [Publisher Link]

[49] Josep Bonsoms et al., "Impact of Climate Change on Snowpack Dynamics in Coastal Central-Western Greenland," *Science of the Total Environment*, vol. 913, pp. 1-13, 2023. [CrossRef] [Google Scholar] [Publisher Link]

[50] Steven J. Brey et al., "Past Variance and Future Projections of the Environmental Conditions Driving Western U.S. Summertime Wildfire Burn Area," *Earth's Future*, vol. 9, no. 2, pp. 1-14, 2021. [CrossRef] [Google Scholar] [Publisher Link]

[51] E. Bruley et al., "Enhanced Spring Warming in a Mediterranean Mountain by Atmospheric Circulation," *Scientific Reports*, vol. 12, pp. 1-12, 2022. [CrossRef] [Google Scholar] [Publisher Link]

[52] Michael P. Byrne et al., "Response of the Intertropical Convergence Zone to Climate Change: Location, Width, and Strength," *Current Climate Change Reports*, vol. 4, pp. 355-370, 2018. [CrossRef] [Google Scholar] [Publisher Link]

[53] Xiaoyan Cao et al., "Spatial-Temporal Variation in XCH_4 during 2009-2021 and its Driving Factors across the Land of the Northern Hemisphere," *Atmospheric Research*, vol. 291, 2023. [CrossRef] [Google Scholar] [Publisher Link]

[54] Anny Cazenave, and Lorena Moreira, "Contemporary Sea-Level Changes from Global to Local Scales: A Review," *Proceedings of the Royal Society A*, vol. 478, no. 2261, pp. 1-30, 2022. [CrossRef] [Google Scholar] [Publisher Link]

[55] Sara Cerasoli, Jun Yin, and Amilcare Porporato, "Cloud Cooling Effects of Afforestation and Reforestation at Midlatitudes," *Proceedings of the National Academy of Sciences*, vol. 118, no. 33, pp. 1-7, 2021. [CrossRef] [Google Scholar] [Publisher Link]

[56] Heeje Cho, Jong-Seong Kug, and Sang-Yoon Jun, "Influence of the Recent Winter Arctic Sea Ice Loss in Short-Term Simulations of a Regional Atmospheric Model," *Scientific Reports*, vol. 12, pp. 1-8, 2022. [CrossRef] [Google Scholar] [Publisher Link]

[57] Kyle R. Clem et al., "Central Tropical Pacific Convection Drives Extreme High Temperatures and Surface Melt on the Larsen C Ice Shelf, Antarctic Peninsula," *Nature Communications*, vol. 13, pp. 1-13, 2022. [CrossRef] [Google Scholar] [Publisher Link]

[58] Jongyun Byun et al., "Deep Learning-Based Rainfall Prediction Using Cloud Image Analysis," *IEEE Transactions on Geoscience and Remote Sensing*, vol. 61, pp. 1-11, 2023. [CrossRef] [Google Scholar] [Publisher Link]

[59] D. Coumou et al., "The Influence of Arctic Amplification on Mid-Latitude Summer Circulation," *Nature Communications*, vol. 9, pp. 1-12, 2018. [CrossRef] [Google Scholar] [Publisher Link]

[60] Lilly Damany-Pearce et al., "Australian Wildfires Cause the Largest Stratospheric Warming Since Pinatubo and Extends the Lifetime of the Antarctic Ozone Hole," *Scientific Reports*, vol. 12, pp. 1-15, 2022. [CrossRef] [Google Scholar] [Publisher Link]

[61] Oliver Branch et al., "Scaling Artificial Heat Islands to Enhance Precipitation in the United Arab Emirates," *Earth System Dynamics*, vol. 15, no. 1, pp. 109-129, 2024. [CrossRef] [Google Scholar] [Publisher Link]

[62] Hien X. Bui et al., "Responses of the Madden–Julian Oscillation to Global Warming: Impacts from Tropical Sea Surface Temperature Changes," *Journal of Climate*, vol. 37, no. 2, pp. 605-617, 2024. [CrossRef] [Google Scholar] [Publisher Link]

[63] Nanda Kishore Reddy Busireddy et al., "Modelled Impact of Ocean Warming on Tropical Cyclone Size and Destructiveness Over the Bay of Bengal: A Case Study on FANI Cyclone," *Atmospheric Research*, vol. 279, 2022. [CrossRef] [Google Scholar] [Publisher Link]

[64] Camille Cadiou et al., "Challenges in Attributing the 2022 Australian Rain Bomb to Climate Change," *Asia-Pacific Journal of Atmospheric Sciences*, vol. 59, pp. 83-94, 2023. [CrossRef] [Google Scholar] [Publisher Link]

[65] Suzana J. Camargo et al., "Characteristics of Model Tropical Cyclone Climatology and the Large-Scale Environment," *Journal of Climate*, vol. 33, no. 11, pp. 4463-4487, 2020. [CrossRef] [Google Scholar] [Publisher Link]

[66] Mengdan Cao et al., "A Two-Stage Machine Learning Algorithm for Retrieving Multiple Aerosol Properties Over Land: Development and Validation," *IEEE Transactions on Geoscience and Remote Sensing*, vol. 61, pp. 1-17, 2023. [CrossRef] [Google Scholar] [Publisher Link]

[67] Brian J. Carroll et al., "Measuring Coupled Fire-Atmosphere Dynamics: The California Fire Dynamics Experiment (CalFiDE)," *Bulletin of the American Meteorological Society*, vol. 105, no. 3, pp. E690-E708, 2024. [CrossRef] [Google Scholar] [Publisher Link]

[68] Paulo Ceppi et al., "Cloud Feedback Mechanisms and their Representation in Global Climate Models," *Wiley Interdisciplinary Reviews: Climate Change*, vol. 8, no. 4, 2017. [CrossRef] [Google Scholar] [Publisher Link]

[69] Jackson Hian-Wui Chang et al., "Biomass Burning in Critical Fire Region Over the Maritime Continent from 2012 to 2021: A Review of the Meteorological Influence and Cloud-Aerosol-Radiation Interactions," *Atmospheric Environment*, vol. 320, 2024. [CrossRef] [Google Scholar] [Publisher Link]

[70] Jianbo Cheng et al., "On the Discrepancies in the Changes in the Annual Mean Hadley Circulation among Different Regions and Between CMIP5 Models and Reanalyses," *Theoretical and Applied Climatology*, vol. 141, pp. 1475-1491, 2020. [CrossRef] [Google Scholar] [Publisher Link]

[71] Chaowei Xu et al., "Comprehensive Analysis for Long-Term Hydrological Simulation by Deep Learning Techniques and Remote Sensing," *Frontiers in Earth Science*, vol. 10, pp. 1-16, 2022. [CrossRef] [Google Scholar] [Publisher Link]

[72] Josep Cos et al., "The Mediterranean Climate Change Hotspot in the CMIP5 and CMIP6 Projections," *Earth System Dynamics*, vol. 13, no. 1, pp. 321-340, 2022. [CrossRef] [Google Scholar] [Publisher Link]

[73] Tyler Cox et al., "Trends in Atmospheric Heat Transport Since 1980," *Journal of Climate*, vol. 37, no. 5, pp. 1539-1550, 2024. [CrossRef] [Google Scholar] [Publisher Link]

[74] Alessandro Damiani et al., "Air Quality and Urban Climate Improvements in the World's Most Populated Region during the COVID-19 Pandemic," *Environmental Research Letters*, vol. 19, no. 3, pp. 1-12, 2024. [CrossRef] [Google Scholar] [Publisher Link]

[75] S. De Cannière et al., "Water Availability and Atmospheric Dryness Controls on Spaceborne Sun-Induced Chlorophyll Fluorescence Yield," *Remote Sensing of Environment*, vol. 301, 2024. [CrossRef] [Google Scholar] [Publisher Link]

[76] Fernando Rafael de Moura et al., "In the Line of Fire: Analyzing Burning Impacts on Air Pollution and Air Quality in an Amazonian City, Brazil," *Atmospheric Pollution Research*, vol. 15, no. 4, 2024. [CrossRef] [Google Scholar] [Publisher Link]

[77] Surat Dewan, and Anita Lakhani, “Tropospheric Ozone and its Natural Precursors Impacted by Climatic Changes in Emission and Dynamics,” *Frontiers in Environmental Science*, vol. 10, pp. 1-21, 2022. [CrossRef] [Google Scholar] [Publisher Link]

[78] Tom Dror et al., “Uncovering the Large-Scale Meteorology that Drives Continental, Shallow, Green Cumulus through Supervised Classification,” *Geophysical Research Letters*, vol. 49, no. 8, pp. 1-8, 2022. [CrossRef] [Google Scholar] [Publisher Link]

[79] William Dulac et al., “Assessing the Representation of Tropical Cyclones in ERA5 with the CNRM Tracker,” *Climate Dynamics*, vol. 62, pp. 223-238, 2024. [CrossRef] [Google Scholar] [Publisher Link]

[80] Sean W. Fleming et al., “SNOTEL, the Soil Climate Analysis Network, and Water Supply Forecasting at the Natural Resources Conservation Service: Past, Present, and Future,” *Journal of the American Water Resources Association*, vol. 59, no. 4, pp. 585-599, 2023. [CrossRef] [Google Scholar] [Publisher Link]

[81] Fouzia Fahrin et al., “The Relationship between Convectively Coupled Waves and the East Pacific ITCZ,” *Journal of Climate*, vol. 37, no. 8, pp. 2565-2583, 2024. [CrossRef] [Google Scholar] [Publisher Link]

[82] Davide Faranda et al., “A Climate-Change Attribution Retrospective of Some Impactful Weather Extremes of 2021,” *Weather and Climate Dynamics*, vol. 3, no. 4, pp. 1311-1340, 2022. [CrossRef] [Google Scholar] [Publisher Link]

[83] J.T. Fasullo et al., “Spurious Late Historical-Era Warming in CESM2 Driven by Prescribed Biomass Burning Emissions,” *Geophysical Research Letters*, vol. 49, no. 2, pp. 1-11, 2022. [CrossRef] [Google Scholar] [Publisher Link]

[84] Juan Feng et al., “Asymmetric Impacts of El Niño Development and Decay Stages on the Hadley Circulation,” *Geophysical Research Letters*, vol. 50, no. 11, pp. 1-9, 2023. [CrossRef] [Google Scholar] [Publisher Link]

[85] Artem G. Feofilov et al., “Incorporating EarthCARE Observations into a Multi-Lidar Cloud Climate Record: The ATLID (Atmospheric Lidar) Cloud Climate Product,” *Atmospheric Measurement Techniques*, vol. 16, no. 13, pp. 3363-3390, 2023. [CrossRef] [Google Scholar] [Publisher Link]

[86] Arlene M. Fiore, Vaishali Naik, and Eric M. Leibensperger, “Air Quality and Climate Connections,” *Journal of the Air & Waste Management Association*, vol. 65, no. 6, pp. 645-685, 2015. [CrossRef] [Google Scholar] [Publisher Link]

[87] Ricardo Fonseca, and Diana Francis, “Satellite Derived Trends and Variability of CO_2 Concentrations in the Middle East during 2014-2023,” *Frontiers in Environmental Science*, vol. 11, pp. 1-20, 2024. [CrossRef] [Google Scholar] [Publisher Link]

[88] Dimitra Founda et al., “The Extreme Heat Wave of Summer 2021 in Athens (Greece): Cumulative Heat and Exposure to Heat Stress,” *Sustainability*, vol. 14, no. 13, pp. 1-16, 2022. [CrossRef] [Google Scholar] [Publisher Link]

[89] Elissavet Galanaki et al., “Spatio-Temporal Analysis of Heatwaves Characteristics in Greece from 1950 to 2020,” *Climate*, vol. 11, no. 1, pp. 1-23, 2022. [CrossRef] [Google Scholar] [Publisher Link]

[90] Jinming Ge et al., “Contrasting Characteristics of Continental and Oceanic Deep Convective Systems at Different Life Stages from CloudSat Observations,” *Atmospheric Research*, vol. 298, 2024. [CrossRef] [Google Scholar] [Publisher Link]

[91] Melissa Gervais, Lantao Suna, and Clara Deser, “Impacts of Projected Arctic Sea Ice Loss on Daily Weather Patterns Over North America,” *Journal of Climate*, vol. 37, no. 3, pp. 1065-1085, 2024. [CrossRef] [Google Scholar] [Publisher Link]

[92] Homa Ghasemifard et al., “Do Changing Circulation Types Raise the Frequency of Summertime Thunderstorms and Large Hail in Europe?,” *Environmental Research: Climate*, vol. 3, no. 1, pp. 1-14, 2024. [CrossRef] [Google Scholar] [Publisher Link]

[93] Theodore M. Giannaros et al., “Meteorological Analysis of the 2021 Extreme Wildfires in Greece: Lessons Learned and Implications for Early Warning of the Potential for Pyroconvection,” *Atmosphere*, vol. 13, no. 3, pp. 1-13, 2022. [CrossRef] [Google Scholar] [Publisher Link]

[94] Sujung Go et al., “Ground-Based Retrievals of Aerosol Column Absorption in the UV Spectral Region and their Implications for GEMS Measurements,” *Remote Sensing of Environment*, vol. 245, pp. 1-55, 2020. [CrossRef] [Google Scholar] [Publisher Link]

[95] Daniel L. Goldberg et al., “TROPOMI NO_2 in the United States: A Detailed Look at the Annual Averages, Weekly Cycles, Effects of Temperature, and Correlation with Surface NO_2 Concentrations,” *Earth’s Future*, vol. 9, no. 4, pp. 1-16, 2021. [CrossRef] [Google Scholar] [Publisher Link]

[96] I.E. Gordon et al., “The HITRAN2020 Molecular Spectroscopic Database,” *Journal of Quantitative Spectroscopy and Radiative Transfer*, vol. 277, pp. 1-82, 2022. [CrossRef] [Google Scholar] [Publisher Link]

[97] Hong Guan et al., “GEFSv12 Reforecast Dataset for Supporting Subseasonal and Hydrometeorological Applications,” *Monthly Weather Review*, vol. 150, no. 3, pp. 647-665, 2022. [CrossRef] [Google Scholar] [Publisher Link]

[98] Mohammad Ganjirad, and Hossein Bagheri, “Google Earth Engine-Based Mapping of Land Use and Land Cover for Weather Forecast Models Using Landsat 8 Imagery,” *Ecological Informatics*, vol. 80, pp. 1-28, 2024. [CrossRef] [Google Scholar] [Publisher Link]

[99] Shu Gui et al., “Association of the Cloud Radiative Effect with the Changes in the Northern Edge of Hadley Circulation between the CMIP5 and CMIP6 Models in Boreal Summer,” *Theoretical and Applied Climatology*, vol. 155, pp. 1247-1259, 2024. [CrossRef] [Google Scholar] [Publisher Link]

[100] Aman Guptaet al., “Estimates of Southern Hemispheric Gravity Wave Momentum Fluxes across Observations, Reanalyses, and Kilometer-Scale Numerical Weather Prediction Model,” *Journal of the Atmospheric Sciences*, vol. 81, no. 3, pp. 583-604, 2024. [CrossRef] [Google Scholar] [Publisher Link]

[101] Panos Hadjinicolaou et al., “Urbanisation and Geographical Signatures in Observed Air Temperature Station Trends Over the Mediterranean and the Middle East–North Africa,” *Earth Systems and Environment*, vol. 7, pp. 649-659, 2023. [CrossRef] [Google Scholar] [Publisher Link]

[102] J. Antonio Guzmán Q. et al., “Multi-Decadal Trends of Low-Clouds at the Tropical Montane Cloud Forests,” *Ecological Indicators*, vol. 158, pp. 1-9, 2024. [CrossRef] [Google Scholar] [Publisher Link]

[103] Thomas M. Hamill et al., “The Reanalysis for the Global Ensemble Forecast System, Version 12,” *Monthly Weather Review*, vol. 150, no. 1, pp. 59-79, 2022. [CrossRef] [Google Scholar] [Publisher Link]

[104] Zhihui Han et al., “Evaluation on the Applicability of ERA5 Reanalysis Dataset to Tropical Cyclones Affecting Shanghai,” *Frontiers of Earth Science*, vol. 16, pp. 1025-1039, 2022. [CrossRef] [Google Scholar] [Publisher Link]

[105] Vittal Hari et al., “On the Role of the Atlantic Meridional Mode in Eastern European Temperature Variability,” *Atmospheric Research*, vol. 297, pp. 1-10, 2024. [CrossRef] [Google Scholar] [Publisher Link]

[106] Zeke Hausfather et al., “Climate Simulations: Recognize the ‘Hot Model’ Problem,” *Nature*, vol. 605, pp. 26-29, 2022. [CrossRef] [Google Scholar] [Publisher Link]

[107] Shuyang Xie et al., “Ambient Atmospheric Application and Influencing Factors of Ozone Catalytic Decomposition Materials in a Channel Test,” *Atmospheric Environment*, vol. 321, 2024. [CrossRef] [Google Scholar] [Publisher Link]

[108] Assaf Hochman et al., “Extreme Weather and Societal Impacts in the Eastern Mediterranean,” *Earth System Dynamics*, vol. 13, no. 2, pp. 749-777, 2022. [CrossRef] [Google Scholar] [Publisher Link]

[109] Erik Höjgård-Olsen, Hélène Chepfer, and Hélène Brogniez, “Satellite Observed Sensitivity of Tropical Clouds and Moisture to Sea Surface Temperature on Various Time and Space Scales: 1. Focus on High Level Cloud Situations Over Ocean,” *Journal of Geophysical Research: Atmospheres*, vol. 127, no. 6, pp. 1-21, 2022. [CrossRef] [Google Scholar] [Publisher Link]

[110] Farnaz E. Hosseinpour, and Eric M. Wilcox, “A New Look into the Impacts of Dust Radiative Forcing on the Energetics of Tropical Easterly Waves,” *Atmospheric Chemistry and Physics*, vol. 24, no. 1, pp. 707-724, 2024. [CrossRef] [Google Scholar] [Publisher Link]

[111] Dubin Huan et al., “Modeled Variations of Tropical Cyclone Genesis Potential during Marine Isotope Stage 3,” *Quaternary Science Reviews*, vol. 326, 2024. [CrossRef] [Google Scholar] [Publisher Link]

[112] Wenshuo Huang et al., “Recent Opposite Trends of Atmospheric Rivers Over East Asia and Western North Pacific Driven by the Pacific Decadal Oscillation,” *Journal of Geophysical Research: Atmospheres*, vol. 129, no. 1, 2024. [CrossRef] [Google Scholar] [Publisher Link]

[113] Ahmad Iqbal et al., “Retrieval of NO_2 Columns by Exploiting MAX-DOAS Observations and Comparison with OMI and TROPOMI Data during the Time Period of 2015-2019,” *Aerosol and Air Quality Research*, vol. 22, no. 6, pp. 1-20, 2022. [CrossRef] [Google Scholar] [Publisher Link]

[114] Xianan Jiang et al., “Muted Extratropical Low Cloud Seasonal Cycle is Closely Linked to Underestimated Climate Sensitivity in Models,” *Nature Communications*, vol. 14, pp. 1-11, 2023. [CrossRef] [Google Scholar] [Publisher Link]

[115] Najmeh Kaffashzadeh, and Abbas-Ali Aliakbari Bidokhti, “Assessment of Surface Ozone Products from Downscaled CAMS Reanalysis and CAMS Daily Forecast Using Urban Air Quality Monitoring Stations in Iran,” *Geoscientific Model Development*, vol. 17, no. 10, pp. 4155-4179, 2024. [CrossRef] [Google Scholar] [Publisher Link]

[116] Peter Kalmus et al., “A High-Resolution Planetary Boundary Layer Height Seasonal Climatology from GNSS Radio Occultations,” *Remote Sensing of Environment*, vol. 276, pp. 1-9, 2022. [CrossRef] [Google Scholar] [Publisher Link]

[117] Yoojin Kang et al., “Improved Retrievals of Aerosol Optical Depth and Fine Mode Fraction from GOCI Geostationary Satellite Data Using Machine Learning Over East Asia,” *ISPRS Journal of Photogrammetry and Remote Sensing*, vol. 183, pp. 253-268, 2022. [CrossRef] [Google Scholar] [Publisher Link]

[118] Dimitris Karagkiozidis et al., “Assessment of the NO_2 Spatio-Temporal Variability over Thessaloniki, Greece, Using MAX-DOAS Measurements and Comparison with S5P/TROPOMI Observations,” *Applied Sciences*, vol. 13, no. 4, pp. 1-23, 2023. [CrossRef] [Google Scholar] [Publisher Link]

[119] D.G. Kaskaoutis et al., “Aerosol Characteristics and Types in the Marine Environments Surrounding the East Mediterranean - Middle East (EMME) Region during the AQABA Campaign,” *Atmospheric Environment*, vol. 298, pp. 1-16, 2023. [CrossRef] [Google Scholar] [Publisher Link]

[120] Hanjun Kim et al., “Subtropical Clouds Key to Southern Ocean Teleconnections to the Tropical Pacific,” *Proceedings of the National Academy of Sciences*, vol. 119, no. 34, pp. 1-8, 2022. [CrossRef] [Google Scholar] [Publisher Link]

[121] Reto Knutti, Maria A.A. Rugenstein, and Gabriele C. Hegerl, “Beyond Equilibrium Climate Sensitivity,” *Nature Geoscience*, vol. 10, pp. 727-736, 2017. [CrossRef] [Google Scholar] [Publisher Link]

[122] Hui-Wen Lai, Deliang Chen, and Hans W. Chen, “Precipitation Variability Related to Atmospheric Circulation Patterns Over the Tibetan Plateau,” *International Journal of Climatology*, vol. 44, no. 1, pp. 91-107, 2024. [CrossRef] [Google Scholar] [Publisher Link]

[123] Hsiang-He Lee, Qi Tang, and Michael Prather, “E3SM Chemistry Diagnostics Package (ChemDyg) Version 0.1.4,” *Geoscientific Model Development*, pp. 1-46, 2024. [CrossRef] [Google Scholar] [Publisher Link]

[124] Pieternel F. Levelt et al., “The Ozone Monitoring Instrument: Overview of 14 Years in Space,” *Atmospheric Chemistry and Physics*, vol. 18, no. 8, pp. 5699-5745, 2018. [CrossRef] [Google Scholar] [Publisher Link]

[125] Davide Faranda et al., “Attributing Venice Acqua Alta Events to a Changing Climate and Evaluating the Efficacy of MoSE Adaptation Strategy,” *Npj Climate and Atmospheric Science*, vol. 6, pp. 1-8, 2023. [CrossRef] [Google Scholar] [Publisher Link]

[126] Ondřej Lhotka, and Jan Kyselý, “The 2021 European Heat Wave in the Context of Past Major Heat Waves,” *Earth and Space Science*, vol. 9, no. 11, pp. 1-12, 2022. [CrossRef] [Google Scholar] [Publisher Link]

[127] Qiyun Ma, Yumeng Chen, and Monica Ionita, “European Summer Wet-Bulb Temperature: Spatiotemporal Variations and Potential Drivers,” *Journal of Climate*, vol. 37, no. 6, pp. 2059-2080, 2024. [CrossRef] [Google Scholar] [Publisher Link]

[128] P. Malakar et al., “Comparison of Reanalysis Data Sets to Comprehend the Evolution of Tropical Cyclones Over North Indian Ocean,” *Earth and Space Science*, vol. 7, no. 2, pp. 1-15, 2020. [CrossRef] [Google Scholar] [Publisher Link]

[129] Liudmyla Malytska et al., “Assessment of Environmental Consequences of Hostilities: Tropospheric NO_2 Vertical Column Amounts in the Atmosphere Over Ukraine in 2019-2022,” *Atmospheric Environment*, vol. 318, pp. 1-13, 2024. [CrossRef] [Google Scholar] [Publisher Link]

[130] Anna Martin et al., “Evaluation of the Coupling of EMACv2.55 and the Land Surface and Vegetation Model JSBACHv4,” *EGUsphere*, pp. 1-40, 2024. [CrossRef] [Google Scholar] [Publisher Link]

[131] Akriti Masoom et al., “Investigation of the Effects of the Greek Extreme Wildfires of August 2021 on Air Quality and Spectral Solar Irradiance,” *Atmospheric Chemistry and Physics*, vol. 23, no. 14, pp. 8487-8514, 2023. [CrossRef] [Google Scholar] [Publisher Link]

[132] Mohammad Mortezazadeh et al., “Sweep Interpolation: A Cost-Effective Semi-Lagrangian Scheme in the Global Environmental Multiscale Model,” *Geoscientific Model Development*, vol. 17, no. 1, pp. 335-346, 2024. [CrossRef] [Google Scholar] [Publisher Link]

[133] Kaighin A. McColl, and Lois I. Tang, “An Analytic Theory of Near-Surface Relative Humidity over Land,” *Journal of Climate*, vol. 37, no. 4, pp. 1213-1230, 2024. [CrossRef] [Google Scholar] [Publisher Link]

[134] Daniel T. McCoy et al., “Extratropical Shortwave Cloud Feedbacks in the Context of the Global Circulation and Hydrological Cycle,” *Geophysical Research Letters*, vol. 49, no. 8, pp. 1-11, 2022. [CrossRef] [Google Scholar] [Publisher Link]

[135] A.V. Mishonov et al., “High-Resolution Regional Ocean Climatologies with the Northwest Atlantic as an Example: A Review,” *Journal of Marine Science Research and Oceanography*, vol. 7, no. 1, pp. 1-32, 2024. [CrossRef] [Google Scholar] [Publisher Link]

[136] P. S. Monks et al., “Tropospheric Ozone and its Precursors from the Urban to the Global Scale from Air Quality to Short-Lived Climate Forcer,” *Atmospheric Chemistry and Physics*, vol. 15, no. 15, pp. 8889-8973, 2015. [CrossRef] [Google Scholar] [Publisher Link]

[137] Falco Monsees et al., “Relations between Cyclones and Ozone Changes in the Arctic Using Data from Satellite Instruments and the MOSAiC Ship Campaign,” *EGUsphere*, pp. 1-25, 2024. [CrossRef] [Google Scholar] [Publisher Link]

[138] Kathryn A. Moore et al., “Characterizing Ice Nucleating Particles Over the Southern Ocean Using Simultaneous Aircraft and Ship Observations,” *Journal of Geophysical Research: Atmospheres*, vol. 129, no. 2, pp. 1-20, 2024. [CrossRef] [Google Scholar] [Publisher Link]

[139] Michael R. Grose et al., “Australian Climate Warming: Observed Change from 1850 and Global Temperature Targets,” *Journal of Southern Hemisphere Earth Systems Science*, vol. 73, no. 1, pp. 30-43, 2023. [CrossRef] [Google Scholar] [Publisher Link]

[140] Gayan Pathirana et al., “Intermodel Relation between Present-Day Warm Pool Intensity and Future Precipitation Changes,” *Climate Dynamics*, vol. 62, pp. 345-355, 2024. [CrossRef] [Google Scholar] [Publisher Link]

[141] Victor M. Velasco Hererra et al., “Past and Future of Wildfires in Northern Hemisphere’s Boreal Forests,” *Forest Ecology and Management*, vol. 504, 2022. [CrossRef] [Google Scholar] [Publisher Link]

[142] Raghu Nadimpalli et al., “Effect of Vortex Initialization and Relocation Method in Anticipating Tropical Cyclone Track and Intensity over the Bay of Bengal,” *Pure and Applied Geophysics*, vol. 178, no. 10, pp. 4049-4071, 2021. [CrossRef] [Google Scholar] [Publisher Link]

[143] M.M. Nageswararao, Yuejian Zhu, and Vijay Tallapragada, “Prediction Skill of GEFSv12 for Southwest Summer Monsoon Rainfall and Associated Extreme Rainfall Events on Extended Range Scale over India,” *Weather and Forecasting*, vol. 37, no. 7, pp. 1135-1156, 2022. [CrossRef] [Google Scholar] [Publisher Link]

[144] Robert H. Nazarian et al., “Projected Changes in Mean and Extreme Precipitation Over Northern Mexico,” *Journal of Climate*, vol. 37, no. 8, pp. 2405-2422, 2024. [CrossRef] [Google Scholar] [Publisher Link]

[145] Takuro Aizawa, Naga Oshima, and Seiji Yukimoto, “Contributions of Anthropogenic Aerosol Forcing and Multidecadal Internal Variability to Mid-20th Century Arctic Cooling-CMIP6/DAMIP Multimodel Analysis,” *Geophysical Research Letters*, vol. 49, no. 4, pp. 1-12, 2022. [CrossRef] [Google Scholar] [Publisher Link]

[146] George J. Boer et al., “Verification Data and the Skill of Decadal Predictions,” *Frontiers in Climate*, vol. 4, pp. 1-15, 2022. [CrossRef] [Google Scholar] [Publisher Link]

[147] Keneshia Hibbert et al., “Changes to Sea Surface Temperatures and Vertical Wind Shear and their Influence on Tropical Cyclone Activity in the Caribbean and the Main Developing Region,” *Atmosphere*, vol. 14, no. 6, pp. 1-17, 2023. [CrossRef] [Google Scholar] [Publisher Link]

[148] Wen Chen et al., “Recent Advances in Understanding Multi-scale Climate Variability of the Asian Monsoon,” *Advances in Atmospheric Sciences*, vol. 40, pp. 1429-1456, 2023. [CrossRef] [Google Scholar] [Publisher Link]

[149] Chloe Brimicombe et al., “Wet Bulb Globe Temperature: Indicating Extreme Heat Risk on a Global Grid,” *GeoHealth*, vol. 7, no. 2, pp. 1-14, 2023. [CrossRef] [Google Scholar] [Publisher Link]

[150] Florian Ladstädter, Andrea K. Steiner, and Hans Gleisner, “Resolving the 21st Century Temperature Trends of the Upper Troposphere–Lower Stratosphere with Satellite Observations,” *Scientific Reports*, vol. 13, pp. 1-8, 2023. [CrossRef] [Google Scholar] [Publisher Link]

[151] Peter O’Neill et al., “Evaluation of the Homogenization Adjustments Applied to European Temperature Records in the Global Historical Climatology Network Dataset,” *Atmosphere*, vol. 13, no. 2, pp. 1-21, 2022. [CrossRef] [Google Scholar] [Publisher Link]

[152] G. Shanmugam, “200 Years of Fossil Fuels and Climate Change (1900–2100),” *Journal of the Geological Society of India*, vol. 99, pp. 1043-1062, 2023. [CrossRef] [Google Scholar] [Publisher Link]

[153] Christoph Kalicinsky, and Ralf Koppmann, “Multi-Decadal Oscillations of Surface Temperatures and the Impact on Temperature Increases,” *Scientific Reports*, vol. 12, pp. 1-10, 2022. [CrossRef] [Google Scholar] [Publisher Link]

[154] Robin Noyelle et al., “Maximal Reachable Temperatures for Western Europe in Current Climate,” *Environmental Research Letters*, vol. 18, no. 9, pp. 1-13, 2023. [CrossRef] [Google Scholar] [Publisher Link]

[155] Krishna K. Osuri et al., “Error Characterization of ARW Model in Forecasting Tropical Cyclone Rainfall Over North Indian Ocean,” *Journal of Hydrology*, vol. 590, 2020. [CrossRef] [Google Scholar] [Publisher Link]

[156] Zhipeng Pei et al., “A Method for Estimating the Background Column Concentration of CO_2 Using the Lagrangian Approach,” *IEEE Transactions on Geoscience and Remote Sensing*, vol. 60, pp. 1-12, 2022. [CrossRef] [Google Scholar] [Publisher Link]

[157] Miguel Perpina et al., “Link Between Opaque Cloud Properties and Atmospheric Dynamics in Observations and Simulations of Current Climate in the Tropics, and Impact on Future Predictions,” *Journal of Geophysical Research: Atmospheres*, vol. 126, no. 17, pp. 1-19, 2021. [CrossRef] [Google Scholar] [Publisher Link]

[158] Anh Phan, and Hiromichi Fukui, “Unusual Response of O_3 and CH_4 to NO_2 Emissions Reduction in Japan during the COVID-19 Pandemic,” *International Journal of Digital Earth*, vol. 17, no. 1, pp. 1-19, 2024. [CrossRef] [Google Scholar] [Publisher Link]

[159] Stanislav A. Yamashkin et al., “Improving the Efficiency of Deep Learning Methods in Remote Sensing Data Analysis: Geosystem Approach,” *IEEE Access*, vol. 8, pp. 179516-179529, 2020. [CrossRef] [Google Scholar] [Publisher Link]

[160] Roman Procyk, Shaun Lovejoy, and Raphael Hébert, “The Fractional Energy Balance Equation for Climate Projections through 2100,” *Earth System Dynamics*, vol. 13, no. 1, pp. 81-107, 2022. [CrossRef] [Google Scholar] [Publisher Link]

[161] Boyin Huang et al., “Uncertainty Estimates for Sea Surface Temperature and Land Surface Air Temperature in NOAAGlobalTemp Version 5,” *Journal of Climate*, vol. 33, no. 4, pp. 1351-1379, 2019. [CrossRef] [Google Scholar] [Publisher Link]

[162] Willie Soon, Ronan Connolly, and Michael Connolly, “Re-Evaluating the Role of Solar Variability on Northern Hemisphere Temperature Trends Since the 19th Century,” *Earth-Science Reviews*, vol. 150, pp. 409-452, 2015. [CrossRef] [Google Scholar] [Publisher Link]

[163] Christine Nam et al., “Changes in Universal Thermal Climate Index from Regional Climate Model Projections Over European Beaches,” *Climate Services*, vol. 34, pp. 1-16, 2024. [CrossRef] [Google Scholar] [Publisher Link]

[164] Veronika Valler et al., “ModE-RA: A Global Monthly Paleo-Reanalysis of the Modern Era 1421 to 2008,” *Scientific Data*, vol. 11, pp. 1-19, 2024. [CrossRef] [Google Scholar] [Publisher Link]

[165] Ali Salem Al-Sakkaf et al., “Assessing Exposure to Climate Extremes Over the Arabian Peninsula Using ERA5 Reanalysis Data: Spatial Distribution and Temporal Trends,” *Atmospheric Research*, vol. 300, 2024. [CrossRef] [Google Scholar] [Publisher Link]

[166] Eyob Betru Wegayehu, and Fiseha Behulu Muluneh, “Comparing Conceptual and Super Ensemble Deep Learning Models for Streamflow Simulation in Data-Scarce Catchments,” *Journal of Hydrology: Regional Studies*, vol. 52, pp. 1-24, 2024. [CrossRef] [Google Scholar] [Publisher Link]

[167] Jing Qian et al., “Meteorological Influences on Daily Variation and Trend of Summertime Surface Ozone Over Years of 2015-2020: Quantification for Cities in the Yangtze River Delta,” *Science of the Total Environment*, vol. 834, 2022. [CrossRef] [Google Scholar] [Publisher Link]

[168] Jiangjun Ran et al., “Contrasting Lake Changes in Tibet Revealed by Recent Multi-Modal Satellite Observations,” *Science of the Total Environment*, vol. 908, 2024. [CrossRef] [Google Scholar] [Publisher Link]

[169] Lia Rapella et al., “Climate Change on Extreme Winds Already Affects Off-Shore Wind Power Availability in Europe,” *Environmental Research Letters*, vol. 18, no. 3, pp. 1-10, 2023. [CrossRef] [Google Scholar] [Publisher Link]

[170] E. Real et al., “Atlas of Ozone Chemical Regimes in Europe,” *Atmospheric Environment*, vol. 320, pp. 1-17, 2024. [CrossRef] [Google Scholar] [Publisher Link]

[171] Tiantian Chen, Yuxi Wang, and Li Peng, “Advanced Time-Lagged Effects of Drought on Global Vegetation Growth and its Social Risk in the 21st Century,” *Journal of Environmental Management*, vol. 347, 2023. [CrossRef] [Google Scholar] [Publisher Link]

[172] Malcolm John Roberts et al., “Impact of Model Resolution on Tropical Cyclone Simulation Using the HighResMIP–PRIMAVERA Multimodel Ensemble,” *Journal of Climate*, vol. 33, no. 7, pp. 2557-2583, 2020. [CrossRef] [Google Scholar] [Publisher Link]

[173] Oussama Romdhani, Leo Matak, and Mostafa Momen, "Hurricane Track Trends and Environmental Flow Patterns under Surface Temperature Changes and Roughness Length Variations," *Weather and Climate Extremes*, vol. 43, pp. 1-15, 2024. [CrossRef] [Google Scholar] [Publisher Link]

[174] A. Routray et al., "Study Pre-and Post-Monsoon Storms Over NIO Region Using High Resolution IMDAA Reanalysis Dataset," *Climate Dynamics*, vol. 62, pp. 555-574, 2024. [CrossRef] [Google Scholar] [Publisher Link]

[175] V.N. Santhosh et al., "Assessing Biases in Atmospheric Parameters for Radiative Effects Estimation in Tropical Regions *Journal of Quantitative Spectroscopy and Radiative Transfer*, vol. 314, 2024. [CrossRef] [Google Scholar] [Publisher Link]

[176] Talukdar Sasanka, Krishna K. Osuri, and Dev Niyogi, "Machine Learning and Dynamics Based Error-Index Method for the Detection of Monsoon Onset Vortex Over the Arabian Sea: Climatology and Composite Structures," *Quarterly Journal of the Royal Meteorological Society*, vol. 149, no. 751, pp. 537-555, 2023. [CrossRef] [Google Scholar] [Publisher Link]

[177] Hongyu Chen, Tim Li, and Jing Cui, "The Reexamination of the Moisture-Vortex and Baroclinic Instabilities in the South Asian Monsoon," *Atmosphere*, vol. 15, no. 2, pp. 1-19, 2024. [CrossRef] [Google Scholar] [Publisher Link]

[178] Nicola Scafetta, "Advanced Testing of Low, Medium, and High ECS CMIP6 GCM Simulations Versus ERA5-T2m," *Geophysical Research Letters*, vol. 49, no. 6, pp. 1-13, 2022. [CrossRef] [Google Scholar] [Publisher Link]

[179] Abdallah Shaheen et al., "Winter AOD Trend Changes Over the Eastern Mediterranean and Middle East Region," *International Journal of Climatology*, vol. 41, no. 12, pp. 5516-5535, 2021. [CrossRef] [Google Scholar] [Publisher Link]

[180] Wenxiang Shen et al., "Improving BC Mixing State and CCN Activity Representation with Machine Learning in the Community Atmosphere Model Version 6 (CAM6)," *Journal of Advances in Modeling Earth Systems*, vol. 16, no. 1, pp. 1-25, 2024. [CrossRef] [Google Scholar] [Publisher Link]

[181] S.C. Sherwood et al., "An Assessment of Earth's Climate Sensitivity Using Multiple Lines of Evidence," *Reviews of Geophysics*, vol. 58, no. 4, pp. 1-93, 2020. [CrossRef] [Google Scholar] [Publisher Link]

[182] Vishal Singh, Anil Kumar Lohani, and Sanjay Kumar Jain, "Reconstruction of Extreme Flood Events by Performing Integrated Real-Time and Probabilistic Flood Modeling in the Periyar River Basin, Southern India," *Natural Hazards*, vol. 112, pp. 2433-2463, 2022. [CrossRef] [Google Scholar] [Publisher Link]

[183] Xin Su et al., "A High-Precision Aerosol Retrieval Algorithm (HiPARA) for Advanced Himawari Imager (AHI) Data: Development and Verification," *Remote Sensing of Environment*, vol. 253, 2021. [CrossRef] [Google Scholar] [Publisher Link]

[184] Agnieszka Sulikowska, and Agnieszka Wypych, "Heat Extremes in Europe's Changing Climate: Definitions, Causes, Trends, Effects," *Geographical Works*, no. 170, pp. 47-82, 2023. [Google Scholar] [Publisher Link]

[185] Carl Svenhag et al., "Implementing Detailed Nucleation Predictions in the Earth System Model EC-Earth3.3.4: Sulfuric Acid-Ammonia Nucleation," *EGUsphere*, pp. 1-28, 2024. [CrossRef] [Google Scholar] [Publisher Link]

[186] Keyvan Soltani et al., "Forecasting Monthly Fluctuations of Lake Surface Areas Using Remote Sensing Techniques and Novel Machine Learning Methods," *Theoretical and Applied Climatology*, vol. 143, pp. 713-735, 2021. [CrossRef] [Google Scholar] [Publisher Link]

[187] Qi Tang et al., "The Fully Coupled Regionally Refined Model of E3SM Version 2: Overview of the Atmosphere, Land, and River Results," *Geoscientific Model Development*, vol. 16, no. 13, pp. 3953-3995, 2023. [CrossRef] [Google Scholar] [Publisher Link]

[188] Chad W. Thackeray et al., "Constraining the Increased Frequency of Global Precipitation Extremes under Warming," *Nature Climate Change*, vol. 12, pp. 441-448, 2022. [CrossRef] [Google Scholar] [Publisher Link]

[189] Katherine R. Travis et al., "Limitations in Representation of Physical Processes Prevent Successful Simulation of $PM_{2.5}$ during KORUS-AQ," *Atmospheric Chemistry and Physics*, vol. 22, no. 12, pp. 7933-7958, 2022. [CrossRef] [Google Scholar] [Publisher Link]

[190] Sönke Dangendorf et al., "Acceleration of U.S. Southeast and Gulf Coast Sea-Level Rise Amplified by Internal Climate Variability," *Nature Communications*, vol. 14, pp. 1-11, 2023. [CrossRef] [Google Scholar] [Publisher Link]

[191] Sylvia G. Dee et al., "Tracking the Strength of the Walker Circulation with Stable Isotopes in Water Vapor," *Journal of Geophysical Research: Atmospheres*, vol. 123, no. 14, pp. 7254-7270, 2018. [CrossRef] [Google Scholar] [Publisher Link]

[192] Xiao Dong et al., "Climate Influence on the 2019 Fires in Amazonia," *Science of the Total Environment*, vol. 794, 2021. [CrossRef] [Google Scholar] [Publisher Link]

[193] Francisco Estrada, and Pierre Perron, "Disentangling the Trend in the Warming of Urban Areas into Global and Local Factors," *Annals of the New York Academy of Sciences*, vol. 1504, no. 1, pp. 230-246, 2021. [CrossRef] [Google Scholar] [Publisher Link]

[194] Papa Fall et al., "Bias-Corrected CMIP5 Projections for Climate Change and Assessments of Impact on Malaria in Senegal under the VECTRI Model," *Tropical Medicine and Infectious Disease*, vol. 8, no. 6, pp. 1-29, 2023. [CrossRef] [Google Scholar] [Publisher Link]

[195] Andrew F. Feldman et al., "A Multi-Satellite Framework to Rapidly Evaluate Extreme Biosphere Cascades: The Western US 2021 Drought and Heatwave," *Global Change Biology*, vol. 29, no. 13, pp. 3634-3651, 2023. [CrossRef] [Google Scholar] [Publisher Link]

[196] Carlos Antonio Fernandez-Palomino et al., "High-Resolution Climate Projection Dataset Based on CMIP6 for Peru and Ecuador: BASD-CMIP6-PE," *Scientific Data*, vol. 11, pp. 1-14, 2024. [CrossRef] [Google Scholar] [Publisher Link]

[197] Stephanie Fiedler et al., "Radiative Effects of Reduced Aerosol Emissions during the COVID-19 Pandemic and the Future Recovery," *Atmospheric Research*, vol. 264, pp. 1-11, 2021. [CrossRef] [Google Scholar] [Publisher Link]

[198] Shubham A. Gade, and Devidas D. Khedkar, “Implication of Climate Change on Crop Water Requirement in the Semi-Arid Region of Western Maharashtra, India,” *Environmental Monitoring and Assessment*, vol. 195, 2023. [CrossRef] [Google Scholar] [Publisher Link]

[199] Meng Gao et al., “Large-Scale Climate Patterns Offer Preseasonal Hints on the Co-Occurrence of Heat Wave and O_3 Pollution in China,” *Proceedings of the National Academy of Sciences*, vol. 120, no. 26, pp. 1-9, 2023. [CrossRef] [Google Scholar] [Publisher Link]

[200] Chaim I. Garfinkel et al., “Stratospheric Variability Contributed to and Sustained the Recent Hiatus in Eurasian Winter Warming,” *Geophysical Research Letters*, vol. 44, no. 1, pp. 374-382, 2017. [CrossRef] [Google Scholar] [Publisher Link]

[201] Ronald Gelaro et al., “The Modern-Era Retrospective Analysis for Research and Applications, Version 2 (MERRA-2),” *Journal of Climate*, vol. 30, no. 13, pp. 5419-5454, 2017. [CrossRef] [Google Scholar] [Publisher Link]

[202] Nikos Gialesakis et al., “A Twenty Year Record of Greenhouse Gases in the Eastern Mediterranean Atmosphere,” *Science of the Total Environment*, vol. 864, 2023. [CrossRef] [Google Scholar] [Publisher Link]

[203] Li Gong et al., “Middle Pleistocene Re-Organization of Australian Monsoon,” *Nature Communications*, vol. 14, pp. 1-14, 2023. [CrossRef] [Google Scholar] [Publisher Link]

[204] Clare Goodess et al., “Climate Change Projections for Sustainable and Healthy Cities,” *Buildings and Cities*, vol. 2, no. 1, pp. 812-836, 2021. [CrossRef] [Google Scholar] [Publisher Link]

[205] Stephen G. Hesterberg, Kendal Jackson, and Susan S. Bell, “Climate Drives Coupled Regime Shifts Across Subtropical Estuarine Ecosystems,” *Proceedings of the National Academy of Sciences*, vol. 119, no. 33, pp. 1-8, 2022. [CrossRef] [Google Scholar] [Publisher Link]

[206] Chibuike Chiedozie Ibebuchi, and Cameron C. Lee, “Circulation Patterns Associated with Trends in Summer Temperature Variability Patterns in North America,” *Scientific Reports*, vol. 13, pp. 1-13, 2023. [CrossRef] [Google Scholar] [Publisher Link]

[207] Yuming Jin et al., “Impact of Changing Winds on the Mauna Loa CO_2 Seasonal Cycle in Relation to the Pacific Decadal Oscillation,” *Journal of Geophysical Research: Atmospheres*, vol. 127, no. 13, pp. 1-15, 2022. [CrossRef] [Google Scholar] [Publisher Link]

[208] Sara Karam et al., “Assessing the Impacts of Climate Change on Climatic Extremes in the Congo River Basin,” *Climatic Change*, vol. 170, pp. 1-24, 2022. [CrossRef] [Google Scholar] [Publisher Link]

[209] Thomas R. Karl, and Kevin E. Trenberth, “Modern Global Climate Change,” *Science*, vol. 302, no. 5651, pp. 1719-1723, 2003. [CrossRef] [Google Scholar] [Publisher Link]

[210] Ali Katal et al., “Outdoor Heat Stress Assessment Using an Integrated Multi-Scale Numerical Weather Prediction System: A Case Study of a Heatwave in Montreal,” *Science of the Total Environment*, vol. 865, 2022. [CrossRef] [Google Scholar] [Publisher Link]

[211] Christian A. Koch et al., “Climate Change and Obesity,” *Hormone and Metabolic Research*, vol. 53, no. 9, pp. 575-587, 2021. [CrossRef] [Google Scholar] [Publisher Link]

[212] Jayanarayanan Kuttippurath et al., “The Increasing Atmospheric CO_2 over India: Comparison to Global Trends,” *iScience*, vol. 25, no. 8, pp. 1-18, 2022. [CrossRef] [Google Scholar] [Publisher Link]

[213] Shaohua Zhao et al., “The Role of Satellite Remote Sensing in Mitigating and Adapting to Global Climate Change,” *Science of the Total Environment*, vol. 904, 2023. [CrossRef] [Google Scholar] [Publisher Link]

[214] Fabrice Lacroix et al., “Mismatch of N Release from the Permafrost and Vegetative Uptake Opens Pathways of Increasing Nitrous Oxide Emissions in the High Arctic,” *Global Change Biology*, vol. 28, no. 20, pp. 5973-5990, 2022. [CrossRef] [Google Scholar] [Publisher Link]

[215] Michael J. Lecours et al., “Atlas of ACE Spectra of Clouds and Aerosols,” *Journal of Quantitative Spectroscopy and Radiative Transfer*, vol. 292, pp. 1-15, 2022. [CrossRef] [Google Scholar] [Publisher Link]

[216] Y.C. Lee, M.O. Wenig, and K.L. Chan, “Oceanic and Atmospheric Anomalies Associated with Extreme Precipitation Events in China 1983-2020,” *Air Quality, Atmosphere & Health*, vol. 16, pp. 881-895, 2023. [CrossRef] [Google Scholar] [Publisher Link]

[217] Luca Lelli et al., “Satellite Remote Sensing of Regional and Seasonal Arctic Cooling Showing a Multi-Decadal Trend Towards Brighter and More Liquid Clouds,” *Atmospheric Chemistry and Physics*, vol. 23, no. 4, pp. 2579-2611, 2023. [CrossRef] [Google Scholar] [Publisher Link]

[218] Baosheng Li et al., “Middle East Warming in Spring Enhances Summer Rainfall over Pakistan,” *Nature Communications*, vol. 14, pp. 1-7, 2023. [CrossRef] [Google Scholar] [Publisher Link]

[219] Xihong Lian et al., “Future Climate Imposes Pressure on Vulnerable Ecological Regions in China,” *Science of the Total Environment*, vol. 858, no. 3, 2022. [CrossRef] [Google Scholar] [Publisher Link]

[220] Antje Weisheimer et al., “Variability of ENSO Forecast Skill in 2-Year Global Reforecasts Over the 20th Century,” *Geophysical Research Letters*, vol. 49, no. 10, pp. 1-12, 2022. [CrossRef] [Google Scholar] [Publisher Link]

[221] Jiayuan Liao et al., “Water-Energy-Vegetation Nexus Explain Global Geographical Variation in Surface Urban Heat Island Intensity,” *Science of the Total Environment*, vol. 895, 2023. [CrossRef] [Google Scholar] [Publisher Link]

[222] Laibao Liu et al., “Increasingly Negative Tropical Water–Interannual CO_2 Growth Rate Coupling,” *Nature*, vol. 618, pp. 755-760, 2023. [CrossRef] [Google Scholar] [Publisher Link]

[223] Joseph W. Lockwood et al., “Correlation between Sea-Level Rise and Aspects of Future Tropical Cyclone Activity in CMIP6 Models,” *Earth’s Future*, vol. 10, no. 4, pp. 1-19, 2022. [CrossRef] [Google Scholar] [Publisher Link]

[224] Xiao Lu et al., “Surface and Tropospheric Ozone Trends in the Southern Hemisphere since 1990: Possible Linkages to Poleward Expansion of the Hadley Circulation,” *Science Bulletin*, vol. 64, no. 6, pp. 400-409, 2018. [CrossRef] [Google Scholar] [Publisher Link]

[225] J.M. Maia, R.M. Curado da Silva, and J. Mingacho, “Evaluation of Effective Dose for Gamma-Rays of Terrestrial Gamma-Ray Flashes in Aviation: Spectral-and Atmosphere-Effects,” *Radiation Physics and Chemistry*, vol. 215, pp. 1-111, 2024. [CrossRef] [Google Scholar] [Publisher Link]

[226] L. Nazarenko et al., “Interactive Nature of Climate Change and Aerosol Forcing,” *Journal of Geophysical Research: Atmospheres*, vol. 122, no. 6, pp. 3457-3480, 2017. [CrossRef] [Google Scholar] [Publisher Link]

[227] Yang Li et al., “Future Changes in the Intensity and Frequency of Precipitation Extremes over China in a Warmer World: Insight from a Large Ensemble,” *PLoS One*, vol. 16, no. 5, pp. 1-12, 2021. [CrossRef] [Google Scholar] [Publisher Link]

[228] Miguel Nogueira et al., “Upgrading Land-Cover and Vegetation Seasonality in the ECMWF Coupled System: Verification with FLUXNET Sites, METEOSAT Satellite Land Surface Temperatures, and ERA5 Atmospheric Reanalysis,” *Journal of Geophysical Research: Atmospheres*, vol. 126, no. 15, pp. 1-26, 2021. [CrossRef] [Google Scholar] [Publisher Link]

[229] Kimberly A. Novick et al., “Informing Nature-Based Climate Solutions for the United States with the Best-Available Science,” *Global Change Biology*, vol. 28, no. 12, pp. 3778-3794, 2022. [CrossRef] [Google Scholar] [Publisher Link]

[230] Shantanu Kumar Pani et al., “Long-Term Observation of Columnar Aerosol Optical Properties over the Remote South China Sea,” *Science of the Total Environment*, vol. 905, 2023. [CrossRef] [Google Scholar] [Publisher Link]

[231] Qihua Peng et al., “Surface Warming–Induced Global Acceleration of Upper Ocean Currents,” *Science Advances*, vol. 8, no. 16, pp. 1-12, 2022. [CrossRef] [Google Scholar] [Publisher Link]

[232] R. Peter et al., “A High Concentration CO_2 Pool over the Indo-Pacific Warm Pool,” *Scientific Reports*, vol. 13, pp. 1-11, 2023. [CrossRef] [Google Scholar] [Publisher Link]

[233] Stephen Po-Chedley et al., “Internal Variability and Forcing Influence Model–Satellite Differences in the Rate of Tropical Tropospheric Warming,” *Proceedings of the National Academy of Sciences*, vol. 119, no. 47, pp. 1-8, 2022. [CrossRef] [Google Scholar] [Publisher Link]

[234] Guoyu Ren et al., “Observed Changes in Temperature and Precipitation Over Asia, 1901-2020,” *Climate Research*, vol. 90, pp. 31-43, 2023. [CrossRef] [Google Scholar] [Publisher Link]

[235] Yun Qian et al., “Urbanization Impact on Regional Climate and Extreme Weather: Current Understanding, Uncertainties, and Future Research Directions,” *Advances in Atmospheric Sciences*, vol. 39, pp. 819-860, 2022. [CrossRef] [Google Scholar] [Publisher Link]

[236] Harsimranjit Kaur Romana et al., “Analysis of Air and Soil Quality around Thermal Power Plants and Coal Mines of Singrauli Region, India,” *International Journal of Environmental Research and Public Health*, vol. 19, no. 18, pp. 1-22, 2022. [CrossRef] [Google Scholar] [Publisher Link]

[237] Alfonso Saiz-Lopez et al., “Natural Short-Lived Halogens Exert an Indirect Cooling Effect on Climate,” *Nature*, vol. 618, pp. 967-973, 2023. [CrossRef] [Google Scholar] [Publisher Link]

[238] Seyni Salack et al., “Low-Cost Adaptation Options to Support Green Growth in Agriculture, Water Resources, and Coastal Zones,” *Scientific Reports*, vol. 12, pp. 1-16, 2022. [CrossRef] [Google Scholar] [Publisher Link]

[239] Benjamin D. Santer et al., “Quantifying Stochastic Uncertainty in Detection Time of Human-Caused Climate Signals,” *Proceedings of the National Academy of Sciences*, vol. 116, no. 40, pp. 19821-19827, 2019. [CrossRef] [Google Scholar] [Publisher Link]

[240] C.E. Scott et al., “Impact on Short-Lived Climate Forcers Increases Projected Warming Due to Deforestation,” *Nature Communications*, vol. 9, pp. 1-9, 2018. [CrossRef] [Google Scholar] [Publisher Link]

[241] Martín Senande-Rivera, Damián Insua-Costa, and Gonzalo Miguez-Macho, “Spatial and Temporal Expansion of Global Wildland Fire Activity in Response to Climate Change,” *Nature Communications*, vol. 13, pp. 1-9, 2022. [CrossRef] [Google Scholar] [Publisher Link]

[242] Swathi Shetty, Pruthviraj Umesh, and Amba Shetty, “Future Transition in Climate Extremes over Western Ghats of India Based on CMIP6 Models,” *Environmental Monitoring and Assessment*, vol. 195, 2023. [CrossRef] [Google Scholar] [Publisher Link]

[243] Hideo Shiogama et al., “Emergent Constraints on Future Precipitation Changes,” *Nature*, vol. 602, pp. 612-616, 2022. [CrossRef] [Google Scholar] [Publisher Link]

[244] Benjamin M. Sleeter et al., “Operational Assessment Tool for Forest Carbon Dynamics for the United States: A New Spatially Explicit Approach Linking the LUCAS and CBM-CFS3 Models,” *Carbon Balance and Management*, vol. 17, pp. 1-26, 2022. [CrossRef] [Google Scholar] [Publisher Link]

[245] Jiecheng Song et al., “Data driven Pathway Analysis and Forecast of Global Warming and Sea Level Rise,” *Scientific Reports*, vol. 13, pp. 1-14, 2023. [CrossRef] [Google Scholar] [Publisher Link]

[246] Aurélien Stolzenbach et al., “Martian Atmospheric Aerosols Composition and Distribution Retrievals during the First Martian Year of NOMAD/TGO Solar Occultation Measurements: 1. Methodology and Application to the MY 34 Global Dust Storm,” *Journal of Geophysical Research Planets*, vol. 128, no. 11, pp. 1-27, 2023. [CrossRef] [Google Scholar] [Publisher Link]

[247] Lili Tan et al., “Assessment of the Sustainability of Groundwater Utilization and Crop Production under Optimized Irrigation Strategies in the North China Plain under Future Climate Change,” *Science of the Total Environment*, vol. 899, 2023. [CrossRef] [Google Scholar] [Publisher Link]

[248] M. Tanarhte et al., “Severe Droughts in North Africa: A Review of Drivers, Impacts and Management,” *Earth-Science Reviews*, vol. 250, 2024. [CrossRef] [Google Scholar] [Publisher Link]

[249] Penghao Tian et al., “Ionospheric Irregularity Reconstruction Using Multisource Data Fusion Via Deep Learning,” *Atmospheric Chemistry and Physics*, vol. 23, no. 20, pp. 13413-13431, 2023. [CrossRef] [Google Scholar] [Publisher Link]

[250] Amar Deep Tiwari et al., “A Synthesis of Hydroclimatic, Ecological, and Socioeconomic Data for Transdisciplinary Research in the Mekong,” *Scientific Data*, vol. 10, pp. 1-26, 2023. [CrossRef] [Google Scholar] [Publisher Link]

[251] Ioanna Tsagouri et al., “Ionosphere Variability I: Advances in Observational, Monitoring and Detection Capabilities,” *Advances in Space Research*, 2023. [CrossRef] [Google Scholar] [Publisher Link]

[252] I-Chun Tsai et al., “Projecting Ozone Impact on Crop Yield in Taiwan under Climate Warming,” *Science of the Total Environment*, vol. 846, 2022. [CrossRef] [Google Scholar] [Publisher Link]

[253] György Varga et al., “Saharan, Aral-Caspian and Middle East Dust Travels to Finland (1980-2022),” *Environment International*, vol. 180, pp. 1-14, 2023. [CrossRef] [Google Scholar] [Publisher Link]

[254] R.S.W. Van De Wal et al., “A High-End Estimate of Sea Level Rise for Practitioners,” *Earth’s Future*, vol. 10, no. 11, pp. 1-24, 2022. [CrossRef] [Google Scholar] [Publisher Link]

[255] Jiapeng Miao, and Dabang Jiang, “Multidecadal Variations in East Asian Winter Temperature Since 1880: Internal Variability Versus External Forcing,” *Geophysical Research Letters*, vol. 49, no. 20, pp. 1-9, 2022. [CrossRef] [Google Scholar] [Publisher Link]

[256] Nischal, Raju Attada, and Kieran M.R. Hunt, “Evaluating Winter Precipitation over the Western Himalayas in a High-Resolution Indian Regional Reanalysis Using Multisource Climate Datasets,” *Journal of Applied Meteorology and Climatology*, vol. 61, no. 11, pp. 1613-1633, 2022. [CrossRef] [Google Scholar] [Publisher Link]

[257] Weiping Ding et al., “Explainability of Artificial Intelligence Methods, Applications and Challenges: A Comprehensive Survey,” *Information Sciences*, vol. 615, pp. 238-292, 2022. [CrossRef] [Google Scholar] [Publisher Link]

[258] Antoine Allam et al., “Mediterranean Specific Climate Classification and Future Evolution under RCP Scenarios,” *Hydrology and Earth System Sciences Discussions*, pp. 1-25, 2019. [CrossRef] [Google Scholar] [Publisher Link]

[259] Zilefac Elvis Asong et al., “Regional Scenarios of Change Over Canada: Future Climate Projections,” *Hydrology and Earth System Sciences Discussions*, pp. 1-40, 2019. [CrossRef] [Google Scholar] [Publisher Link]

[260] Roberto San José et al., “Global Climate Driven Effects on Urban Air Pollution Simulations Using Very High Spatial Resolution,” *International Journal of Environment and Pollution*, vol. 66, no. 1-3, pp. 143-161, 2019. [CrossRef] [Google Scholar] [Publisher Link]

[261] Jorge J. Escurra Aguirre, and Charles A. Jones, “Water Use Efficiency and Storage Capacity in South Asia by 2050,” *Journal of the American Water Resources Association*, vol. 55, no. 6, pp. 1519-1539, 2019. [CrossRef] [Google Scholar] [Publisher Link]

[262] Yulong Yao et al., “Rapid Changes in Land-Sea Thermal Contrast across China’s Coastal Zone in a Warming Climate,” *Journal of Geophysical Research: Atmospheres*, vol. 124, no. 4, pp. 2049-2067, 2019. [CrossRef] [Google Scholar] [Publisher Link]

[263] Yong Zhang et al., “Glacier Surface Mass Balance in the Suntar-Khayata Mountains, Northeastern Siberia,” *Water*, vol. 11, no. 9, pp. 1-21, 2019. [CrossRef] [Google Scholar] [Publisher Link]

[264] Armin Ahmadi et al., “Assessment of MC&MCMC Uncertainty Analysis Frameworks on SWAT Model by Focusing on Future Runoff Prediction in a Mountainous Watershed Via CMIP5 Models,” *Journal of Water and Climate Change*, vol. 11, no. 4, pp. 1811-1828, 2019. [CrossRef] [Google Scholar] [Publisher Link]

[265] Pengfei Han et al., “Projected Changes of Alpine Grassland Carbon Dynamics in Response to Climate Change and Elevated CO_2 Concentrations under Representative Concentration Pathways (RCP) Scenarios,” *PLoS One*, vol. 14, no. 7, 2019. [CrossRef] [Google Scholar] [Publisher Link]

[266] Samaneh Lesani, and Mohammad Hossein Niksokhan, “Climate Change Impact on Caspian Sea Wave Conditions in the Noshahr Port,” *Ocean Dynamics*, vol. 69, pp. 1287-1310, 2019. [CrossRef] [Google Scholar] [Publisher Link]

[267] Xiaomin Zeng et al., “Spatial Patterns of Precipitation-Induced Moisture Availability and their Effects on the Divergence of Conifer Stem Growth in the Western and Eastern Parts of China’s Semi-Arid Region,” *Forest Ecology and Management*, vol. 451, 2019. [CrossRef] [Google Scholar] [Publisher Link]

[268] Athira Krishnan, and Prasad K. Bhaskaran, “Performance of CMIP5 Wind Speed from Global Climate Models for the Bay of Bengal Region,” *International Journal of Climatology*, vol. 40, no. 7, pp. 3398-3416, 2020. [CrossRef] [Google Scholar] [Publisher Link]

[269] Sungbo Shim et al., “Effects of Anthropogenic and Natural Forcings on the Summer Temperature Variations in East Asia during the 20th Century,” *Atmosphere*, vol. 10, no. 11, pp. 1-22, 2019. [CrossRef] [Google Scholar] [Publisher Link]

[270] Mojisola Oluwayemisi Adeniyi, “On the Influence of Variations in Solar Irradiance on Climate: A Case Study of West Africa,” *Earth Systems and Environment*, vol. 3, pp. 189-202, 2019. [CrossRef] [Google Scholar] [Publisher Link]

[271] Jorge E. González et al., “New York City Panel on Climate Change 2019 Report Chapter 2: New Methods for Assessing Extreme Temperatures, Heavy Downpours, and Drought,” *Annals of the New York Academy of Sciences*, vol. 1439, no. 1, pp. 30-70, 2019. [CrossRef] [Google Scholar] [Publisher Link]

[272] Mahsa Jahandideh-Tehrani et al., “Review of Climate Change Impacts on Predicted River Streamflow in Tropical Rivers,” *Environmental Monitoring and Assessment*, vol. 191, 2019. [CrossRef] [Google Scholar] [Publisher Link]

[273] Iqbal H. Sarker, “Machine Learning: Algorithms, Real-World Applications and Research Directions,” *SN Computer Science*, vol. 2, pp. 1-21, 2021. [CrossRef] [Google Scholar] [Publisher Link]

[274] S. Ragettli et al., “Climate Change Impacts on Summer Flood Frequencies in Two Mountainous Catchments in China and Switzerland,” *Hydrology Research*, vol. 52, no. 1, pp. 4-25, 2019. [CrossRef] [Google Scholar] [Publisher Link]

[275] Hamed Yassaghi, Nariman Mostafavi, and Simi Hoque, “Evaluation of Current and Future Hourly Weather Data Intended for Building Designs: A Philadelphia Case Study,” *Energy and Buildings*, vol. 199, pp. 491-511, 2019. [CrossRef] [Google Scholar] [Publisher Link]

[276] Neil C. Swart et al., “The Canadian Earth System Model Version 5 (CanESM5.0.3),” *Geoscientific Model Development*, vol. 12, no. 11, pp. 4823-4873, 2019. [CrossRef] [Google Scholar] [Publisher Link]

[277] Peter M. Caldwell et al., “The DOE E3SM Coupled Model Version 1: Description and Results at High Resolution,” *Journal of Advances in Modeling Earth Systems*, vol. 11, no. 12, pp. 4095-4146, 2019. [CrossRef] [Google Scholar] [Publisher Link]

[278] E.G. Nisbet et al., “Very Strong Atmospheric Methane Growth in the 4 Years 2014-2017: Implications for the Paris Agreement,” *Global Biogeochemical Cycles*, vol. 33, no. 3, pp. 318-342, 2019. [CrossRef] [Google Scholar] [Publisher Link]

[279] Jean-Christophe Golaz et al., “The DOE E3SM Coupled Model Version 1: Overview and Evaluation at Standard Resolution,” *Journal of Advances in Modeling Earth Systems*, vol. 11, no. 7, pp. 2089-2129, 2019. [CrossRef] [Google Scholar] [Publisher Link]

[280] Raktima Dey et al., “A Review of Past and Projected Changes in Australia’s Rainfall,” *Wiley Interdisciplinary Reviews Climate Change*, vol. 10, no. 3, 2019. [CrossRef] [Google Scholar] [Publisher Link]

[281] A.F. Bais et al., “Ozone-Climate Interactions and Effects on Solar Ultraviolet Radiation,” *Photochemical & Photobiological Sciences*, vol. 18, no. 3, pp. 602-640, 2019. [CrossRef] [Google Scholar] [Publisher Link]

[282] Shichang Kang et al., “Linking Atmospheric Pollution to Cryospheric Change in the Third Pole Region: Current Progress and Future Prospects,” *National Science Review*, vol. 6, no. 4, pp. 796-809, 2019. [CrossRef] [Google Scholar] [Publisher Link]

[283] Aryeh Feinberg et al., “Improved Tropospheric and Stratospheric Sulfur Cycle in the Aerosol-Chemistry-Climate Model SOCOL-AERv2,” *Geoscientific Model Development*, vol. 12, no. 9, pp. 3863-3887, 2019. [CrossRef] [Google Scholar] [Publisher Link]

Appendix A.

List of notations defined for the machine learning algorithms [257,282]

ϕ	Time series of model and observation temperature anomalies, the global lower troposphere.
ψ	Time series of model and observation temperature anomalies, global mid–troposphere
ф	Difference between observationally constrained and multi–model mean dynamic components (AMIP4K and AMIP) of cloud feedback as a function of ω_{500}
ρ_ϕ	Ascending Local Equator Crossing Time (LECT) for MetOp–A, Aqua, Suomi National Polar-Orbiting Partnership (S–NPP), and NOAA Joint Polar Satellite System–1 (NOAA–20) polar–orbiting satellites[1]
ν_ϕ	ROC values for corresponding AUC data
Ƙ	Northern and Southern Hemisphere surface air temperature series estimated from the 172 (NH 109, SH 63) subset[2]
Þ	Flajolet–Odlyzko constant
Ḧ	Surface air temperature series estimated for Australia. $(10^{\circ}-50^{\circ}\mathrm{S}, 110^{\circ}-160^{\circ}\mathrm{E})$ and South America $(5^{\circ}-55^{\circ}\mathrm{S}, 30^{\circ}-80^{\circ}\mathrm{W})$[2]
ξ	Khinchin–Lévy constant
Ʈ	Monthly global mean temperatures in the midtroposphere (TMT) anomaly time series from Aqua, MetOp–A, Suomi National Polar Orbiting Partnership (S–NPP), and NOAA Joint Polar Satellite System–1 (NOAA–20) and the reference TMT (RFTMT) time series merged from satellite–data
Ḡ	Inter–satellite difference time series before the merging. Anomalies are relative to a monthly climatology of RFTMT for the MetOp–A period from January 2008 to December 2017 (uncertainties in trend calculations represent 95% confidence intervals with autocorrelation adjustments)
η	Global–mean TMT monthly anomalies[3]
μ	Global mean anomaly difference time series between existing datasets and RFTMT[3]
Ƴ	U–net MSE, FNR and POFD scores during training of the baseline model
Ü	Pareto fronts projected for the three indices in the loss function needed for the comparison of precipitation outputs
ζ	Riemann zeta function representing Dirichlet series
θ	Lemniscate constant representing the integral covariance of stochastic data
α	Monthly TMT anomalies averaged over the global ocean[3]
β	Anomaly Difference Time Series between existing data sets and RFTMT over the global ocean[3]
Ω_θ	Hyper–harmonic median of Dirichlet series
λ_α	Monthly TMT anomalies averaged over the global land[3]
λ_β	Anomaly Difference Time Series between existing data sets and RFTMT over the global land[3]
K	Kullback–Leibler divergent coefficient
Ꞷ$_n$	Sylvester sequence of Eigen solutions
Ʋ	Model ECS values plotted against model warming trends
Ṝ	Probability density function[4] of vertical velocity at $500\mathrm{hPa}$ using a bin width of $2\mathrm{hPaday}^{-1}$
ƒ	Bessel corrected variance
σ_ϕ	Fourier integral of the cloud feedback components for each of the CMIP6 AMIP4K simulations[5]
χ	Bernoulli continuity coefficient for Gregory's series
Б$_\tau$	Recursive Bayesian Estimation of relative conjugate error

[1] The descending LECT was performed 12 h after ascending LECT. This study used data from 08/2002–12/2009 for Aqua, 01/2008–12/2017 for MetOp–A, 01/2012–12/2020 for S–NPP, and 01/2018–12/2020 for NOAA–20. During the overlap period, the NOAA–20 overlaid the S–NPP time series.

[2] Surface air temperatures for geographical areas in the Northern and Southern Hemispheres between 1851 and 1993. Standard meteorological seasons were used, with winters lasting from December to February, designated as January. The statistics revealed anomalies between 1961 and 1990. The data series in this and the subsequent graphs were smoothed using a 10–year Gaussian filter.

[3] Temperatures in the mid–troposphere (TMT) time series were compared from August 2002 to December 2020 using existing datasets and the reference TMT (RFTMT). Time data were drawn such that the mean difference between 8 August 2002 and 12 December 2003 was zero.

[4] The average long–wave and short–wave cloud radiative effects (CRE) for each vertical velocity bin. The observed values are the average of three re–analyses combined with contemporaneous CREs from the CERES–EBAF dataset, with gray shading representing the dispersion of the re–analyses. The CFMIP values are the multi–model averages for the 13 AMIP simulations shown in Table 15 for the years indicated in the legend.

[5] The feedback was based on the differences between the AMIP4K and AMIP trials. The current climate's observed ω500 distributions and CRE–ω_{500} associations are used to determine the dynamic, thermodynamic, and covariation components.

Appendix B. List of Tables

Table 1. Models participating in CMIP1 and CMIP2

Model	Flux correction	Run length (year)
BMRC	none	106
CCCMA	heat, water	160
CCSR	heat, water	50
CERFACS	none	50
COLA	none	60
CSIRO	heat, water, momentum	110
DOE PCM	none	310
ECHAM1+LSG	heat, water, momentum	970
ECHAM3+LSG	heat, water, momentum	1100
ECHAM4+OPYC3	heat, water (annual mean)	250
GFDL	heat, water	1100
GISS (Miller)	none	95
GISS (Russell)	none	96
IAP/LASG	sea surface salinity (reference to base)	60
LMD/IPSL	none	25
MRI	heat, water	120
NCAR (CSM)	none	310
NCAR (CRU)	none	120
NRL	sea ice (reference to base)	40
UKMO (HadCM2)	heat, water	1090
UKMO (HadCM3)	none	90

Table 2. Available information from RCPs and resolution (as per references [17–28])

	Resolution (sectors)	Resolution (geographical)
Emissions of greenhouse gases		
CO_2	energy sector, land	Global and for 5 regions
CH_4	12 sectors	0.5° × 0.5° grid
N_2O, HFCs, PFCs, CFCs, SF_6	–	Global and for 5 regions
Emissions aerosols and chemically active gases		
SO_2, Black Carbon (BC), Organic Carbon (OC),CO,NO_x,VOCs,NH_3	12 sectors	0.5° × 0.5° grid
Speciation of VOC emissions	–	0.5° × 0.5° grid
Concentration of greenhouse gases		
(CO_2, CH_4, N_2O, HFCs, PFCs, CFCs, SF_6)	–	Global
Concentrations of aerosols and chemically active gases		
(O_3, Aerosols, N deposition, S deposition)	–	0.5° × 0.5° grid
Land–use/land–cover data		
	cropland, pasture, primary vegetation, secondary vegetation, forests	0.5° × 0.5° grid with subgrid fractions, (annual maps and transition matrices including wood harvesting)

Table 3. Overview of representative concentration pathways (RCPs)

	Description	Publication–IA Model
RCP8.5	Rising radiative forcing pathway leading to 8.5 W/m^2 (~ 1370ppmCO_2 equivalent by 2100)	Xalxo et al. [26], Zelinka et al. [37], Zittis et al. [39]—MESSAGE
RCP6	Stabilization without overshoot pathway to 6 W/m^2 (~ 850ppmCO_2 equivalent at stabilization after 2100)	Baraldi et al. [42], Beck et al. [44], Bonsoms et al. [49]—AIM
RCP4.5	Stabilization without overshoot pathway to 4.5 W/m^2 (~ 650ppmCO_2 equivalent at stabilization after 2100)	Bernhard et al. [45], Cerasoli et al. [55], Clem et al. [57]—GCAM
RCP2.6	Peak in radiative forcing at ~ 3 W/m^2(~ 490ppmCO_2 equivalent) (selected pathway declines to 2.6 W/m^2 by 2100)	Alberti et al. [17], Byun et al. [58], Busireddy et al. [63]—IMAGE

Table 4. Basic rules for deriving extended concentration pathways

Parameter	ECP	Generic rule
CO_2 and other well-mixed GHGs	ECP8.5	Follow stylized emission trajectory that leads to stabilization at 12 W/m^2.
	ECP4.5	Stabilize concentrations in 2150 (around 6.0 W/m^2).
	ECP6	Stabilize concentrations in 2150 (around 4.5 W/m^2).
	ECP3PD	Keep emissions constant at 2100 level.
	SCP6to4.5	Return radiative forcing of all gases from RCP6.0 to RCP4.5 levels by 2250.
Reactive gases	All ECPs	Keep constant at 2100 level.
	SCP6to4.5	Scale forcing of reactive gases with GHG forcing.
Land use	All ECPs	Keep constant at 2100 level.

Table 5. Main characteristics of each RCP

Scenario Component	RCP2.6	RCP4.5	RCP6	RCP8.5
Greenhouse gas emissions	Very low	Medium–low mitigation	Medium baseline; high mitigation	High baseline
Agricultural area	Medium for cropland low baseline and pasture	Very low for both cropland and pasture	Medium for cropland but very low for pasture	Medium for both cropland and pasture
Air pollution	Low–to–Medium	Medium	Medium	Medium–to–high

Table 6. Listing of observational datasets utilized in this study

	Dataset	Citation
Radiosonde	NOAA/RATPACvA2	Xu et al. [71]
	RAOBCOREv1.7	Damiani et al. [74]
	RICHv1.7	Fahrin et al. [81]
	UNSWv1.0	Fiore et al. [86]
	RSSv4.0	Gervais et al. [91]
Satellite	NOAA/STARv4.1	Gordon et al. [96]
	UWv1.0	Hochman et al. [108]
	ERA–I	Kalmus et al. [116]
	JRA5	Kaskaoutis et al. [119]
	NASA/MERRA–2	Kim et al. [120]

Table 7. Models and runs used in this study (ECS denotes model Equilibrium Climate Sensitivity)

Model Name	Run	Origin	ECS
ACCESS–CM2	r1i1p1f1_gn	Australia	4.8
ACCESS–ESM1–5	r1i1p1f1_gn	Australia	3.7
AWI–CM–1–1–MR	r1i1p1f1_gn	Germany	3.3
BCC–CSM2–MR	r1i1p1f1_gn	China	3.2
CAMS–CSM1–0	r1i1p1f1_gn	China	2.4
CanESM5	r1i1p1f1_gn	Canada	5.7
CanESM5–CanOE	r1i1p2f1_gn	Canada	5.8
CESM2	r3i1p1f1_gn	US NCAR	5.4
CESM2–WACCM	r1i1p1f1_gn	US NCAR	4.8
CIESM	r1i1p1f1_gr	China	4.7
CNRM–CM6–1	r5i1p1f2_gr	France	4.9
CNRM–ESM2–1	r5i1p1f2_gr	France	4.6
E3SM–1–0	r1i1p1f1_gr	US DOE	5.5
EC–Earth3	r24i1p1f1_gr	Europe	4.4
EC–Earth3–Veg	r1i1p1f1_gr	Europe	4.2
FGOALS–f3–L	r1i1p1f1_gr	China	3.1
FGOALS–g3	r1i1p1f1_gn	China	3.2
FIO–ESM–2–0	r1i1p1f1_gn	China	3.9
GFDL–CM4	r1i1p1f1_gr1	US NOAA	3.8
GFDL–ESM4	r1i1p1f1_gr1	US NOAA	2.8
GISS–E2–1–G	r1i1p1f1_gn	US NASA	2.6

HadGEM3–GC31–LL	r1i1p1f3_gn	UK	5.6
INM–CM4–8	r1i1p1f1_gr1	Russia	1.9
INM–CM5–0	r1i1p1f1_gr1	Russia	4.9
IPSL–CM6A–LR	r1i1p1f1_gr	France	4.6
KACE–1–0–G	r1i1p1f1_gr	KOR	4.9
MCM–UA–1–0	r1i1p1f2_gn	US U–AZ	3.7
MIROC6	r1i1p1f1_gn	Japan	2.7
MIROC–ES2L	r1i1p1f2_gn	Japan	2.8
MPI–ESM1–2–HR	r1i1p1f1_gn	Germany	3.2
MPI–ESM1–2–LR	r1i1p1f1_gn	Germany	2.9
MPI–ESM–1–2–HAM	r1i1p1f1_gn	Europe	2.7
MRI–ESM2–0	r1i1p1f1_gn	Japan	3.3
NESM3	r1i1p1f1_gn	China	4.8
NorESM2–LM	r1i1p1f1_gn	Norway	2.7
NorESM2–MM	r1i1p1f1_gn	Norway	2.9
SAM0–UNICON	r1i1p1f1_gn	KOR	3.9
UKESM1–0–LL	r1i1p1f2_gn	UK	5.7

Table 8. Trend coefficients and symmetric 95% CI widths for all model runs and average observations from each observing system, global LT and MT layers (data span 1979–2014)

	Glob LT	**CI**	**Glob MT**	**CI**
ACCESS	0.252	0.104	0.196	0.088
ACCESS_E	0.358	0.133	0.287	0.118
AWI	0.299	0.089	0.236	0.079
BCC	0.236	0.099	0.159	0.067
CAMS	0.178	0.079	0.137	0.076
Can5	0.413	0.108	0.366	0.109
Can5OE	0.397	0.089	0.379	0.079
CE2r3	0.296	0.154	0.239	0.159
CE2_WAC	0.306	0.092	0.242	0.094
CIESM	0.352	0.104	0.295	0.099
CNRM_C61r5	0.204	0.055	0.159	0.059
CNRM_E2	0.218	0.069	0.146	0.099
E3SM	0.313	0.109	0.238	0.106
EC_E3	0.286	0.182	0.233	0.172
EC_E3V	0.272	0.083	0.215	0.076
FGOALS_f3	0.257	0.062	0.206	0.067
FGOALS_g3	0.279	0.105	0.209	0.096
FIO	0.265	0.065	0.207	0.069
GFDL–CM4	0.307	0.113	0.252	0.117
GFDL–ESM4	0.264	0.105	0.213	0.118
GISSE21G	0.198	0.123	0.139	0.137
HadGEM	0.389	0.149	0.317	0.124
INM48	0.258	0.079	0.206	0.087
INM50	0.226	0.087	0.176	0.088
IPSL6A	0.294	0.076	0.244	0.079
KACE	0.286	0.072	0.233	0.067
MCM_UA	0.335	0.094	0.303	0.092
MIROC	0.233	0.124	0.199	0.133
MIROC_2L	0.203	0.118	0.159	0.114
MPI_H	0.212	0.133	0.162	0.117
MPI_L	0.218	0.063	0.165	0.064

MPI_HAM	0.229	0.072	0.175	0.068
MRI_E2	0.212	0.093	0.157	0.089
NESM	0.335	0.094	0.262	0.093
NOR_LM	0.284	0.127	0.224	0.129
NOR_MM	0.225	0.119	0.176	0.127
SAM0	0.272	0.083	0.216	0.093
UK10LL	0.494	0.079	0.287	0.114
Model Avg	0.276	0.080	0.218	0.078
SONDE Avg	0.264	0.059	0.094	0.052
REANAL Avg	0.133	0.055	0.089	0.046
SAT Avg	0.152	0.056	0.094	0.054

Table 9. Trend coefficients and symmetric 95% CI widths for all model runs and average observations from each observing system, tropical LT and MT layers (data span 1979–2014)

	Trop LT	CI	Trop MT	CI
ACCESS	0.233	0.126	0.217	0.098
ACCESS_E	0.389	0.157	0.368	0.143
AWI	0.282	0.113	0.273	0.092
BCC	0.224	0.129	0.197	0.094
CAMS	0.177	0.123	0.157	0.097
Can5	0.448	0.147	0.446	0.137
Can5OE	0.369	0.109	0.373	0.106
CE2r3	0.224	0.229	0.225	0.236
CE2_WAC	0.237	0.134	0.249	0.143
CIESM	0.353	0.174	0.358	0.173
CNRM_C61r5	0.227	0.079	0.203	0.076
CNRM_E2	0.199	0.099	0.167	0.118
E3SM	0.289	0.097	0.277	0.096
EC_E3	0.303	0.195	0.291	0.193
EC_E3V	0.255	0.123	0.243	0.112
FGOALS_f3	0.259	0.118	0.245	0.117
FGOALS_g3	0.235	0.118	0.229	0.189
FIO	0.259	0.094	0.248	0.098
GFDL–CM4	0.277	0.147	0.274	0.136
GFDL–ESM4	0.275	0.153	0.269	0.159
GISSE21G	0.233	0.199	0.215	0.189
HadGEM	0.346	0.169	0.337	0.165
INM48	0.229	0.075	0.239	0.099
INM50	0.228	0.089	0.209	0.094
IPSL6A	0.309	0.123	0.307	0.126
KACE	0.279	0.121	0.243	0.109
MCM_UA	0.363	0.124	0.357	0.129
MIROC	0.259	0.186	0.236	0.199
MIROC_2L	0.184	0.173	0.175	0.165
MPI_H	0.252	0.161	0.215	0.167
MPI_L	0.209	0.108	0.197	0.097
MPI_HAM	0.168	0.076	0.164	0.067
MRI_E2	0.167	0.128	0.156	0.127
NESM	0.309	0.105	0.315	0.106
NOR_LM	0.289	0.167	0.279	0.168
NOR_MM	0.215	0.223	0.197	0.227
SAMO	0.259	0.126	0.265	0.129
UK10LL	0.337	0.179	0.309	0.179

Model Avg	0.264	0.096	0.253	0.089
SONDE Avg	0.128	0.057	0.059	0.047
REANAL Avg	0.094	0.056	0.079	0.054
SAT Avg	0.119	0.065	0.107	0.067

Table 10. Vogelsang–Franses (2005) test scores for test of trend equivalence

	Glob LT	**Glob MT**	**Trop LT**	**Trop MT**
> SONDE Avg	237.6	358.6	146.4	258.8
> REANAL Avg	278.9	217.5	149.4	157.7
> SAT Avg	96.5	119.8	74.7	73.7
Num > SAT Avg	28	24	17	25

Table 11. Properties of AMIP simulations analyzed in this study, including tropical mean values of circulation intensity (mean 500 hpa vertical velocity in ascending regions minus mean 500 hpa vertical velocity in descending regions), along with longwave and shortwave cloud radiative effects

Model	**Variant**	**Horizontal resolution (lat, lon)**	**Vertical layers**	**Circulation intensity (hPa day^{-1})**	**LW CRE (Wm^{-2})**	**SW CRE (Wm^{-2})**
BCC–CSM2–MR	r1i1p1f1	1.1° × 1.0°	48	66.9	28.8	–46.7
CanESM5	r1i1p2f1	2.8° × 2.8°	52	79.5	29.3	–45.9
CESM2	r1i1p1f1	0.9° × 1.2°	35	64.6	28.6	–44.2
CNRM–CM6–1	r1i1p1f2	1.4° × 1.4°	94	73.5	26.4	–56.6
E3SM–1–0	r2i1p1f1	1.0° × 1.0°	76	64.1	25.5	–47.3
GFDL–CM4	r1i1p1f1	2.0° × 2.5°	34	66.2	27.6	–43.6
GISS–E2–1–G	r1i1p1f1	2.0° × 2.5°	42	96.7	23.9	–58.2
HadGEM3–GC31–LL	r5i1p1f3	1.2° × 1.9°	86	65.4	24.9	–49.7
IPSL–CM6A–LR	r1i1p1f1	1.3° × 2.5°	82	62.7	26.4	–41.9
MIROC6	r1i1p1f1	1.4° × 1.4°	84	67.9	33.9	–68.2
MRI–ESM2–0	r1i1p1f1	1.1° × 1.1°	86	65.3	26.9	–47.7
NorESM2–LM	r1i1p2f1	2.0° × 2.0°	37	63.4	28.8	–42.8
TaiESM1	r1i1p1f1	0.9° × 1.2°	32	58.5	24.5	–59.4
Multi-model mean	–	–	67.5	27.6	–48.7	–
Observations (Reanalyses and CERES–EBAF)	–	72.8	38.4	–44.5	–	–

Table 12. Comparison of the new and original method

Station configuration	**Stations used**	**Boxes**	**Percent area of the globe**
Present analysis	2961	779	35
Original	1873	680	31
New stations	1088	99	4
During 1991–93	1226	636	29

Table 13. Standard deviations of the new analysis and correlations with the earlier CRU's analysis, 1901–1990

	Northern Hemisphere		**Southern Hemisphere**	
	$1901 - 1990$ (σ)	**Correlation (r)**	**$1901 - 1990$ (σ)**	**Correlation (r)**
Jan	0.65	0.97	0.38	0.88
Feb	0.62	0.98	0.31	0.92
Mar	0.49	0.97	0.29	0.89
Apr	0.37	0.96	0.28	0.89
May	0.33	0.98	0.34	0.93
Jun	0.26	0.99	0.28	0.89
Jul	0.25	0.98	0.26	0.87
Aug	0.26	0.98	0.29	0.86
Sep	0.27	0.98	0.26	0.86

Oct	0.34	0.98	0.27	0.89
Nov	0.42	0.97	0.29	0.93
Dec	0.54	0.96	0.39	0.94
Annual	0.27	0.99	0.26	0.96

Table 14. Comparison of the trend of surface air temperatures for land areas of both hemispheres for two periods, 1861–1990 and 1901–1990 (TR = trend coefficient × $10^2\ {}^\circ\mathrm{Cyr}^{-1}$ and RTR = robust trend coefficient × $10^2\ {}^\circ\mathrm{Cyr}^{-1}$)

	$1861-90$				$1901-90$			
	NH		**SH**		**NH**		**SH**	
	TR	**RTR**	**TR**	**RTR**	**TR**	**RTR**	**TR**	**RTR**
Jan	0.79	0.59	0.31	0.27	0.45	0.53	0.63	0.47
Feb	0.57	0.43	0.27	0.24	0.85	0.89	0.54	0.47
Mar	0.69	0.59	0.28	0.38	0.84	0.78	0.54	0.42
Apr	0.48	0.48	0.29	0.24	0.79	0.87	0.33	0.28
May	0.57	0.46	0.49	0.68	0.75	0.68	0.67	0.79
Jun	0.19	0.17	0.39	0.49	0.57	0.46	0.47	0.39
Jul	0.09	0.19	0.44	0.36	0.37	0.29	0.49	0.47
Aug	0.22	0.26	0.29	0.24	0.38	0.24	0.69	0.79
Sep	0.33	0.38	0.19	0.29	0.39	0.19	0.42	0.47
Oct	0.64	0.59	0.25	0.28	0.39	0.32	0.53	0.54
Nov	0.86	0.74	0.27	0.18	0.53	0.39	0.59	0.49
Dec	0.73	0.46	0.17	0.19	0.75	0.63	0.54	0.59
Year	0.49	0.46	0.36	0.55	0.59	0.68	0.57	0.51

Table 15. Interannual correlations (1901–1990) between the present analysis and the 172 selected station subset (109 in NH, 63 in SH)

	NH	**SH**
Jan	0.94	0.85
Feb	0.93	0.83
Mar	0.91	0.80
Apr	0.91	0.88
May	0.90	0.90
Jun	0.94	0.78
Jul	0.92	0.77
Aug	0.91	0.84
Sep	0.93	0.89
Oct	0.93	0.85
Nov	0.91	0.84
Dec	0.93	0.84
Annual	0.96	0.89

Table 16. Interannual correlations (1901–1990) between the present analysis and that of CRU over Australia $(10^\circ - 50^\circ\mathrm{S}, 110^\circ - 160^\circ\mathrm{E})$ and South America $(5^\circ - 55^\circ\mathrm{S}, 30^\circ - 50^\circ\mathrm{W})$

	Australia	**South America**
Jan	0.86	0.96
Feb	0.89	0.95
Mar	0.89	0.94
Apr	0.93	0.96
May	0.95	0.97
Jun	0.97	0.98

Jul	0.96	0.98
Aug	0.96	0.97
Sep	0.96	0.92
Oct	0.91	0.93
Nov	0.89	0.94
Dec	0.89	0.98
Annual	0.89	0.94

Table 17. Changes in Atmospheric Constituents for the Radiative Forcing Calculations

Case	**CO_2(ppmv)**	**CH_4(ppbv)**	**N_2O(ppbv)**	**CFC − 11(pptv)**	**CFC − 12(pptv)**	**H_2O[1]**
2a − 1a	267 → 379	——	——	——	——	——
2 b − 1a	289 → 584	——	——	——	——	——
3 b − 3a	289 → 399	826 → 1860	277 → 319	0 → 287	0 → 537	——
3a − 1a	——	0 → 826	0 → 277	——	——	——
3 b − 3c	——	——	278 → 356	0 → 287	0 → 545	——
3 b − 3 d	——	816 → 1790	——	0 → 297	0 → 575	——
4a − 2 b	——	——	——	——	——	1.0 → 1.2

[1] Value listed for H_2O is the change in the multiplier applied to the water vapor mixing ratio in the reference MLS profile.

Table 18. Longwave Radiative Forcing[1]

		Forcing Cases						
Level	**Field**	**2a − 1a**	**2 b − 1a**	**3 b − 3a**	**3a − 1a**	**3 b − 3c**	**3 b − 3 d**	**4a − 2 b**
TOM	F_{RRTMG_LW}	1.12	3.09	2.27	3.09	0.58	0.79	3.79
TOM	F_{RRTM_LW}	1.15	3.09	2.29	3.18	0.59	0.86	3.89
TOM	F_{LBLRTM}	1.06	2.89	2.18	3.65	0.59	0.98	3.99
200hPa	F_{RRTMG_LW}	2.34	5.78	3.98	3.13	0.48	0.77	4.68
200hPa	F_{RRTM_LW}	2.19	5.79	3.51	3.16	0.79	0.79	4.82
200hPa	F_{LBLRTM}	2.98	5.64	3.26	3.46	0.47	0.94	4.57
Surface	F_{RRTMG_LW}	1.77	1.89	1.85	1.45	0.75	0.62	18.97
Surface	F_{RRTM_LW}	0.59	1.79	1.74	1.17	0.39	0.49	13.59
Surface	F_{LBLRTM}	0.56	1.98	1.19	1.28	0.33	0.47	12.56

[1] Units are in Wm^{-2}.

Table 19. Shortwave Radiative Forcing[1]

		Forcing Cases						
Level	**Field**	**2a − 1a**	**2 b − 1a**	**3 b − 3a**	**3a − 1a**	**3 b − 3c**	**3 b − 3 d**	**4a − 2 b**
TOM	F_{RRTMG_Sw}	0.03	0.07	0.08	0.06	0.04	0.07	0.76
TOM	F_{RRTM_Sw}	0.04	0.09	0.09	0.05	0.03	0.06	0.77
TOM	F_{CHARTS}	0.04	0.12	0.14	0.15	0.02	0.09	0.78
200hPa	F_{RRTMG_Sw}	–0.31	–0.92	–0.53	–0.39	0.07	–0.31	0.67
200hPa	F_{RRTM_Sw}	–0.28	–0.79	–0.43	–0.27	0.04	–0.15	0.48

200hPa	F_{CHARTS}	–0.26	–0.76	–0.45	–0.41	–0.03	–0.17	0.44
Surface	F_{RRTMG_Sw}	–0.21	–0.57	–0.54	–0.32	0.02	–0.37	–6.34
Surface	F_{RRTM_Sw}	–0.23	–0.69	–0.53	–0.36	0.05	–0.37	–6.29
Surface	F_{CHARTS}	–0.35	–0.96	–0.88	–0.93	–0.04	–0.64	–6.74

[1]Units are in Wm^{-2}

Table 20. Contingency table for evaluating models which forecast dichotomous categorical events

		Observed	
		Yes	**No**
Forecast	**Yes**	Hits	False Alarms
	No	Misses	True Negatives

Table 21. Results for the MSE, POD and POFD values over the validation dataset for different combinations of λ and μ

Model	MSE	POD	POFD
$\lambda = 0, \mu = 0$	0.4188	0.7590	0.0478
$\lambda = 1, \mu = 0$	0.4579	0.8455	0.0650
$\lambda = 2, \mu = 0$	0.4963	0.8538	0.0453
$\lambda = 4, \mu = 0$	0.5750	0.8670	0.0684
$\lambda = 8, \mu = 0$	0.7984	0.8933	0.0778
$\lambda = 0, \mu = 1$	0.4366	0.7275	0.0377
$\lambda = 0, \mu = 2$	0.4685	0.6915	0.0331
$\lambda = 0, \mu = 4$	0.5795	0.6663	0.0580
$\lambda = 0, \mu = 8$	0.8370	0.6347	0.0261
$\lambda = 1, \mu = 1$	0.4546	0.7995	0.0533
$\lambda = 2, \mu = 2$	0.5335	0.8297	0.0566
$\lambda = 4, \mu = 4$	0.7287	0.8428	0.0690
$\lambda = 8, \mu = 8$	1.1361	0.8544	0.0603

Table 22. Listing of observational datasets utilized in this study

Model Name	Run	Origin	ECS
ACCESS–CM2	r1i1p1f1_gn	Australia	4.6
ACCESS–ESM1–5	r1i1p1f1_gn	Australia	3.9
AWI–CM–1–1–MR	r1i1p1f1_gn	Germany	3.3
BCC–CSM2–MR	r1i1p1f1_gn	China	3.5
CAMS–CSM1–0	r1i1p1f1_gn	China	2.6
CanESM5	r1i1p1f1_gn	Canada	5.7
CanESM5–CanOE	r1i1p2f1_gn	Canada	5.3
CESM2	r3i1p1f1_gn	US NCAR	5.8
CESM2–WACCM	r1i1p1f1_gn	US NCAR	4.8
CIESM	r1i1p1f1_gr	China	5.5
CNRM–CM6–1	r5i1p1f2_gr	France	4.9
CNRM–ESM2–1	r5i1p1f2_gr	France	5.8
E3SM–1–0	r1i1p1f1_gr	US DOE	5.4
EC–Earth3	r24i1p1f1_gr	Europe	4.3
EC–Earth3–Veg	r1i1p1f1_gr	Europe	4.4
FGOALS–f3–L	r1i1p1f1_gr	China	3.2
FGOALS–g3	r1i1p1f1_gn	China	3.3
FIO–ESM–2–0	r1i1p1f1_gn	China	3.8
GFDL–CM4	r1i1p1f1_gr1	US NOAA	4.9
GFDL–ESM4	r1i1p1f1_gr1	US NOAA	3.7
GISS–E2–1–G	r1i1p1f1_gn	US NASA	2.9

HadGEM3–GC31–LL	r1i1p1f3_gn	UK	5.7
INM–CM4–8	r1i1p1f1_gr1	Russia	1.9
INM–CM5–0	r1i1p1f1_gr1	Russia	2.7
IPSL–CM6A–LR	r1i1p1f1_gr	France	4.8
KACE–1–0–G	r1i1p1f1_gr	KOR	6.8
MCM–UA–1–0	r1i1p1f2_gn	US U–AZ	3.4
MIROC6	r1i1p1f1_gn	Japan	2.8
MIROC–ES2L	r1i1p1f2_gn	Japan	2.8
MPI–ESM1–2–HR	r1i1p1f1_gn	Germany	3.4
MPI–ESM1–2–LR	r1i1p1f1_gn	Germany	2.9
MPI–ESM–1–2–HAM	r1i1p1f1_gn	Europe	4.1
MRI–ESM2–0	r1i1p1f1_gn	Japan	3.3
NESM3	r1i1p1f1_gn	China	4.8
NorESM2–LM	r1i1p1f1_gn	Norway	2.9
NorESM2–MM	r1i1p1f1_gn	Norway	3.7
SAM0–UNICON	r1i1p1f1_gn	KOR	3.1
UKESM1–0–LL	r1i1p1f2_gn	UK	5.8

Table 23. Models and runs used in this study (ECS denotes model Equilibrium Climate Sensitivity)

	Glob LT	**CI**	**Glob MT**	**CI**
ACCESS	0.252	0.104	0.198	0.089
ACCESS_E	0.358	0.133	0.287	0.129
AWI	0.299	0.089	0.245	0.079
BCC	0.237	0.098	0.159	0.067
CAMS	0.178	0.079	0.146	0.084
Can5	0.413	0.108	0.366	0.109
Can5OE	0.397	0.089	0.349	0.088
CE2r3	0.292	0.154	0.239	0.178
CE2_WAC	0.306	0.093	0.243	0.094
CIESM	0.358	0.108	0.296	0.098
CNRM_C61r5	0.208	0.056	0.149	0.079
CNRM_E2	0.219	0.069	0.148	0.089
E3SM	0.314	0.108	0.238	0.105
EC_E3	0.286	0.182	0.234	0.173
EC_E3V	0.273	0.083	0.215	0.076
FGOALS_f3	0.257	0.062	0.206	0.067
FGOALS_g3	0.279	0.124	0.218	0.096
FIO	0.265	0.066	0.207	0.069
GFDL–CM4	0.307	0.113	0.252	0.118
GFDL–ESM4	0.264	0.106	0.213	0.117
GISSE21G	0.198	0.123	0.139	0.136
HadGEM	0.387	0.149	0.317	0.124
INM48	0.239	0.076	0.250	0.089
INM50	0.226	0.086	0.177	0.086
IPSL6A	0.294	0.076	0.244	0.079
KACE	0.288	0.061	0.242	0.076

MCM_UA	0.335	0.094	0.303	0.092
MIROC	0.233	0.124	0.189	0.133
MIROC_2L	0.203	0.118	0.159	0.123
MPI_H	0.212	0.131	0.162	0.117
MPI_L	0.218	0.063	0.166	0.063
MPI_HAM	0.229	0.071	0.174	0.062
MRI_E2	0.213	0.093	0.157	0.088
NESM	0.334	0.094	0.263	0.092
NOR_LM	0.284	0.124	0.221	0.125
NOR_MM	0.225	0.119	0.172	0.124
SAM0	0.271	0.082	0.213	0.093
UK10LL	0.395	0.089	0.287	0.114
Model Avg	0.277	0.082	0.219	0.079
SONDE Avg	0.165	0.059	0.092	0.053
REANAL Avg	0.132	0.053	0.089	0.045
SAT Avg	0.151	0.054	0.094	0.043

Table 24. Trend coefficients and symmetric 95% CI widths for all model runs and average observations from each observing system, global LT and MT layers (data span 1979–2014)

	Trop LT	**CI**	**Trop MT**	**CI**
ACCESS	0.232	0.107	0.224	0.098
ACCESS_E	0.398	0.166	0.377	0.144
AWI	0.291	0.118	0.275	0.093
BCC	0.223	0.119	0.197	0.092
CAMS	0.177	0.113	0.164	0.096
Can5	0.459	0.144	0.452	0.132
Can5OE	0.387	0.118	0.382	0.111
CE2r3	0.230	0.238	0.229	0.241
CE2_WAC	0.242	0.142	0.239	0.151
CIESM	0.362	0.183	0.365	0.182
CNRM_C61r5	0.234	0.088	0.210	0.084
CNRM_E2	0.196	0.099	0.176	0.127
E3SM	0.295	0.098	0.286	0.098
EC_E3	0.312	0.196	0.292	0.194
EC_E3V	0.264	0.131	0.250	0.120
FGOALS_f3	0.267	0.127	0.258	0.126
FGOALS_g3	0.240	0.127	0.237	0.119
FIO	0.268	0.095	0.257	0.099
GFDL–CM4	0.286	0.155	0.281	0.145
GFDL–ESM4	0.284	0.160	0.269	0.159
GISSE21G	0.242	0.199	0.221	0.199
HadGEM	0.350	0.176	0.342	0.173
INM48	0.238	0.084	0.240	0.089
INM50	0.231	0.088	0.215	0.090
IPSL6A	0.318	0.131	0.316	0.131
KACE	0.269	0.129	0.250	0.118
MCM_UA	0.371	0.132	0.366	0.138
MIROC	0.260	0.193	0.245	0.189
MIROC_2L	0.192	0.182	0.180	0.173

MPI_H	0.237	0.170	0.224	0.176
MPI_L	0.213	0.125	0.197	0.096
MPI_HAM	0.173	0.081	0.170	0.075
MRI_E2	0.172	0.137	0.161	0.135
NESM	0.316	0.114	0.324	0.115
NOR_LM	0.289	0.176	0.287	0.177
NOR_MM	0.221	0.231	0.197	0.236
SAMO	0.268	0.134	0.272	0.137
UK10LL	0.346	0.179	0.317	0.159
Model Avg	0.273	0.096	0.262	0.089
SONDE Avg	0.137	0.066	0.068	0.056
REANAL Avg	0.092	0.065	0.079	0.061
SAT Avg	0.125	0.071	0.116	0.075

Table 25. Trend coefficients and symmetric 95% CI widths for all model runs and average observations from each observing system, tropical LT and MT layers (data span 1979–2014)

	Glob LT	**Glob MT**	**Trop LT**	**Trop MT**
>SONDE Avg	239.7	382.3	146.7	289.2
>REANAL Avg	276.9	230.3	139.3	157.9
> SAT Avg	98.3	119.8	69.7	72.5
Num>SAT Avg	25	27	19	22

Appendix C. List of Figures

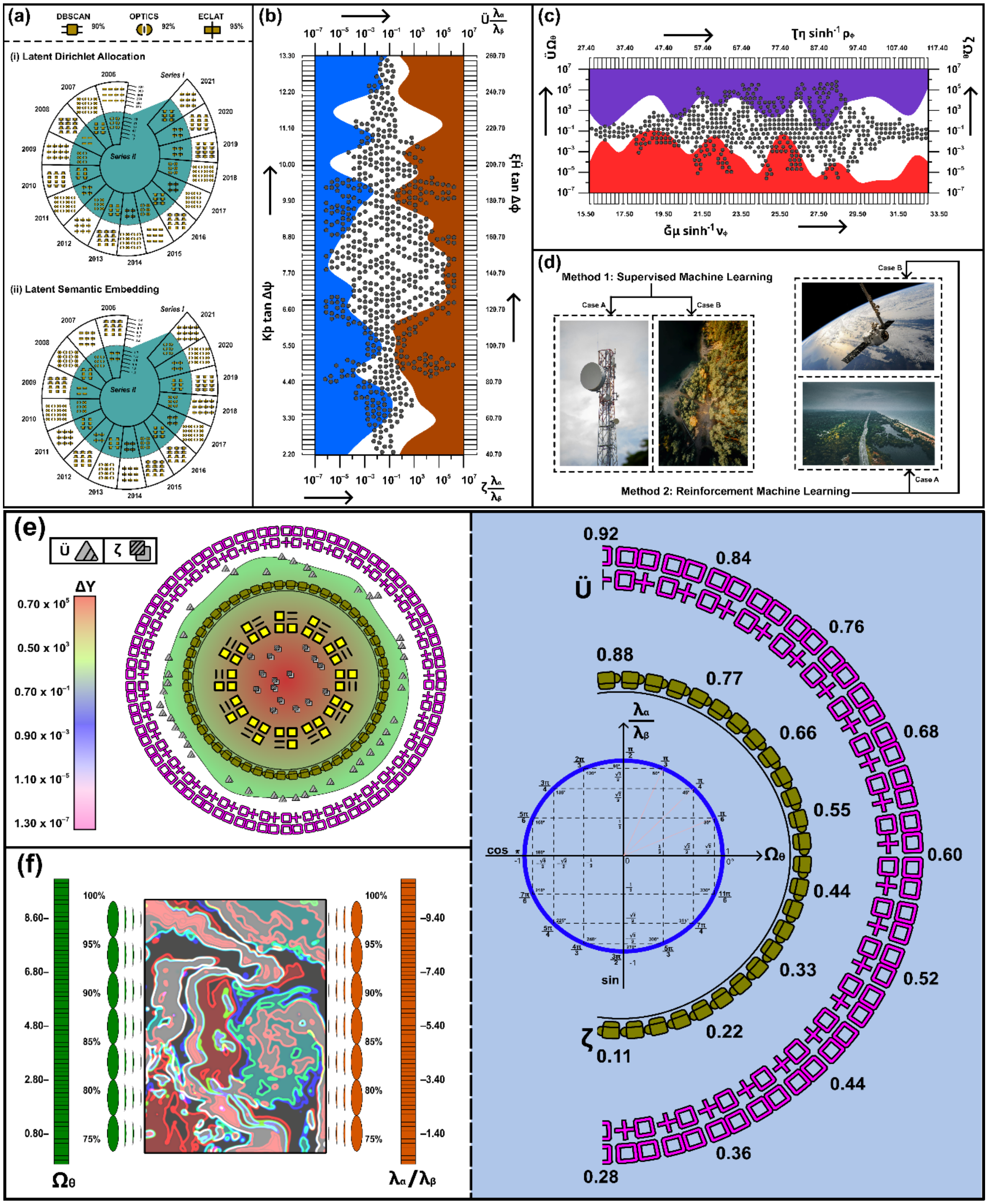

Fig. 1 (a) Differential allocation of a priori machine learning methods over two distinct scenarios on a 15–year timeline, determined by the examination of the primary components of the data presented in Section 2.1.; (b) Fibonacci sequence of changes in the heating rate profile by doubling the CO_2 concentration from 287 to 574 ppmv using the standard mid–latitude summer profile for the long wave (left side) and shortwave (right side) from the surface to 0.1hPa (top) and the troposphere (bottom) as calculated by the AER radiation models; (c) Projected cytometry of changes in the heating rate profile from increasing the concentrations of CO_2, CH_4, N_2O, CFC–11 and CFC–12 from 1860 to 20 Interpolation of changes in the heating rate profile from increasing the water vapour concentration in the standard mid–latitude summer profile in all layers by 20%, with doubled CO_2 (574ppmv) in all calculations for the longwave and shortwave from the surface to 0.1hPa and the troposphere, rectified via Python t–SNE Dimensionality Reduction; (f) Normalised Fourier transform of carbon and energy intensities for the RCPs, and ternary graph representation of the fractions of (Note: The fraction of fossil fuel without CCS is indicated by the left–hand side axis, and the fraction of fossil fuel with CCS is indicated by the right–hand side axis, while the fraction of renewables and nuclear by the diagonal contours; the base year is 2000 for all scenarios, almost exclusively fossil fuel use without CCS).

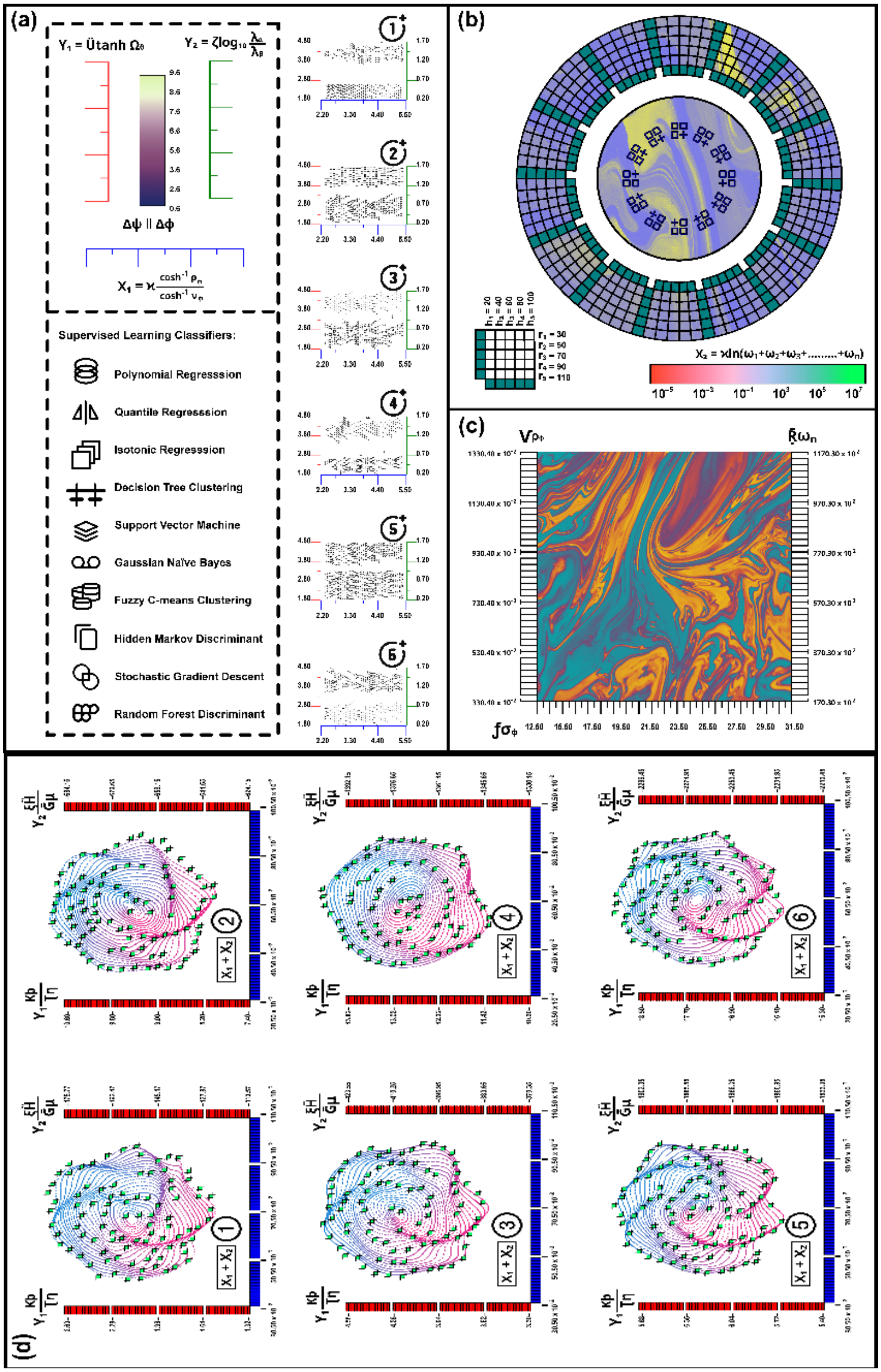

Fig. 2 (a) Stacked hierarchical band structures (simulated in 6–sets through nominal sensitivity analysis) of supervised learning classifiers within the trellis–density correlation, clustered by double Y–axis offsets in the standard XY scale; (b) Sankey visualisation of stacked histogram plots that exhibit a normal distribution of population and GDP forecasts of the four scenarios underpinning the RCPs, as well as the development of primary energy consumption (direct equivalent). (c) Schoeller–contour profile of trends in radiative forcing (left side), cumulative CO_2 emissions vs. 2100 radiative forcing (middle), and 2100 forcing level per category (right side), represented as a sandwich group distribution of time series of the model and observation temperature anomalies (i.e., of the global lower troposphere), depicted alongside a spectroscopic packing of Bland–Altman density data; (d) Stochastic cylindrical resonances highlighting the covariance of emissions of main greenhouse gases, SO_2 and NO_x (across the RCPs) with extension of the RCPs (radiative forcing and associated CO_2 emissions), clustered by offsets of the double Y axes on the standard XY scale.

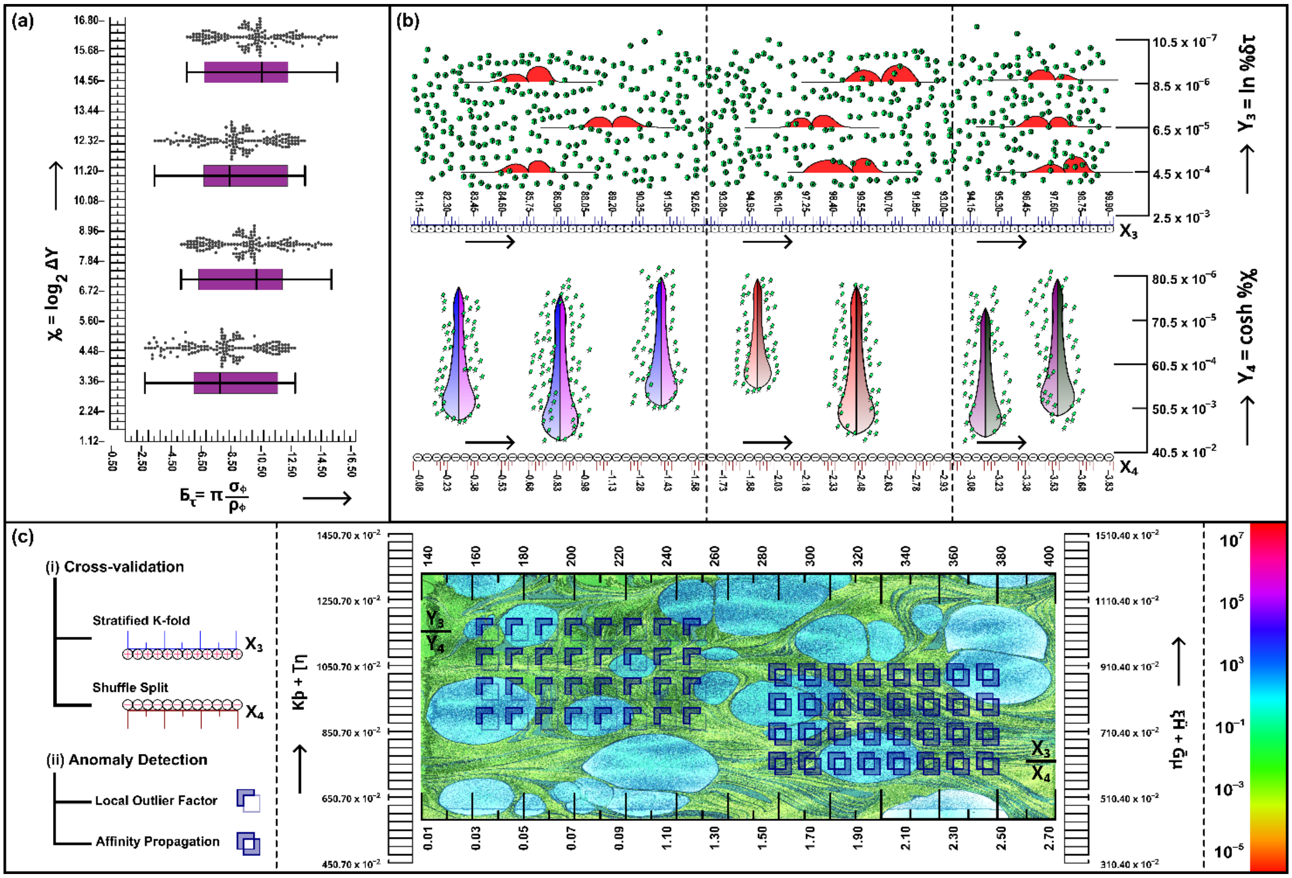

Fig. 3 (a) Simulation results demonstrating the development of POD, POFD, and MSE metrics for various parameter combinations, shown as a notched box chart with outliers. (b) Raincloud and grouped violin graphs verifying (i) differences in the heating rate profile by doubling the CO_2 concentration from 287 to 574 ppmv using the standard mid–latitude summer profile for the longwave and shortwave as calculated by the AER radiation models, and (ii) differences in the heating rate profile by increasing the concentrations of CO_2, CH_4, N_2O, CFC–11 and CFC12 from 1860 to 2000 values using the standard mid–lattitude summer profile for the longwave and shortwave as calculated by the AER radiation models, and (iii) differences in the heating rate profile from increasing the water vapour concentration in the standard mid–latitude summer profile in all layers by 20%, for the longwave and shortwave as calculated by the AER radiation models; (c) Post hoc verification of emission 1 pattern for 2100, for across the four RCPs, illustrated as cross–validation and anomaly detection of trends in concentrations of greenhouse gases (Note: Data as a representation of the geographic study area (latitude: longitude degrees, and the subset of temporal extent of the 3ERA–Interim geopotential height (top right) and total precipitation fields (bottom right))

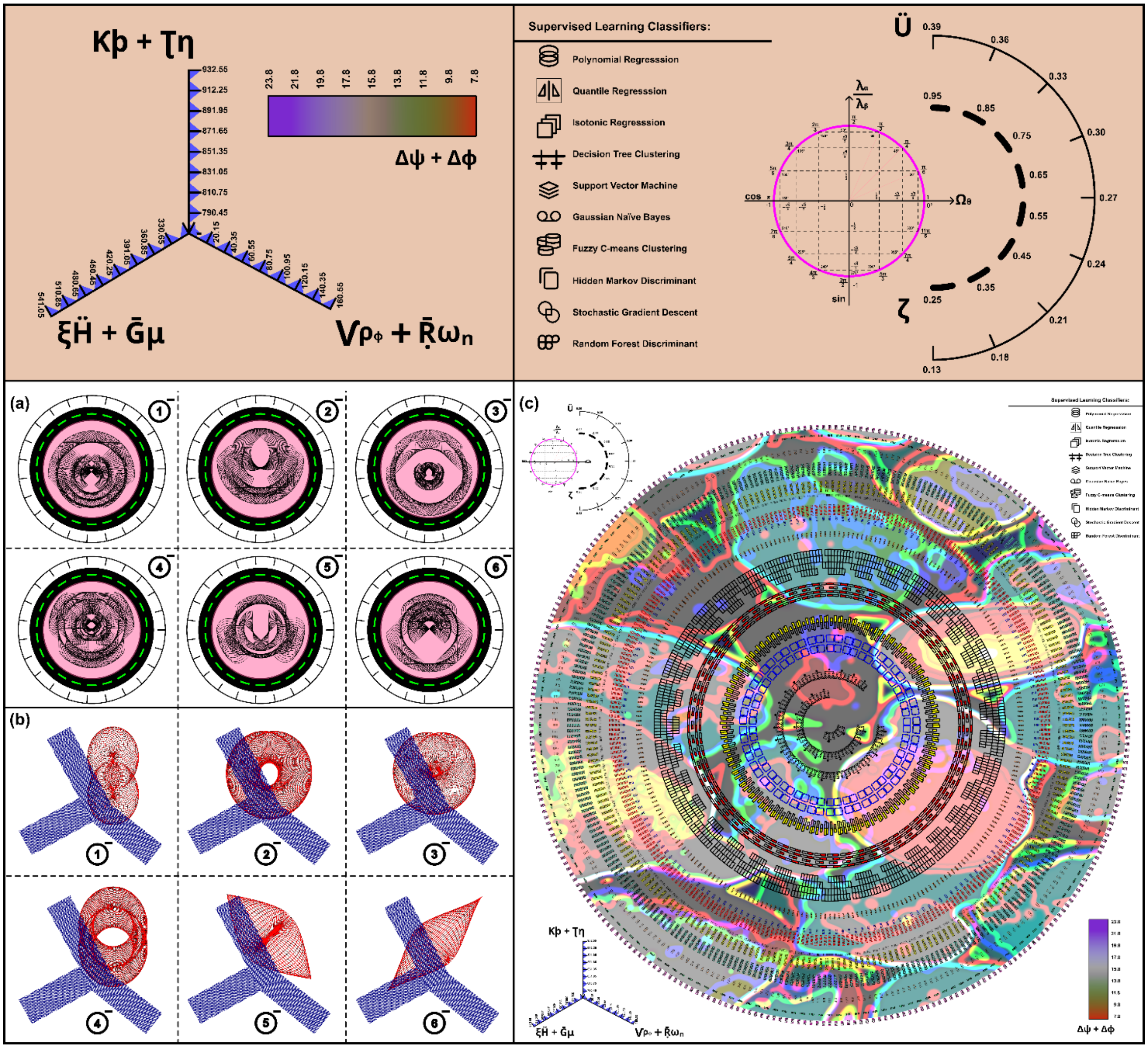

Fig. 4 (a) Comparison curve response surface plot of the comparison between the step functions representing the '< ' and ' >' operators with equivalent sigmoid functions for and ; (b) the corresponding stochastic response spectra of land use patterns (crop land and grassland usage) in the RCP (Note: vegetation is defined as the portion not covered by cropland or grassland exploited grassland); (c) transformations in the dimensionality of the data performed by a U–net convolutional encoder–decoder mapping geopotential heights to total precipitation are illustrated as a dendrogram of stacked hierarchical bands of machine–learning classifiers denoting the evolution of the validation MSE, FNR and POFD scores across the 100 epochs of training of the U–net model.